ANAEROBIC PITTING CORROSION OF CARBON STEEL IN MARINE SULFIDOGENIC ENVIRONMENTS

by

Bret Harrison Davis

A thesis submitted in partial fulfillment
of the requirements for the degree

of

Master of Science

in

Physics

MONTANA STATE UNIVERSITY
Bozeman, Montana

April, 2013

APPROVAL

of a thesis submitted by

Bret Harrison Davis

This thesis has been read by each member of the thesis committee and has been found to be satisfactory regarding content, English usage, format, citation, bibliographic style, and consistency and is ready for submission to The Graduate School.

Richard Smith

Approved for the Department of Physics

Richard Smith

Approved for The Graduate School

Dr. Ronald W. Larsen

STATEMENT OF PERMISSION TO USE

In presenting this thesis in partial fulfillment of the requirements for a master's degree at Montana State University, I agree that the Library shall make it available to borrowers under rules of the Library.

If I have indicated my intention to copyright this thesis by including a copyright notice page, copying is allowable only for scholarly purposes, consistent with "fair use" as prescribed in the U.S. Copyright Law. Requests for permission for extended quotation from or reproduction of this thesis in whole or in parts may be granted only by the copyright holder.

Bret Harrison Davis

April 2013

ACKNOWLEDGEMENTS

This work is supported by Office of Naval Research (ONR) Multidisciplinary University Research Initiative (MURI) grant N00014-10-1-0946.

I want to thank all past and present members of the Imaging and Chemical Analysis Laboratory (ICAL) for their help and instruction in the many analytical instruments in ICAL: Dr. Muhammedin Deliorman, Dr. Zhiyong "Jahson" Suo, Kilean Lucas, Dr. Mark Wolfenden, Linda Loetterle, Laura Kellerman, Nancy Equall and Josh Martin. Many thanks go to my advisor and the leader of ICAL, Dr. Recep Avci, for taking me into his lab and leading me down a path of critical thinking.

This work would not have been possible without the wide range of collaborators who comprised the MURI team, most notably of the Microbiology Department at the University of Oklahoma in Norman, OK. These include Dr. Iwona Beech, with whom we had fruitful discussions, and Dr. J. Suflita and his research group (particularly I. A. Davidova and Tiffany Lenhart), who provided and advised us on the growth of SRB cultures. Also, Dr. J. Hammond and D. Paul of Physical Electronics deserve thanks for their contributions of Auger nanoprobe data. Scott Sitzman of Oxford Instruments NanoAnalysis generously provided EBSD data and so deserves thanks. The Center for Biofilm Engineering at MSU was instrumental in providing equipment, as well as being a nearby focus for academic collaboration.

TABLE OF CONTENTS

TABLE OF CONTENTS – CONTINUED

TABLE OF CONTENTS – CONTINUED

LIST OF TABLES

Table Page

LIST OF TABLES – CONTINUED

Table Page

LIST OF FIGURES

Figure Page

LIST OF FIGURES – CONTINUED

Figure Page

LIST OF FIGURES – CONTINUED

Figure Page

LIST OF FIGURES – CONTINUED

Figure Page

LIST OF FIGURES – CONTINUED

Figure Page

LIST OF FIGURES – CONTINUED

Figure Page

LIST OF FIGURES – CONTINUED

Figure Page

LIST OF FIGURES – CONTINUED

Figure Page

ABSTRACT

Microorganisms find their way into fuel tanks by multiple means. For example, some fuel tanks in U.S. Navy vessels utilize seawater to replace ballast lost to burned fuel. This introduces a consortium of aerobic and anaerobic fuel-degrading organisms that form biofilms on the tank's inner walls. These biofilms create oxic gradients; allowing aerobic and anaerobic organisms to live in synergistic alliance. The presence and activity of these organisms influence degradation of fuels and corrosion of tank materials. This thesis focuses on corrosion of iron under strict anaerobic (anoxic) sulfidogenic marine environments.

Manganese sulfide (MnS) inclusions are known sites of pitting corrosion in carbon steel in aqueous environments. This work investigates pitting corrosion of carbon steel under exposure to sulfate-reducing organisms in anaerobic marine environments. It was found that pitting was initiated in the boundary regions of MnS inclusions at normal pH. Corrosion in general was more pronounced in the presence of a biofilm of sulfate-reducing bacteria than in abiotic sulfide medium. It is proposed that the initiation of an anodic reaction leading to the dissolution of the Fe matrix and subsequent pitting of steel in the boundary regions of MnS inclusions is due to strain exerted on the Fe matrix by MnS minerals mixed within the Fe matrix at the interface due to metallurgical processes. We discovered that on the average only 1 out of ~2200 inclusions (or ~2 pits per mm^2 area) are activated to initiate pitting corrosion at normal pH. This increases very rapidly and reaches to pitting densities of ~4200 pits/mm^2 at acidic conditions (pH <4). The main reason for this is because MnS inclusions start dissolving at low pH conditions via $MnS + 2H^+ \rightarrow H_2S + Mn^{2+}$. This mechanism produces H_2S abiotically, which auto catalyzes the pits to grow along the long (hundreds of microns) micro-wires of MnS inclusions. At certain locations these micro-pits join together to give rise to macroscopic pitting in metals.

INTRODUCTION

Motivation

In metal systems undergoing corrosion, mechanical failure typically results from a crack or pit that formed as a result of accelerated localized corrosion. The source of localized attack is impurities in the metal which change the electrochemical environment and create unique stresses and strains. Furthermore, where these systems are in contact with microbial life, biofilms that form on the metal surface and cellular metabolism create complex electrochemical environments which may serve to accelerate or inhibit corrosion. It has been shown that manganese sulfide (MnS) inclusions act as pitting sites in carbon steel, but the details of how pits initiate and why some inclusions are more active while others are not have not been determined. The roles microorganisms play in corrosion have yet to be shown as well. This work is part of the Multi-University Research Initiative (MURI) project, funded by the Office of Naval Research, on the bio-corrosion of carbon steel and fuel degradation in seawater-compensated fuel ballast tanks (SWCFBT) in Navy vessels. SWCFBT solve the problem of the ship maintaining balance via replacing the mass loss to the spent fuel by bilging filtered seawater into the tank. This creates a stratified environment where a separate fuel layer sits atop the seawater. Seawater is rich in microbial life, and this system introduces a wide consortium despite filtration, including known fuel-degrading sulfate-reducing bacteria (SRB). These microbes generate hydrogen sulfide (H_2S), a known aggressive corroder of steel, close to the steel tank walls by the reduction of sulfate (SO_4^{2-}).

Working Hypothesis

This thesis investigates the initiation of pitting in 1018 carbon steel (the primary SWCFBT material) at sites of MnS inclusions under exposure to sulfidogenic, anaerobic marine environments with and without SRB. The extent of pitting corrosion due to H_2S and the SRB's metabolism is elucidated, as well as aspects of general corrosion. We find evidence that supports the hypothesis that residual stain in the metal is what drives the localized corrosion, and so the results of this study can be extended to other metal-corrosion systems.

Corrosion Principles

Corrosion in metals is an electron transfer process in which electrons are lost from the metal surface (anode, reductant, or electron donor), subsequently freeing metal cations and generating dissolution of the solid metal. For the electrochemical reaction to complete there must be an electron acceptor (cathode or oxidant) present.

Redox Reactions

The net reaction is a redox reaction, consisting of two half reactions that represent the anodic reaction (oxidation) and the cathodic reaction (reduction), as illustrated in equations 1–3.

(1) Oxidation: anode → oxidized form + electrons

(2) Reduction: cathode + electrons → reduced form

(3) REDOX: anode + cathode → oxidized form + reduced form

Two requirements are imposed on the electrons for corrosion to proceed: (1) the change must be thermodynamically favorable and (2) there must be an availability of kinetic pathways, which act as the wires in the corrosion cell circuit. The first requires that the electron lower its free energy upon transfer from anode to cathode. The change in an electron's free energy (ΔG^o) at standard conditions and neutral pH is given by its change in reduction potential (ΔE_0) under the same standard conditions. E_0 is an empirical value directly proportional to a compound's affinity for accepting electrons in units of voltage measured against some reference electrode (typically based on hydrogen reduction, called the standard hydrogen electrode, or SHE). The relationship is given in equation 4.

(4) $\Delta G^o = -n\ F\ \Delta E_0$

where n is the number of electrons and F is the Faraday constant (F = 23 kcal/mole) (**Willey**).

Therefore, electron flow is from a lower to a higher reduction potential. Standard reduction potentials are well tabulated.

Corrosion Products

Corrosion products may take the form of precipitates that are deposited on the metal surface. These provide new kinetic pathways that accelerate corrosion (**Lewandowski**) or passivate a metal surface to inhibit it (**Videla**). In addition, changes in surface morphology create pocket "microenvironments" of different pH, salinity, etc. (**Wranglen**). This creates a dynamic chemistry in which the corrosion process can be either perpetuated or halted.

Microbially Influenced Corrosion

Microbiology Review

Unlike a corroding metal, which can only lose energy to its surroundings and never gain any, microbial cells are in a constant state of flux. They possess a system that can store and reuse energy as needed, allowing them to transport molecules across their plasma membranes with or against concentration or electrochemical gradients. This provides great power to influence their surroundings in a nonspontaneous way.

Bacteria may be categorized by their method of taking up energy, electrons, and carbon and their terminal electron acceptor in respiration. These fuel the reactions of life. Microbes require electrons to reduce power in their electron transport chain, and to keep the current of electrons moving, an externally abundant and highly electronegative compound (such as S^{6+} in SO_4^{2-}) is required to accept the electron at the end of the chain. In nature, the ultimate electron acceptor is oxygen. Therefore, microbes fall into two classes, those that utilize oxygen as a terminal electron acceptor (aerobes) and those that utilize another compound, such as SO_4^{2-} (anaerobes).

Biofilm

After bacteria first colonize a metal surface, they begin excreting extracellular polymeric substances (EPS) and utilizing quorum sensing (cell communication) to build up a biofilm (**Willey**), in which they thrive. The EPS is a complex consortium of polysaccharides, proteins, lipids, DNA, and other bio-molecules that make up the biofilm matrix. Eventually, a stratified system exists starting at the metal surface and ending at

the outside surface of the biofilm where it meets the bulk solution. Different microbes with different metabolisms inhabit the separate layers, creating unique electrochemical environments in each. It is important to note that although these layers are distinguishable, the biofilm as a whole is a synergistic system, with all the elements contributing to each other. A mass of biofilm may serve to isolate particular regions of the surface from the bulk solution. Cellular metabolism and surface chemistry can either exacerbate corrosion or mollify it in these separated zones.

In a biofilm environment, perhaps the most influential factor in corrosion is the oxic/anoxic gradient. When the bulk solution is oxic but the surface of the metal is anoxic, with some gradient between, anaerobes live close to the metal surface and aerobes close to the surface. Ultimately, most of the electrons oxidized from the metal surface reduce oxygen, and it is the pathway taken by these electrons through the biofilm that determines the electrochemistry of the system. To clarify the anaerobic processes, this thesis focuses on strict anoxic systems.

Other Microbially Influenced Corrosion

Microbes may also influence corrosion via the direct uptake of electrons (oxidizing power) from metals and other compounds (**Venzlaff**) or the opening of new kinetic pathways via their EPS **(Beech**). Hydrogen evolution is a key step in anaerobic corrosion when protons act as the cathode. All microbes take up hydrogen and reduce it. The microbial cell may produce products that serve as alternative oxidants or reductants or catalyze the already present redox reactions.

Sulfate-Reducing Bacteria Investigated

The microbes investigated in this study are the anaerobic SRB *Desulfoglaeba alkanexedens* (strain ALDC) (**Davidova**) and *Desulfovibrio indonensis* (**Feio**), which utilize sulfate as a terminal electron acceptor, thereby reducing it to hydrogen sulfide, a known accelerator of steel corrosion. As a carbon and electron source, ALDC degrades n-alkanes. *D. indonensis*, on the other hand, degrades lactate ($CH_3CH(OH)COO^-$) as a carbon and electron source but cannot utilize n-alkanes. Fossil fuels are hydrocarbon-rich, making these microbes of particular interest in studies on fuel degradation. From a practical standpoint, *D. indonensis* was used in corrosion experiments because of its short doubling time compared to ALDC. Cultures of *D. indonensis* were ready for corrosion experiments only a few days after inoculation, compared to a few months for ALDC. As a model, decane ($C_{10}H_{22}$) is provided to ALDC cultures. The net metabolic reaction is given in equation 5.

(5) $C_{10}H_{22} + 7.75\ SO_4^{2-} + 5.5\ H^+ \leftrightarrow 10\ HCO_3^- + 7.75\ H_2S + H_2O$

Sulfide Chemistry

H_2S is a gas that, when dissolved in aqueous solution, acts as a weakly diprotic acid, meaning it can lose one or both of its hydrogen atoms. The equilibrium of sulfide species as a function of pH (negative log of proton (H^+) concentration) is given by the acid dissociation constant (k) in equations 6 – 8.

(6) $H_2S \rightarrow H^+ + HS^-$ $\qquad k_1 = 10^{-7} = [H^+][HS^-]/[H_2S]$

(7) $HS^- \rightarrow H^+ + S^{2-}$ $\qquad k_2 = 10^{-15} = [H^+][S^{2-}]/[HS^-]$

(8) $H_2O \rightarrow H^+ + OH^-$ $\quad\quad k_3 = 10^{-14} = [OH^-][H^+]$

Square brackets indicate concentration. These "mass action" relations give a system of equations that are solved for the equilibrium concentrations as a function of pH. These are plotted in Fig. 1. The total concentration of sulfide species is expressed as $[S] = [H_2S] + [HS^-] + [S^{2-}]$. Note that [S] does NOT mean the total concentration of S, but rather the total concentrations of sulfide species, not elemental sulfur species.

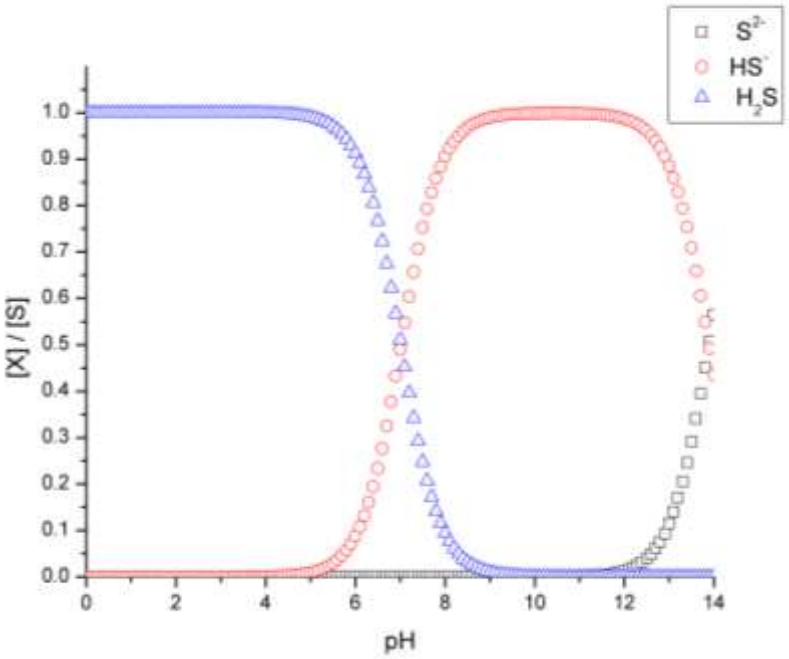

Figure 1: Equilibrium concentrations of sulfide species in aqueous solution as a function of pH. [X] is the concentration of H_2S, HS^-, or S^{2-}.

At physiological pH (~7) H_2S and HS^- are equally dominant. S^{2-} makes up only a small fraction of the total concentration at pH < ~12, so the natural log of the fraction of S^{2-} is plotted in Fig. 2. At pH 7, S^{2-} only makes up 4.5×10^{-6} % of the total sulfide concentration.

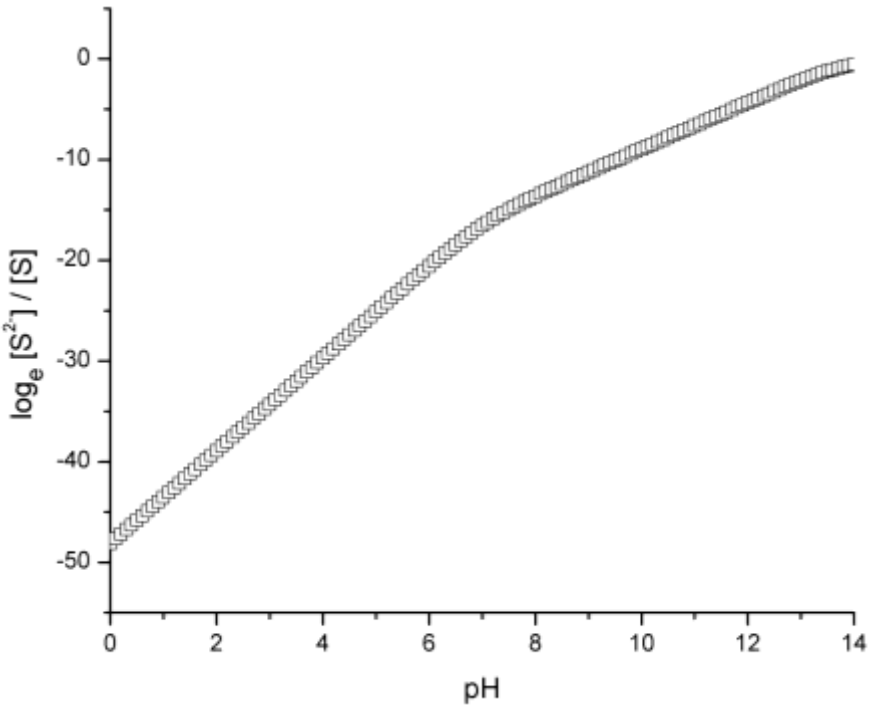

Figure 2: Natural log of fraction of S^{2-} as a function of pH.

Already, it is evident that pH plays a vital role. Physiological pH is around 7, but in a pit microenvironment, pH has been measured as low as 3.5 (**Brown**). Different relative concentrations of sulfide species will inevitably lead to different corrosion products, catalytic efficiency, etc. which will alter the corrosion process.

Sulfur possesses a wide range of oxidation states (−2 to +6), allowing it to influence corrosion and biological systems dynamically. Hydrogen sulfides (H_2S, HS^-, and S^{2-}) are totally reduced sulfur compounds with sulfur in the −2 oxidation state. Sulfides are well-known corrosive agents because they will readily accept electrons.

Iron Sulfide

Sulfide ions and freed iron cations will readily form iron sulfide by the mechanism given in equation 9.

(9) $Fe^{2+} + S^{2-} \rightarrow FeS$

Iron sulfide acts as a conductor in an anaerobic environment and forms a corrosion deposit on a metal surface. This is without the consequence of passivation; rather, there is electron transport between the metal anode and external cathodes.

MATERIALS AND METHODS

Methods of Analysis

Introduction

Surface-sensitive spectroscopic techniques were utilized that could reveal morphological features as well as the elemental composition of the surface with the necessary resolution to analyze nano-sized inclusions and pits. When doing analysis on nano and microscales, it is important to be aware of the excitation volume of the sample, and the volume from which information leaves and arrives at the detector (information volume) depends on the analytical techniques used. For a given excitation volume smaller information volumes yield more spatially resolved information. As a high-energy electron beam (primary electron beam) makes contact with a sample, the primary electrons scatter off the sample atoms as a cascade of elastic and inelastic collisions, generating an excitation volume in the shape of a teardrop. Some inelastic collisions transfer energy from the primary electrons to the specimen atoms, which generate secondary radiation in the form of characteristic Auger electrons and characteristic X–rays (**Goldstein**).

Auger Process and Characteristic X-rays

Excitation of an atom ejects a core electron, which leaves a vacancy that is filled by a higher-energy electron from a higher orbital. The energy released by this process can be manifested as an emission of either a characteristic X–ray or a characteristic Auger electron. If it is an Auger electron, the atom that released it now has a double vacancy in

its core levels: one vacancy is due to filling a core hole and the other is due to the ejection of the Auger electron (**Goldstein**). An atom undergoes a range of transitions for a given primary beam energy, and each of these generates its own characteristic Auger electron or characteristic X–ray. A given primary beam with electron energy (i.e. ~ 20 keV) generates a given excitation volume. However, the volumes of different "flavors" of information, as shown in Fig. 3, are quite different. Auger electrons carry information from a much smaller volume (a few nm^3), dependent on the kinetic energy of the Auger electrons, than characteristic X–rays (a volume of a few μm^3).

The normalized count of Auger electrons and/or characteristic X–rays as a function of electron kinetic energy or X–ray energy is characteristic of the parent atom's atomic core level structure, providing elemental identification. These are Auger electron spectroscopy (AES) and energy-dispersive X–ray spectroscopy (EDX), respectively. EDX provides quantitative analysis accurate to ~1 atomic % for heavy elements, but can only report qualitative analysis for the lighter, biological elements (i.e. O, N, C, P) (**Goldstein**). This makes quantitative analysis of biologically corroded samples challenging.

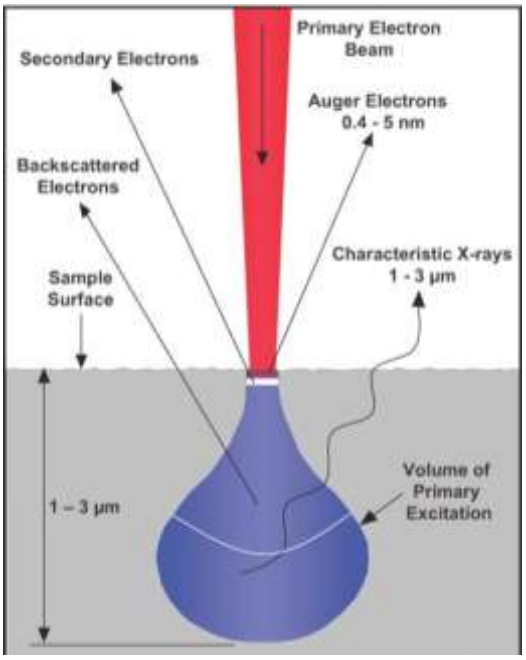

Figure 3: Diagram illustrating excitation volume and information volumes of Auger, EDX, and SEM after irradiation with a primary electron beam (phi.com).

Sputter Etching

Auger probes are equipped with focused Ar^+ ion beam guns for sputter etching of a surface. Sputtering is a technique in which atomic layers are removed layer by layer by focused Ar^+ ions. An elemental analysis is made of each layer, building a stratigraphic picture of the material, called a depth profile. This is only possible because of the shallow information depth from which Auger electrons escape.

Electron Backscatter Diffraction

The primary electrons may go through just elastic scattering that changes their trajectory but does not change their energy. If a primary electron backscatters and escapes the sample, then that measured electron is a backscattered electron. The diffraction pattern (Kikuchi pattern) of backscattered electrons reveals information about

the orientation of crystalline domains (**Goldstein**). The derivative of the orientation map translates into residual strain in the crystal lattice. This phenomenon is referred to as electron backscatter diffraction (EBSD). Many field emission scanning electron microscopes (FEMs) are equipped with systems to measure the EBSD generated from the primary electron beam.

Instrumentation

AES was conducted using an in-house PHI 660 Auger Microprobe and a PHI 700Xi Auger Nanoprobe at Physical Electronics (PHI), Chanhassen, MN. Our Auger microprobe is equipped with a lanthanum hexaboride (LaB_6) electron source operating typically at 10-keV primary energy that generates a spot size of ~0.3 to 3 μm and an Auger nanoprobe with a 25-kV Schottky thermal field emission source that generates a spot size of ~5 nm. These were equipped with a focused Ar^+ ion beam for depth profiling and secondary electron microscopy (SEM). Auger microprobe data were analyzed using the AugerScan version 3.22 software provided by RBD Enterprises, Inc. (Bend, OR). AES nanoprobe and microprobe measurements were conducted with probe currents of ~1 nA and 100 nA and accelerating voltages of 20 kV and 10 kV, respectively.

Imaging was done in a FEM from ZEISS (SUPRA 55VP, Carl Zeiss MicroImaging, GmbH, Gottingen) in parallel with EDX. The FEM is equipped with a thermal field emission electron source and possesses ultrahigh resolution at low kV (1.7 nm at a 1.0-keV primary beam). High-resolution imaging was done without any conductive coating at an accelerating voltage of 1 kV and a working distance of 3 mm. EDX spectra were collected for ~45 seconds at X-ray energies between 0 and 10 keV

using a 20-keV primary beam energy and a working distance of 15 mm. EDX spectra were analyzed using the Spirit, version 1.07.05 software provided by Princeton Gamma-Tech, Inc. (Rocky Hill, NJ).

Atomic force microscopy (AFM) was conducted with a Veeco Multimode V (Veeco, Santa Barbara, CA) operated in tapping mode.

Anaerobic Chamber

To create an oxygen-free environment, experiments were performed in an anaerobic glovebox manufactured by Forma Scientific (Marietta, OH). The chamber atmosphere was a mixture of nitrogen and hydrogen with hydrogen regulated to a range of 1–7% (by volume). Proper pressure in the chamber was maintained via a release valve through mineral oil to prevent any backflow of air.

Oxygen entering the chamber was captured and reacted with hydrogen, with the aid of a palladium catalyst, through which these gases were circulated. This reaction created water, which in turn was absorbed in desiccant to maintain a relative humidity below 10%. To confirm that oxygen was not in the system, we monitored the O_2 with a well-calibrated gas phase meter (NT-10, Coy Laboratory Inc., Grass Lake, MI) and a dissolved oxygen sensor (Visiferm DO, Hamilton Company, Reno, NV). These consistently measured <10 ppm in the gas phase and <1 ppb in the aqueous phase in nanopure water, respectively. The dye Rezasurin in a reduced aqueous solution was used as a simple visual verification of the presence of oxygen, because it turns from clear to pink upon the addition of dissolved oxygen (**Kreft**).

Steel Sample Material and Preparation

1018 Carbon Steel Composition

Disks 1 mm thick were cut from ½-inch-diameter rods of 1018 cold rolled carbon steel (MSC Industrial Supply Co., Melville, NY). ASTM specifications give the composition of 1018 steel as 0.15–0.20 carbon, 0.60–0.90 manganese, 0.040 phosphorous (max), and 0.050 sulfur (max) in weight percent, with iron making up the balance (**ASTM**). An FEM image of pearlite, a two-phased lamellar structure of alternating α-ferrite (88 wt %) and cementite (Fe_3C , 12%), is shown in Fig. 4. This was ubiquitous throughout our steel samples.

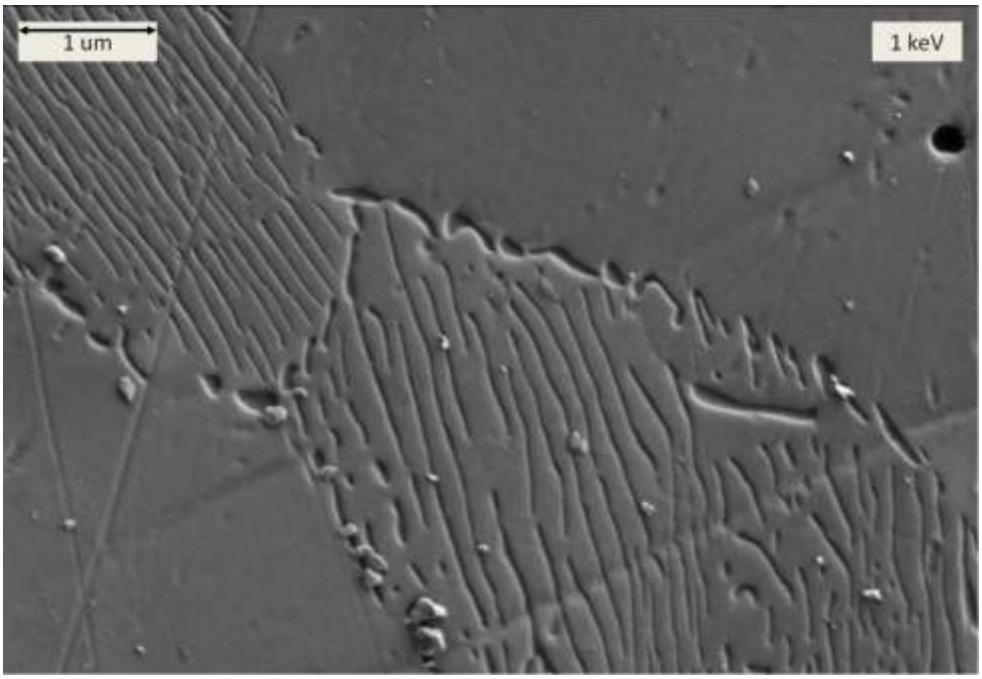

Figure 4: Pearlite in polished 1018 carbon steel. Carbide (Fe_3C) appears as fins in the ferrite matrix.

Coupon Polishing

Because of the surface morphology sensitivity requirements, the sample surface was highly polished. Samples arrived at the lab prepolished commercially (Lap-Rite Ind., Inc., Wood Dale, IL). They were given a final polishing to a submicron (30-50-nm) finish in-house. First, they were mounted on glass slides with silicone (polydimethylsiloxane) glue. They were then polished in the Allied Metprep 3 pH-3 Grinding/Polishing System (Allied High Tech Products, Inc., Compton, CA). Polishing suspensions were purchased from Allied. First, a three -micron polycrystalline diamond suspension was used. The polisher was set to drive for 30 minutes at 150 RPM at a 10-lb load and finish with a 30-second water rinse. Polishing solution was added about every minute. Next, a 1-micron suspension was used with identical settings on the polisher. The final polish took place in the Buehler Vibromet 1 Polisher (Buehler, Lake Bluff, IL) with a 40-nm colloidal silicon suspension. The polisher was allowed to run for one hour at the machine's speed setting of 5 (~60 rpm). Afterwards, to prevent polishing suspension from sticking to the sample surface, the samples were immediately rinsed with Nanopure water, followed by a rinse with acetone and drying with canned air. Next, they were removed from the glass with a razor blade and cleaned in a series of five-minute sonications in ethanol, chloroform, and acetone. Finally, they were dried with nitrogen and stored in the anaerobic chamber to prevent premature corrosion.

Elemental Analysis of Clean Coupon Surface

Elemental analysis of the clean surface was done using EDX and the Auger microprobe. The EDX in Fig. 5 shows primarily iron (~93 atomic percent) with a small

amount of manganese (~1%) and oxygen (~6%). This is reasonable because the surface is oxidized; furthermore sulfur and phosphorous should occur in amounts below the detection limit ($<10^{-1}$ atomic percent). The oxygen is present because of the rapid oxidation of the surface in the outside environment. However, recall that oxygen is a light element and its quantitation in EDX is not reliable; in particular Fe L-lines interfere with the O K-line.

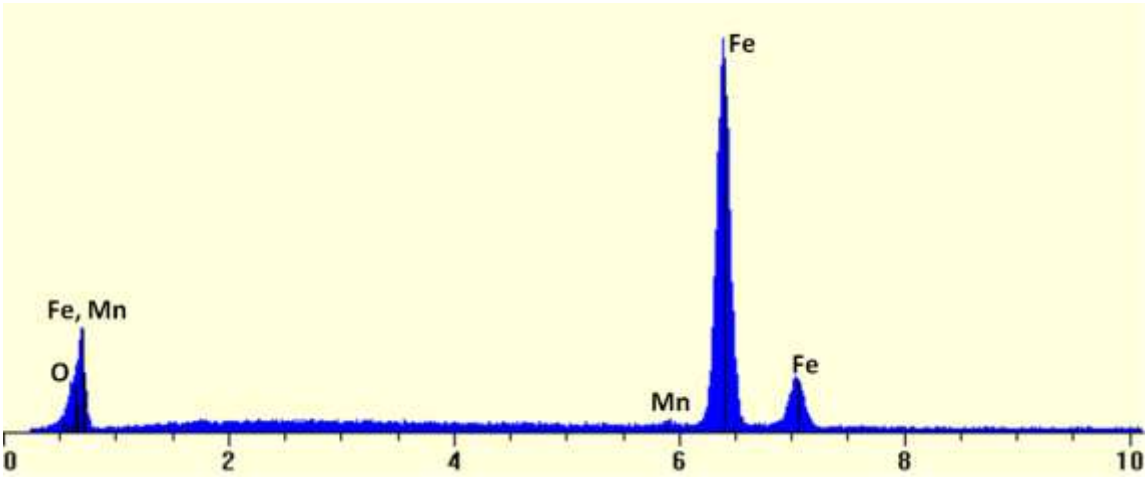

Figure 5: EDX spectrum of clean 1018 carbon steel surface. The atomic percentages are 93% Fe, 1% Mn, and 6% O.

The Fe and Mn K-line transitions of the elements lie between 5 and 7 keV, and these are the transitions most frequently used to quantify by EDX. Oxygen has a K- α transition at ~0.5 keV, which often overlaps with the Mn L- α and Fe L- α lines, making it difficult to resolve at low quantities.

While EDX shows the elemental composition of the entire excitation volume, Auger reveals the composition of the surface. Fig. 6 shows Auger microprobe data from a spot before and after the surface is sputter cleaned. There is carbonaceous material (mostly environmental hydrocarbons), and there is an iron oxide layer that readily

develops outside on the steel surface. Note that carbon is not detected in EDX. The final scan, after removing a layer a few nm deep by sputtering, shows what the surface would look like if it were unexposed to the outside atmosphere or other contaminants, because sputtering is done under ultrahigh vacuum.

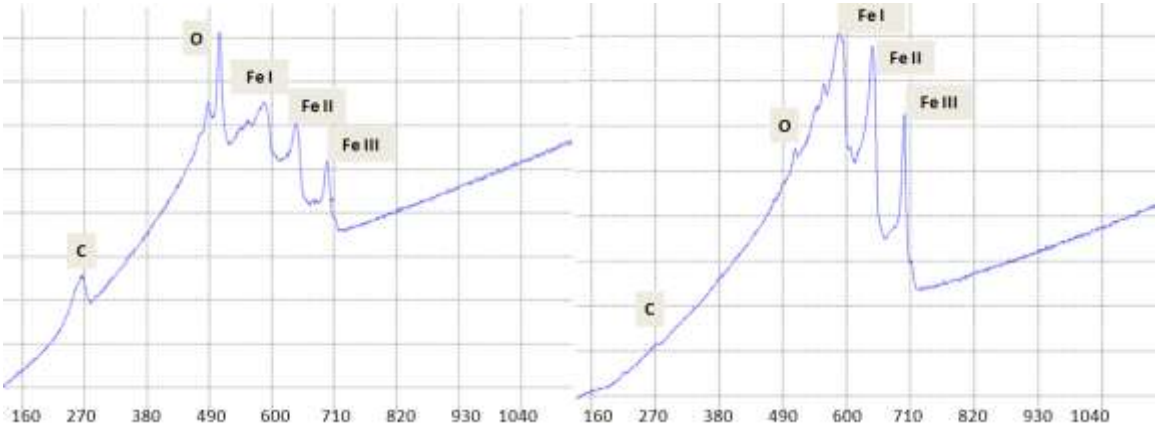

Figure 6: Auger scans (150-1150 eV) reveal iron with carbon and oxygen before (left) and after (right) contamination from the outside atmosphere is sputtered away.

MnS Inclusions

Industrially produced steel contains elementally unique inclusions, and these require analysis on an individual basis. Free sulfur in steel causes structural weakness via the formation of iron sulfide. Industry's current solution is to add manganese, which effectively scavenges the sulfur in the form of MnS inclusions. MnS has a lower solubility in metal and a lower conductivity than FeS, making it a less damaging impurity (**Wranglen**). These inclusions form as long, thin micro-wires (>100 μm) that run along the rolling axis of the rod. On the surface of traditionally prepared samples, cut perpendicular to the rod axis, they appear as spots (< 1 μm diameter), but investigation in

FEM of samples cut parallel to the rod reveals their true nature. FEM images showing samples cut in both manners are given in Fig. 7 for comparison.

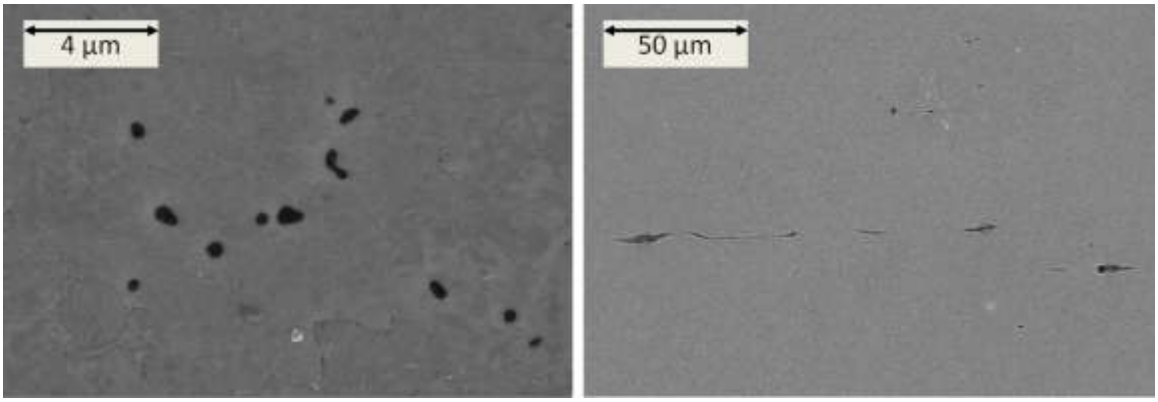

Figure 7: MnS inclusions (black features) in samples cut perpendicular (left) and parallel (right) to the rolling (rod) axis imaged with 20-keV primary electron beam.

MnS inclusions are widely distributed over the samples, and the most convenient way to image them in FEM is to use a large accelerating voltage. Fig. 8 shows that at a beam energy of 20 keV, the inclusions appear black, whereas at a lower energy (1 keV), they blend into the rest of the surface.

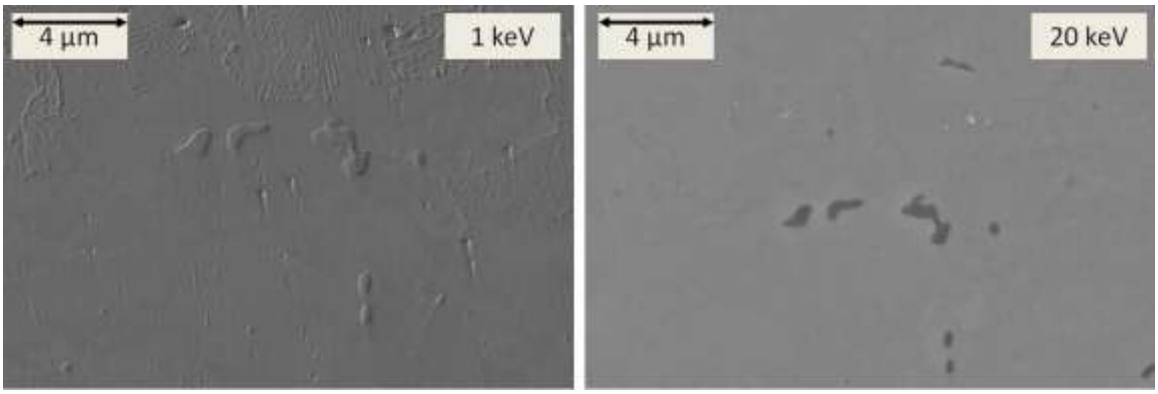

Figure 8: Inclusions on a sample surface cut traditionally (perpendicular to the rod axis) imaged with primary electrons at 1-keV (left) and 20-keV (right) energy. The two images are from nearly the same field of view.

MnS Inclusion Tracking So that individual inclusions could be analyzed in multiple instruments (i.e. FEM with EDX and AES) and be investigated before and after corrosion, a scheme was devised to keep track of inclusions on the steel surface by superimposing an oriented coordinate system. A cross visible to the naked eye was scribed onto the polished sample surface, as shown in Fig. 9. Next, the sample was mounted for investigation under the FEM in a particular orientation. The cross represented an oriented coordinate system that could be seen in detail with the electron microscope. Images were taken at a range of magnifications starting with a maximally wide field of view, to make identification of the general area easiest. Fig. 9 shows fields of view centered on the same spot at 67, 620, 1,860, and 71,000 times magnification. Inclusions that were tracked were found close to the cross so that they could be found again with the aid of morphological features in the scribed cross.

MnS Inclusion Elemental Composition The elemental composition of MnS inclusions was determined using EDX and Auger nanoprobe. Once again, it is important to stress that these two techniques yield different measurements that complement each other. The sizes of the inclusions are on the same order as the size of the excitation volume, so characteristic X- rays will be collected from both the inclusion and its immediate surroundings, which are iron. Field emission Auger nanoprobe collects information from a cube ~4-5 nanometers in dimension: the spatial resolutions of nanoAuger in imaging and spectral analysis match closely.

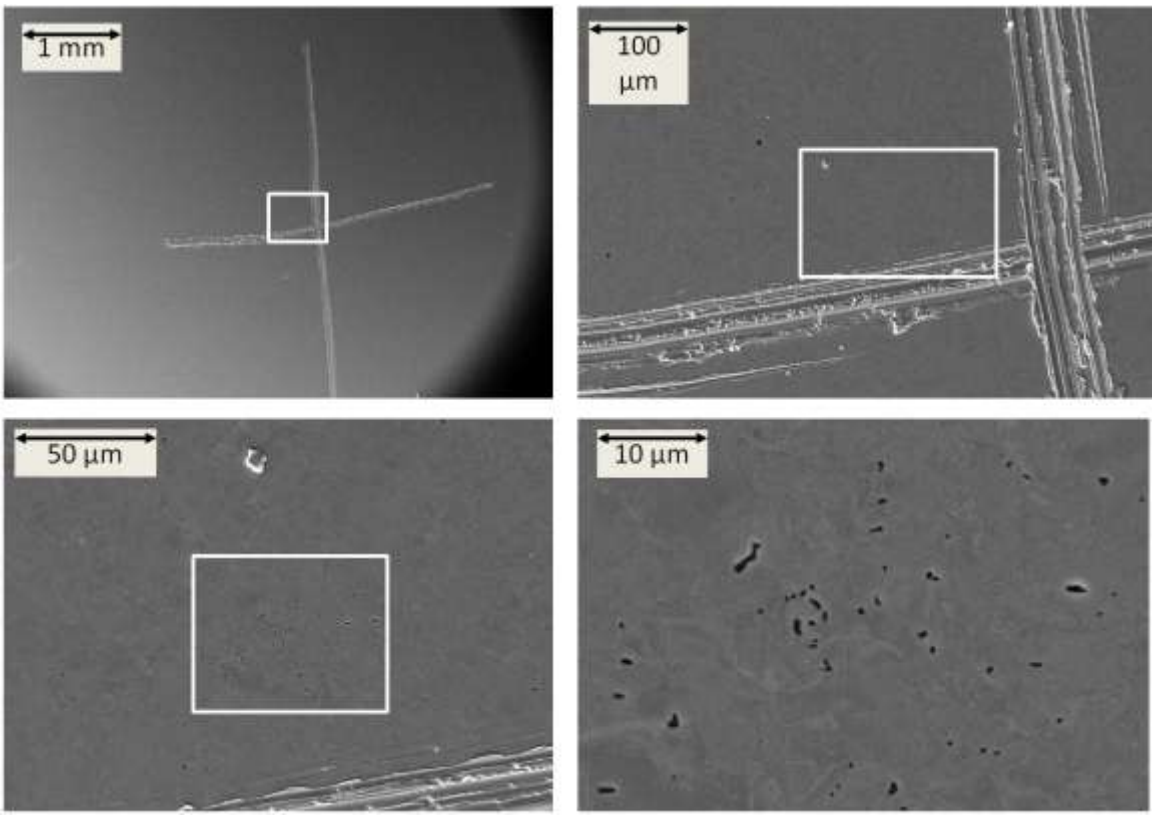

Figure 9: Reference mark for locating a particular inclusion among different instruments at various magnifications.

Surface elemental maps taken with the Auger nanoprobe of an individual MnS inclusion on a clean steel surface (labeled inclusion #1) are given in Fig. 10. The accompanying EDX taken from a spot centered on the inclusion is given in Fig. 11. The inclusion was not sputter cleaned, but care was taken to keep exposure to the outside atmosphere at a minimum.

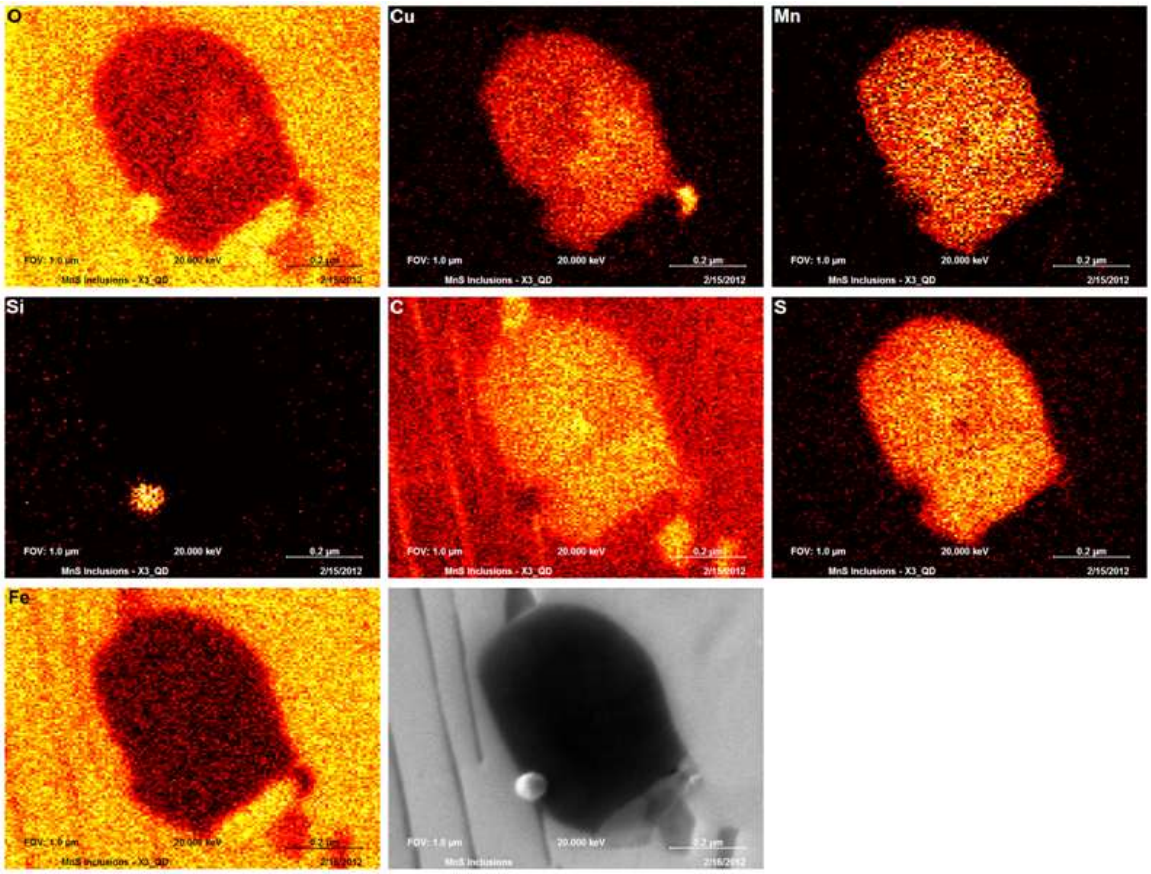

Figure 10: Inclusion #1. Auger elemental maps for (top row, left to right) oxygen, copper, manganese, (middle row) silicon, carbon, sulfur, and (bottom row) iron. The FEM image at 20 keV is at the bottom right. The field of view measures 1 µm across with a resolution of 256 × 256 pixels for mapping.

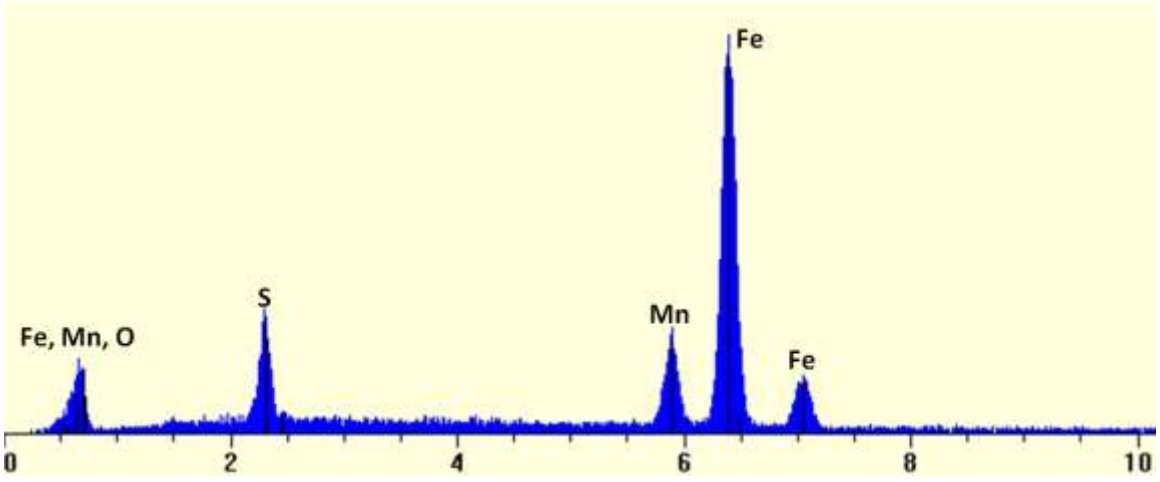

Figure 11: Inclusion # 1. EDX spectrum.

The nanoprobe Auger detects elements that the EDX does not. These are confined to a surface layer nanometers deep that can only be resolved using the surface-sensitive Auger. These are carbon and copper. The presence of carbon is easily explained as carbonaceous contamination from the outside environment. The presence of oxygen in EDX spectra, once again, is not resolved because the Mn and Fe L-lines overlap with the O signal. Auger microprobe revealed that oxygen is removed from the surface of the steel matrix after sputter cleaning (see Fig. 6 in Methods and Materials). The depth profile, shown in Fig. 12, of the clean steel matrix taken with the Auger nanoprobe confirms this. The bulk of the oxygen and carbon are removed from the surface after ~5 nm of sputtering.

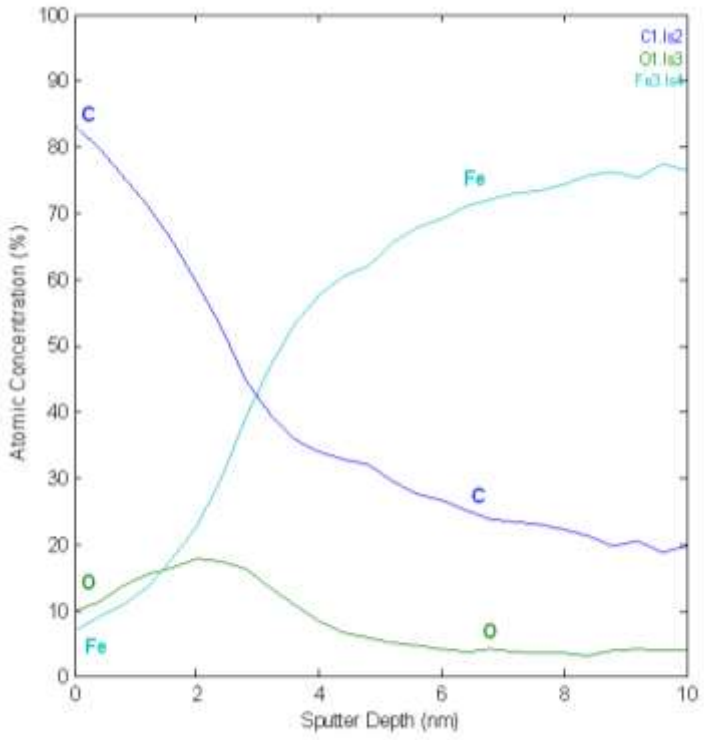

Figure 12: Depth profile taken from a 2 x 2 mm square on clean steel surface using an Auger nanoprobe.

The oxygen map in Fig. 10 shows that the MnS inclusion is relatively devoid of oxygen, compared to the surrounding matrix. The iron map in Fig. 10 shows that iron is found not only in the matrix, but within the inclusion as well, albeit in a lower concentration. Whether it exists as iron oxide contamination from the outside environment, as iron nitride within the entire inclusion, and/or combined with other inclusion elements cannot be determined before the inclusion is sputtered. Accounting for the presence of copper is plagued by the same mysteries as accounting for that of iron, although it is confined to the inclusion. It is most likely of the form Cu_2S. Some of these issues will be addressed in the coming sections. The silicon map in Fig.10 is of interest: a measure of the spatial spectral resolution of the Auger nanoprobe, it reveals a 40-nm silica polishing particle left behind. Pearlite is clear in both the FEM image and the Auger carbon map, where the high carbon content of carbide shines against the ferrite background.

A similar analysis was performed on another inclusion, labeled inclusion #2. Surface elemental maps taken with the Auger nanoprobe are shown in Fig. 13, and the accompanying EDX is given in Fig. 14.

This inclusion was not sputter cleaned, and the results are consistent with inclusion #1, except for one detail. This inclusion shows regions of high and low sulfur, labeled regions #1 and #2, respectively. This implies that the composition of MnS is not consistent and that there will be varying amounts of Mn, S, and Cu in the inclusions.

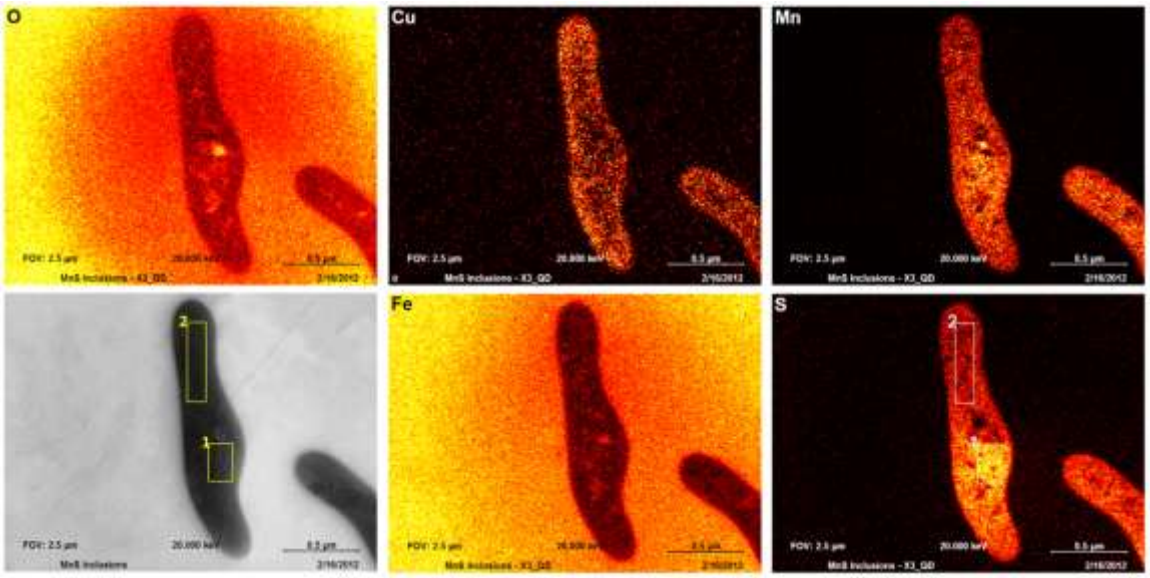

Figure 13: Inclusion #2. Auger elemental maps for (top row, left to right) oxygen, copper, and manganese. (Bottom row, left to right) FEM image at 20keV, Auger elemental maps of iron and sulfur. The field of view measures 2.5 x 2.5 μm with a scanning resolution of 256 × 256 pixels. Labels 1 and 2 show high- and low-S regions over the inclusion.

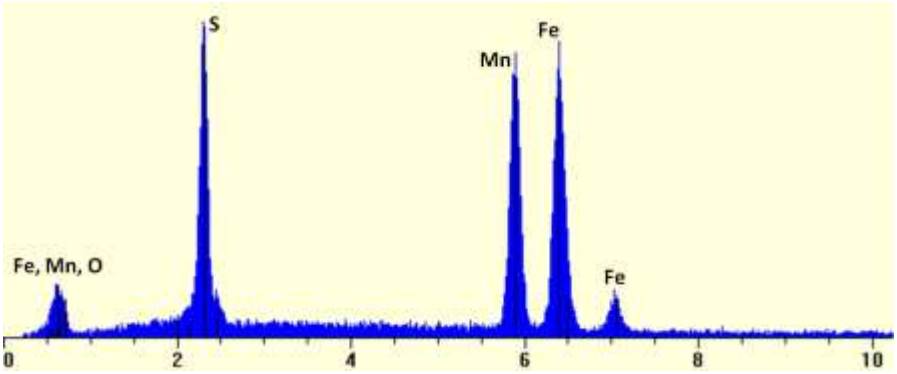

Figure 14: Inclusion #2 EDX spectrum.

The elemental compositions of inclusions #1 and #2 as measured by Auger nanoprobe and EDX are given in Table 1. Also shown are data from the depth profile (Fig. 12) and EDX spectrum (Fig. 5) of the steel matrix.

Table 1: Summary of elemental composition (by atomic %) of MnS inclusions labeled #1 and #2 and of the clean steel background as measured by Auger nanoprobe and EDX.

	C	**N**	**O**	**S**	**Cl**	**Mn**	**Fe**	**Cu**
# 1, AES	69	-	112	3.5	0.1	5.2	4.4	6.0
# 1, EDX	-	-	3.1	12	-	14	71	
# 2, area 1, AES	72	2.5	11	3.5	0.1	4.8	4.3	1.9
# 2, area 2, AES	81	1.2	8.3	1.6	0.1	1.6	4.1	2.6
# 2, EDX	-	-	4.9	26	-	34	35	-
Background, EDX	-	-	5.8	-	-	1.4	93	-
Background, AES	84	-	9.0	0.3	-	-	6.1	1.0
Background, AES, 10 nm removed	-	-	-	-	-	-	100	-

Another individual inclusion, labeled inclusion #3, was sputtered to remove 1 nm and then 50 nm, and elemental surface maps were taken using the Auger nanoprobe. The elemental surface maps in Fig. 15 were taken after 1 nm of sputtering. There is still much oxygen, indicating that the oxide contamination layer is deeper that 1 nm. Quantitative analysis from a spot centered on the inclusion, given in Table 2, also shows that a significant amount of carbon remains, indicating that the carbonaceous contamination is also deeper than 1 nm. The copper, sulfur, and manganese are still present and confined to the inclusion.

The elemental surface maps in Fig. 16 were taken after 50 nm of sputtering inclusion #3. The copper has vanished except for around the edges, indicating that the bulk of it was confined to a surface layer less than 50 nm deep. The copper is attributed to a layer of Cu_2S that forms on the surface of MnS inclusions. The oxygen has vanished as well, indicating that there are no metal oxides outside or within the inclusion and that the oxide layer is less than 50 nm deep. Also gone is the carbon signal, as shown in the quantitative analysis in Table 2.

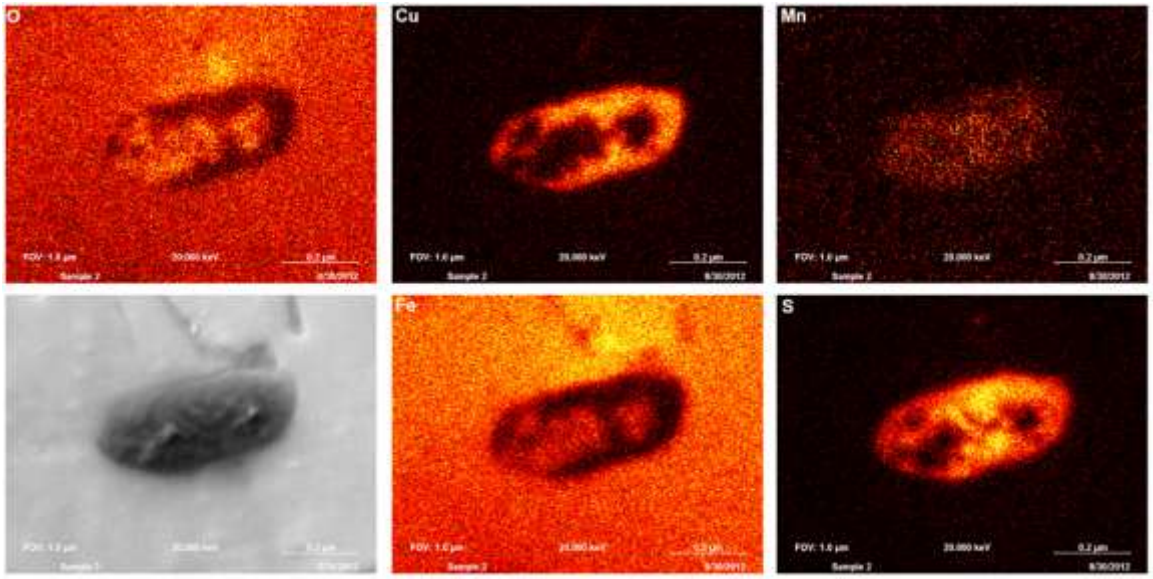

Figure 15: Inclusion #3 after 1 nm was removed. Auger elemental maps for (top row, left to right) oxygen, copper, and manganese. (Bottom row, left to right) FEM image at 20 keV, Auger elemental maps for iron and sulfur. The field of view measures 1.0 μm across with a scanning resolution of 256 × 256 pixels.

The carbonaceous contamination, as well, is less than 50 nm deep. Iron is still contained within the inclusion. This iron is not part of iron oxide. It may be iron sulfide or interstitial iron defects in the MnS lattice. Notice that the Cu signal is now confined to the edges of the inclusion in contact with the Fe matrix in the immediate surroundings of MnS. This disorder in the boundary will further strain the Fe matrix in the immediate surroundings of the inclusion.

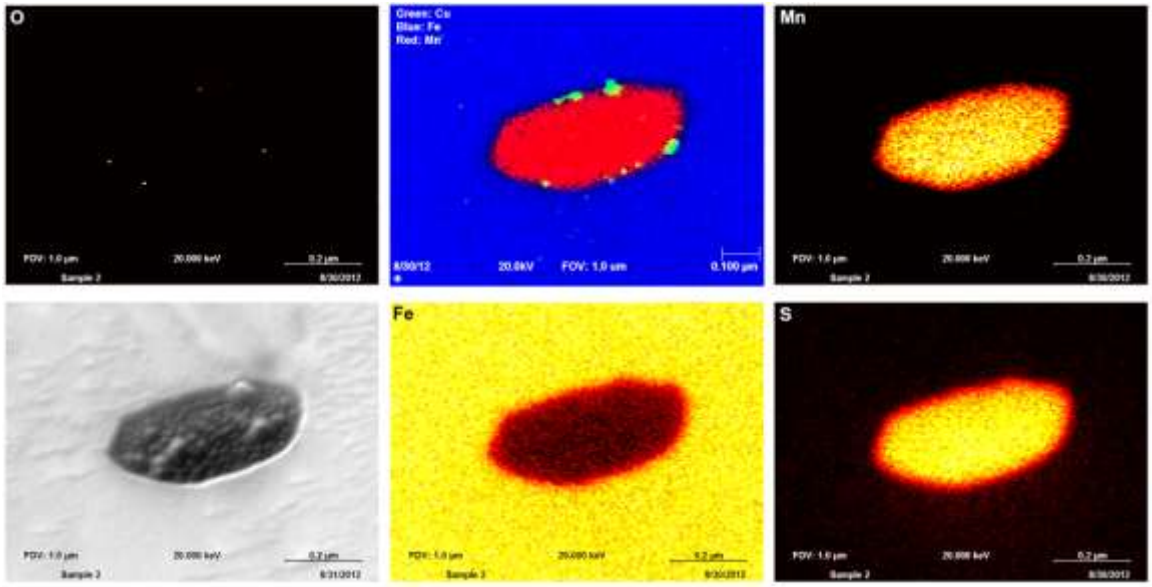

Figure 16: Inclusion #3 after 50 nm were removed. (Top row, left to right) Auger elemental map for oxygen, color map, Auger elemental map for manganese. (Bottom row, left to right) FEM image at 20 keV, elemental maps of iron and sulfur. The field of view measures 1.0 x 1.0 µm with a scanning resolution of 256 × 256 pixels. The copper map is illustrated as a color overlay with copper (green), manganese (red), and iron (blue).

Table #2: Summary of elemental composition (by atomic %) of MnS inclusion labeled #3 as measured by Auger nanoprobe after 1 nm and 50 nm were removed by sputtering.

	C	**O**	**S**	**Mn**	**Fe**	**Cu**	**Cl**	**Si**	**N**
#3, 1 nm removed	49	23	4.5	4.9	13	2.1	0.2	1.5	1.2
#3, 50 nm removed	-	-	30	37	32	-	-	-	-

Si was present, presumably as a uniform contaminant from the PDMS glue used to attach the samples to the glass slides for polishing. X–ray photoelectron spectroscopy (XPS) is an analytical technique that measures the normalized count of X–ray photoelectrons to resolve the concentrations of the different oxidation states of elements in a sample. The associated information volume is similar to that of Auger electrons, because both methods measure low kinetic electrons. XPS spectra taken from the

backside of the coupon (where it is attached by the glue) and the polished side, as a control, are given in Fig. 17. The quantitative analysis is shown in Table 3. It was found that the photoelectron signal from the silicon 2p transition (associated with the oxidation state of Si in PDMS glue) on the back was greater by almost 70%.

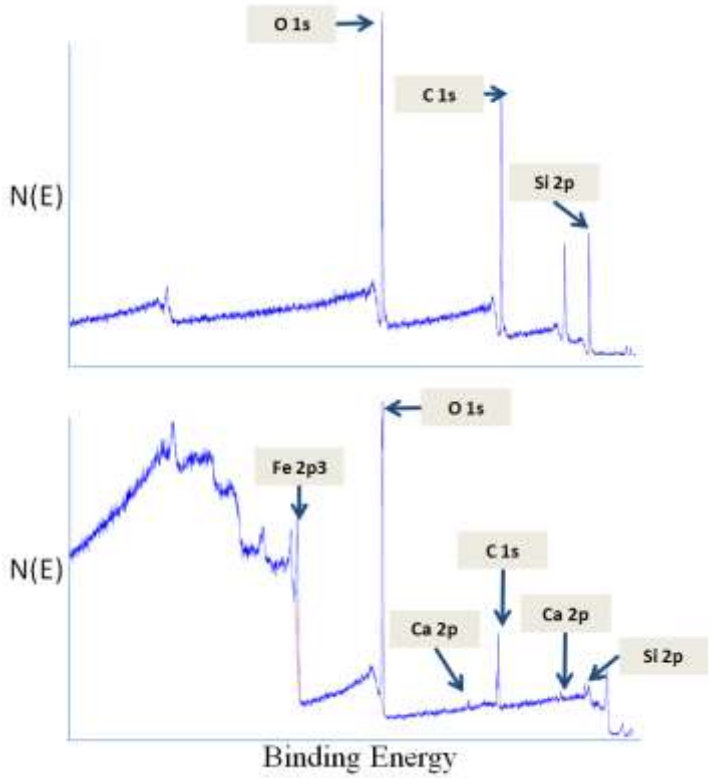

Figure 17: XPS spectra from back of coupon contaminated with PDMS glue (top) and polished side, as a control (bottom).

Table # 3: Summary of elemental composition (by atomic %) of polished and back surfaces of a clean steel coupon as measured by XPS. Note change in Si2p peak.

	Si 2p	**C 1s**	**O 1s**	**Ca 2p**	**Fe 2p3**
Backside	21.4	51.9	26.6	-	-
Polished side	3.2	27.7	55.9	0.5	12.7

A depth profile taken with the Nanoprobe Auger from another inclusion (inclusion #4) on the clean steel surface after 10 nm of sputtering is given in Fig. 18. It

reveals that the inclusion changes in elemental composition as a function of sputter depth. Note that the copper disappears after ~5 nm of sputtering. It is confined to the surface, suggesting a copper sulfide Cu_2S layer.

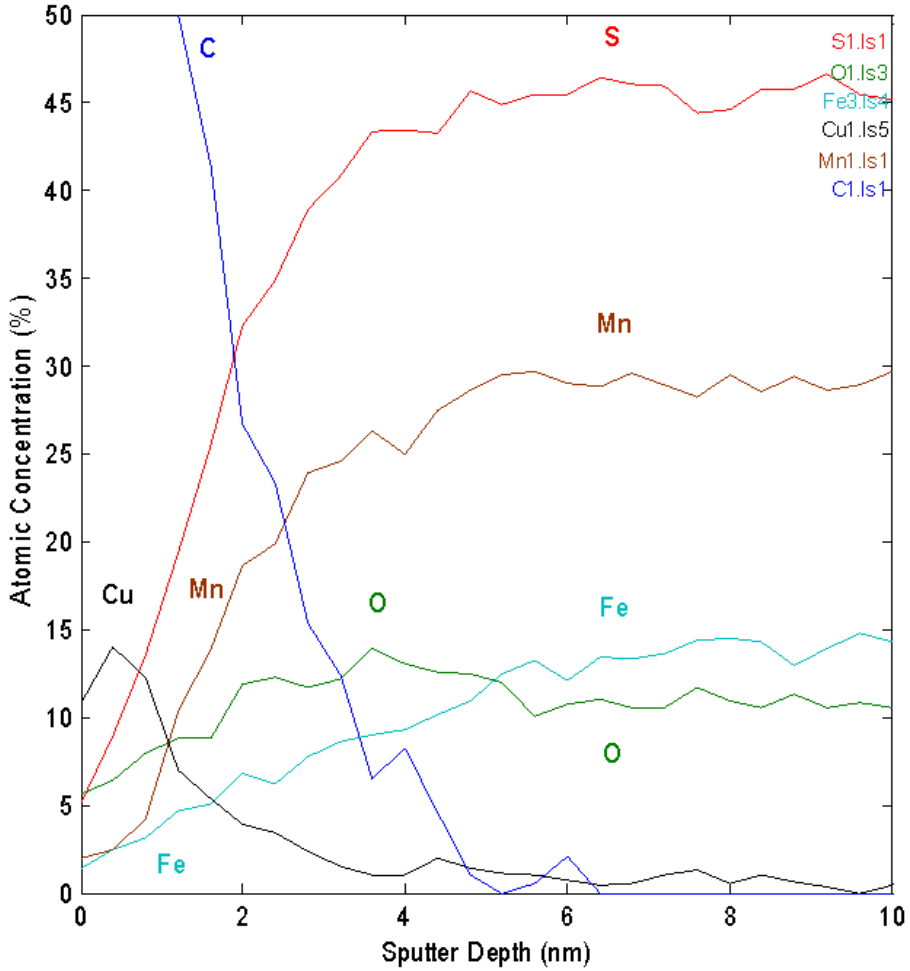

Figure 18: Inclusion #4 depth profile. Note that Cu disappears after ~5 nm.

Calcium was also present in this inclusion. The Auger nanoprobe elemental maps of the inclusion taken before (Fig. 19) and after (Fig. 20) 10 nm of sputtering reveal that it is below the Cu_2S layer, but its depth into the inclusion was not established by further sputtering.

The sample was held at a 30° tilt angle from the primary electron beam and at a 62° tilt angle from the focused Ar^+ ion beam used for sputtering. The ion beam was incident from the upper left corner of the field of view. The direction of the ion beam is clear from the remaining Cu_2S after 10 nm sputtering on the side of the inclusion facing the beam.

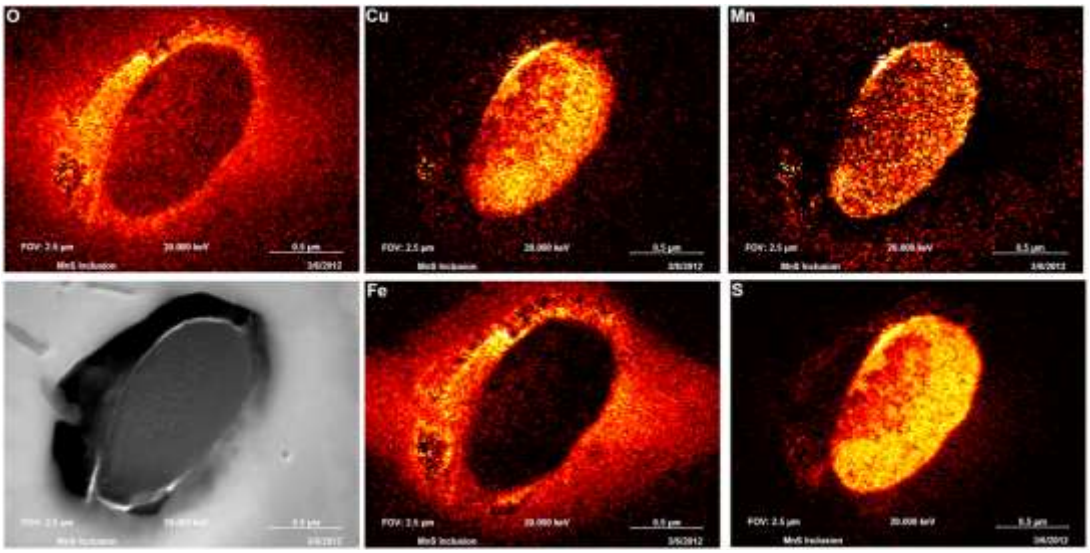

Figure 19: Inclusion # 4. (Top row, left to right) Auger nanoprobe surface elemental maps of oxygen, copper, and manganese. (Bottom row, left to right) FEM image at 20 keV, elemental maps of iron and sulfur.

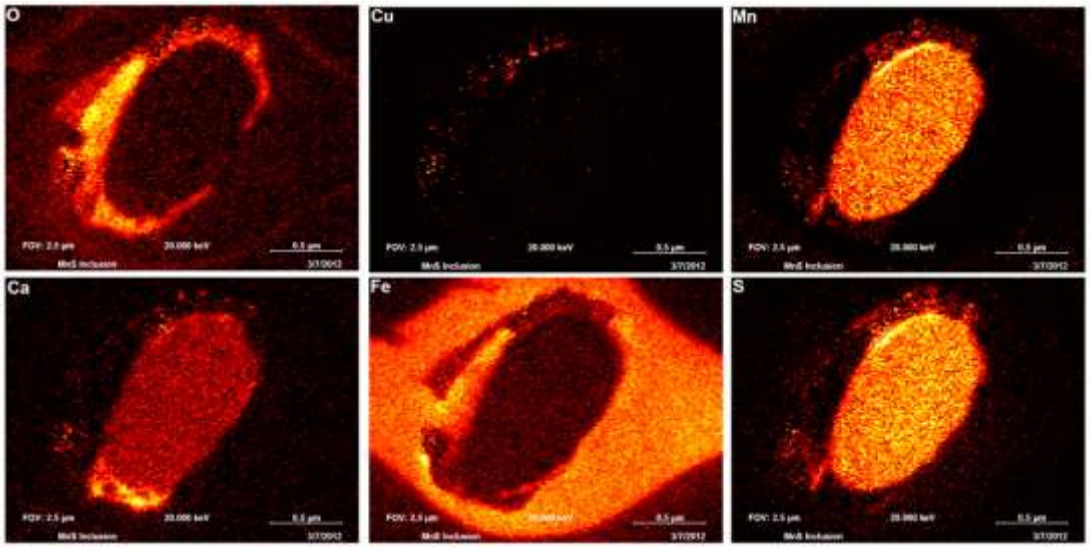

Figure 20: Inclusion #4 after 10 nm of sputtering. Auger nanoprobe surface elemental maps of (top row, left to right) oxygen, copper, manganese, (bottom row) calcium, iron, and sulfur.

A similar inclusion (inclusion #5) on a clean steel surface was analyzed using EDX in the FEM. The EDX spectrum in Fig. 21 shows that the inclusion must contain Ca throughout a volume extending at least a few microns into the surface.

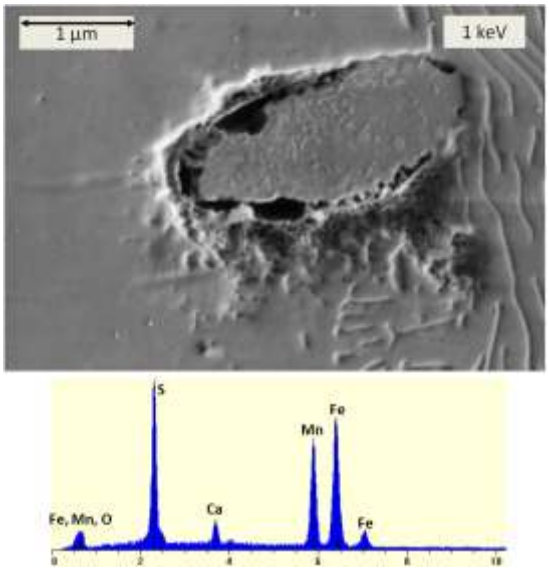

Figure 21: Inclusion #5. MnS inclusion with Ca impurity exhibits initiation of corrosion around edges.

There is clearly a prematurely corroded edge around the inclusion in both Ca-rich examples, as evidenced by the FEM images in Fig. 19 and Fig. 21. This is associated with a clear iron oxide region around the edge, as evidenced in the elemental maps of inclusion #4.

The quantitative analyses of the spots centered on inclusions #4 and #5 are given in Table 4.

Table 4: Summary of elemental composition (by atomic %) of MnS inclusions labeled #4 and #5 found using Auger nanoprobe (before and after sputtering away 10 nm) and EDX.

	C	**O**	**S**	**Mn**	**Fe**	**Ca**	**Cu**
# 4, AES	75	4.7	4.4	1.8	2.0	2.7	9.5
# 4, AES, 10 nm removed	-	-	4.0	30	4.7	25	-
# 5, EDX	-	4.8	29	27	36	3.8	-

Note the varying elemental compositions within and among inclusions. Within an inclusion this appears to be a function of depth. Other elements besides Mn and S are clearly contained within a number of these inclusions, and these may be confined to a surface layer, as is Cu_2S, or distributed throughout the inclusion below the surface, as is Ca. Ti is another element found in EDX spectra of MnS inclusions. These impurity elements may induce accelerated corrosion, such as around MnS inclusion borders, by introducing additional strain on the Fe matrix. Also of note is that the Mn:S ratio has considerable variation!

EDX analysis was the method used in-house to verify the content of an MnS inclusion during investigative studies in the FEM. To better understand the composition of inclusions as seen by EDX, X– ray spectra were obtained from a sample set of 133

pure MnS inclusions. The atomic percentages of Mn, S, and O were plotted as a function of atomic percent Fe and fit to linear relationships as shown in Fig. 22. The fits are given in equations 10–12.

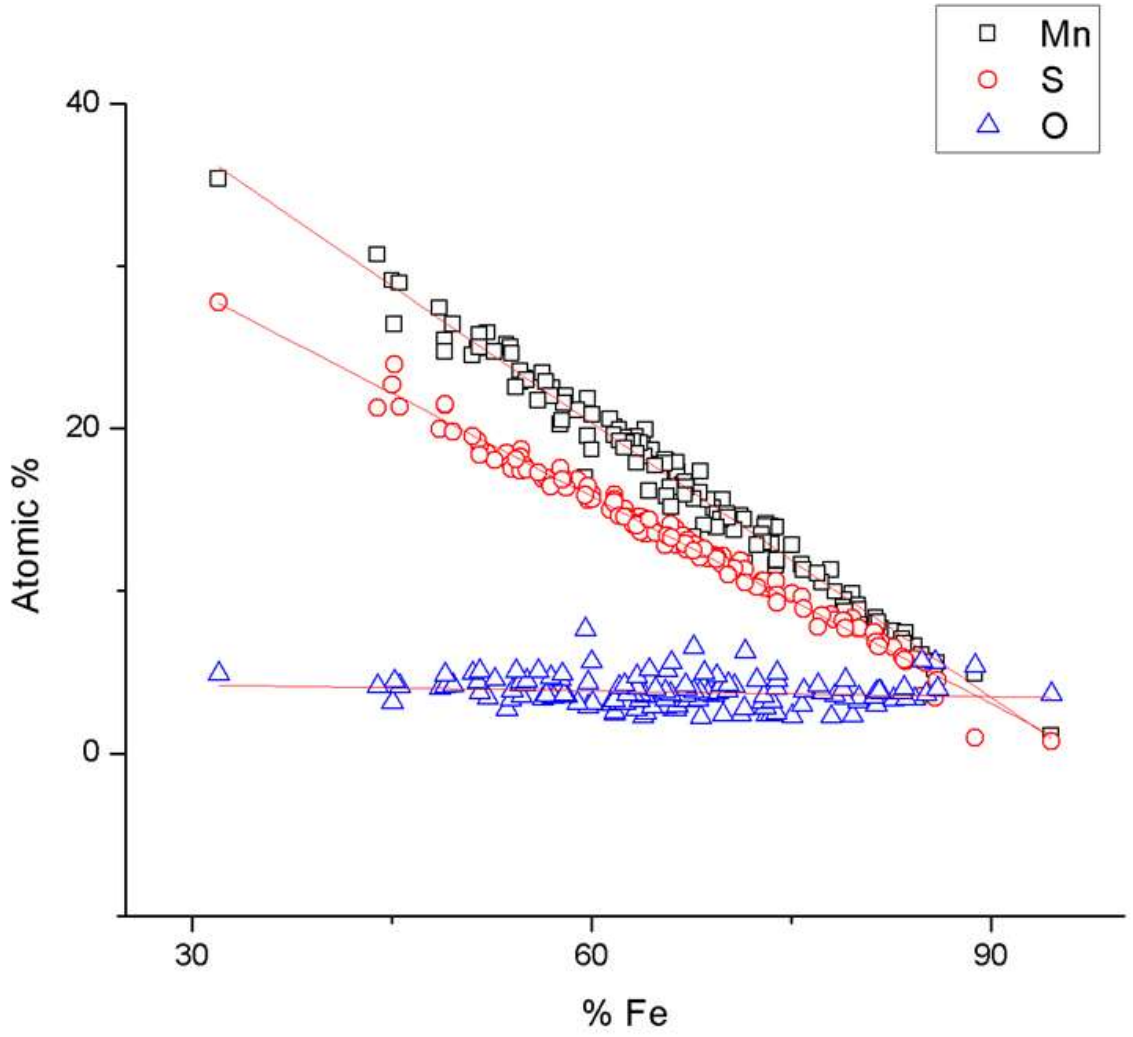

Figure 22: Chart of atomic percent Mn, S, and O vs. atomic percent Fe for a sample set of 133 MnS inclusions.

(10) $Mn = - 0.56\ Fe + 54.12$

(11) $S = - 0.42\ Fe + 41.28$

(12) $O = - 0.01\ Fe + 4.6$

The oxygen content is a constant (~4.6%), so it appears as a uniform background. According to the linear fits, for pure MnS (0% Fe), the ratio Mn/S is 1.31. For all inclusions, there is a greater density of Mn than S; this is contrary to the Auger data, which are highly surface-sensitive. The atomic percentage of iron varies between ~30 and 90%, and this is attributed to the variation in size of the inclusions, from tens to hundreds of nanometers. For example, in Fig. 23, inclusion #1 contained 32% Fe whereas inclusion #2 contained 82% Fe.

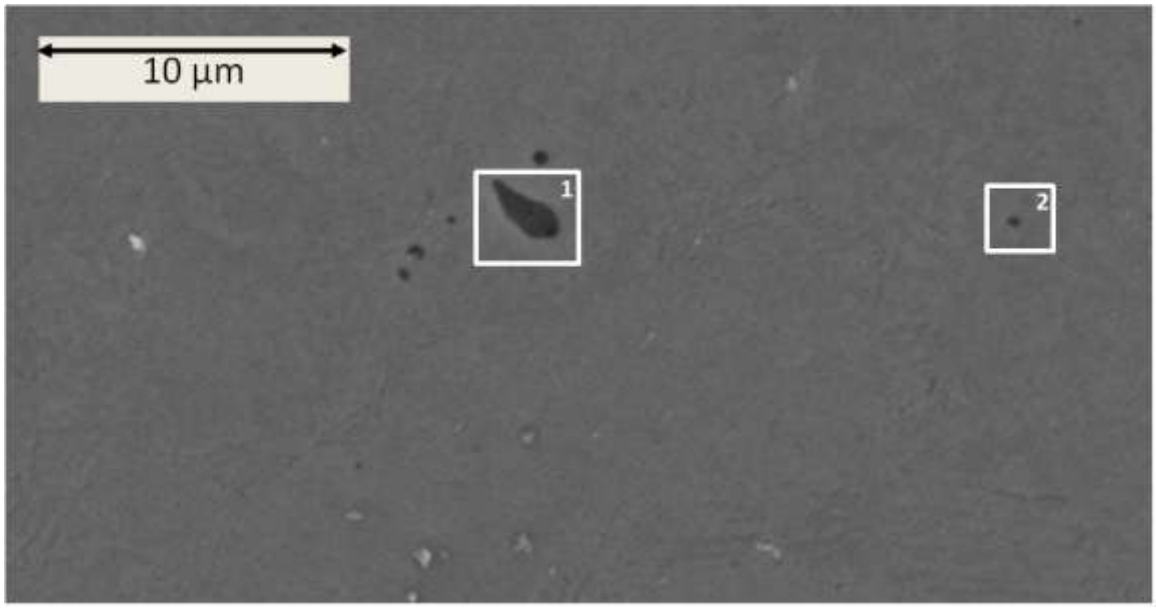

Figure 23: Comparison of MnS inclusions with high (2) and low (1) Fe content in their respective EDX spectra.

Inclusions of other compositions were found in pure form and combined with MnS in multi-mineral inclusions. Multiple minerals were seen as distinct heterogeneities in the inclusion, as shown in Fig. 24 and Fig. 25. Among these was a feldspar mineral, anorthite ($CaAl_2Si_2O_8$), with additional Mg oxide that was particularly common on the

steel surface. These inclusions were present in different ratios of feldspar to MnS and with other metal oxides and sulfides.

Surface elemental maps of a feldspar inclusion combined with MnS are shown in Fig. 24. The sulfur in the MnS is clearly restrained to one region, and the calcium and oxygen in the feldspar to another. Iron is homogeneously distributed throughout in relatively low abundance. These boundaries are disordered regions where enhanced residual strain may exist and lead to accelerated corrosion.

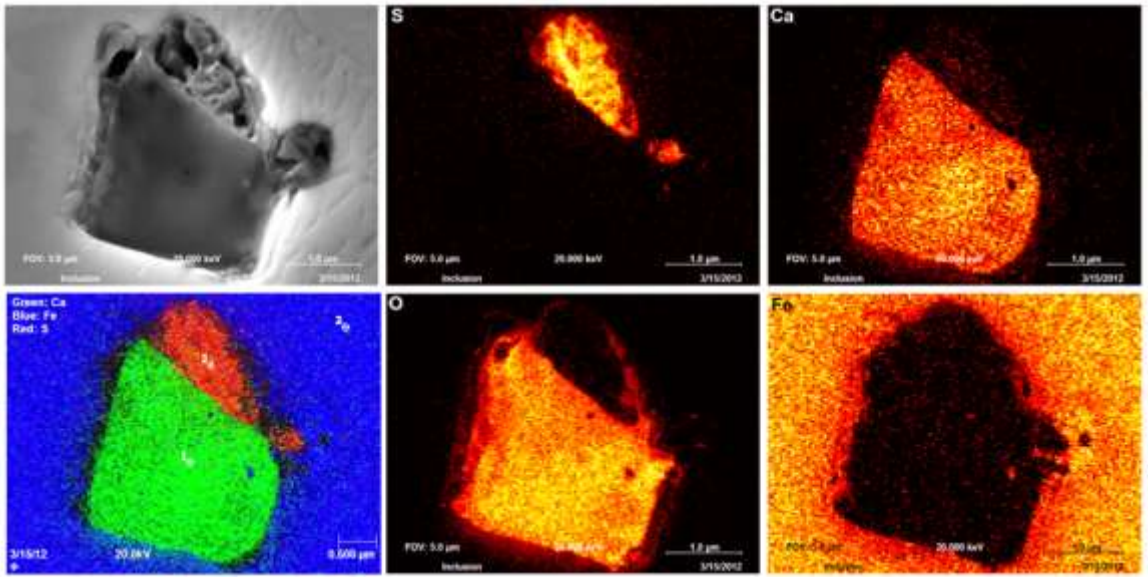

Figure 24: A MnS inclusion combined with feldspar. (Top row, left to right) FEM image (20 keV), Auger elemental maps of sulfur and. (Bottom row, left to right) Auger map showing iron- (blue), sulfur- (red), and calcium-rich (green) areas, Auger maps of oxygen and iron. The field of view measures 5×5 μm^2 and the scanning resolution is 256×256.

An FEM image at 1 keV and the accompanying EDX spectrum of a different feldspar inclusion combined with MnS are shown in Fig. 25. The high-resolution FEM image clearly shows heterogeneous zones, and this complements the accompanying EDX

spectrum, which cannot resolve these zones. Also clear is premature corrosion around the inclusion boundary.

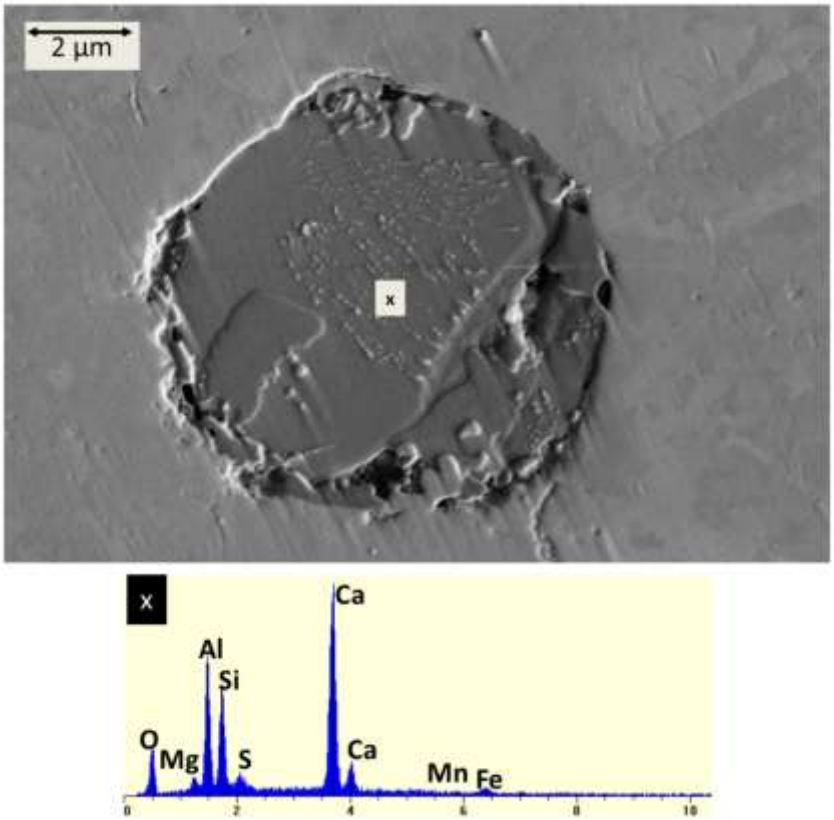

Figure 25: Inclusion of feldspar combined with trace FeS and accompanying EDX spectrum.

Strain Around MnS Inclusions

EBSD maps were taken from a clean steel surface containing MnS inclusions. The orientation map in Fig. 26 reveals that the steel is a poly-crystal with differently oriented BCC crystal domains (ferrite). The orientation is indicated by a color map related to the crystal's Miller indices. The map also shows that the complexity and number of domains increase around MnS inclusions. A derivative of the orientation map in Fig. 26 gives residual strain. This map is color-coded, with blue indicating low strain

and red indicating high strain. It is clear that the strain is associated with the crystal domains and orientation.

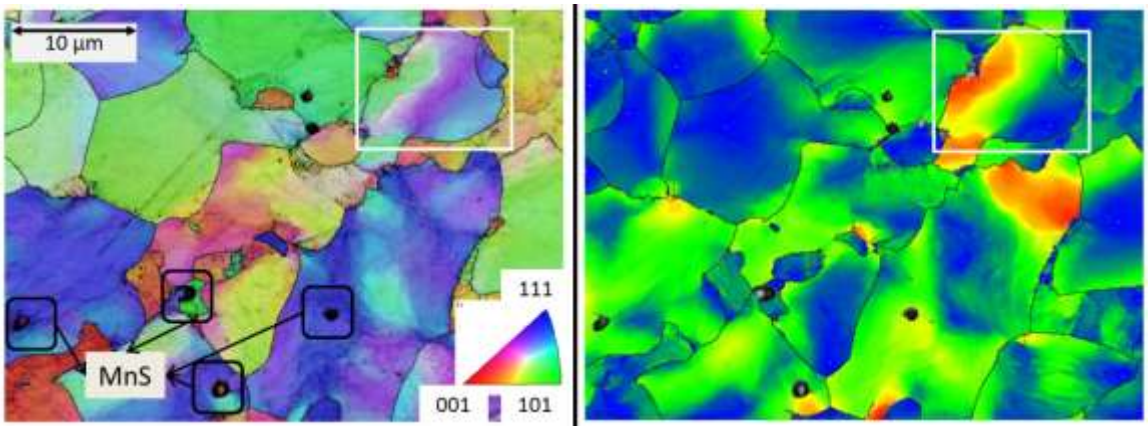

Figure 26: Left to right: Orientation and residual strain maps of the same field of view on a 1018 steel surface with MnS inclusions. MnS inclusions are indicated on the orientation map. The strain is color-coded along the visible spectrum from blue (minimum strain) to red (maximum strain).

Experiments

Introduction

Samples were exposed to both biotic and abiotic solutions with the intention of elucidating the consequences of SRB cellular metabolism on pitting corrosion in anaerobic sulfidogenic environments. The biotic solutions were cultures of SRB *Desulfoglaeba alkanexedens* (strain ALDC, herein referred to as such) and *Desulfovibrio indonensiensis* and their 0.2-um filtrates. The filtrates served as controls: the impact of the cells' active metabolism on the corrosion was removed by removing the cell matter from the medium. The cell cultures were grown in a basal saltwater medium. The abiotic solutions served as a further control which excluded any microbial metabolism whatsoever. These were sterile ALDC medium and a sulfide solution prepared by

dissolving nonanhydrate sodium sulfide salt ($Na_2S \cdot 9\ H_2O$) in sterile ALDC medium or nanopure water. A control pH of ~7.5 was chosen to match the physiological conditions of the SRB. All chemicals were purchased from Sigma Aldrich. Solutions were prepared with nanopure water and sterilization was done by autoclaving (at 21 psi steam and 120 °C for 20 minutes) and/or filtering through 0.2-µm membrane filters (Corning, Inc.).

Exposure was by immersing the steel coupon in 4 mL of corrosive media in 15-mL vials with butyl rubber stoppers that were capped with aluminum seals and crimped in the anaerobic chamber, making a doubly sealed anaerobic environment in which oxygen contamination was more surely eliminated. Coupons were placed on the bottom of the vial with their polished side face up.

The duration of exposure was chosen to be two weeks, unless otherwise indicated. This was a time frame in which the initiation of pitting could be observed.

After exposure, while in the anaerobic chamber, samples were removed and rinsed with pure anoxic water and dried by carefully wicking the moisture away with a Kimwipe. Elemental analysis of the surface was done using Auger microprobe, and the FEM was used in parallel with EDX to seek out sites of pitting corrosion on the surface and reveal their elemental composition. General corrosion was also assessed using Auger microprobe and FEM with EDX.

Removal of Corrosion Deposits

Samples were treated with a stripping chemical reagent herein referred to as "Clark solution" after analysis and reinvestigated in the FEM. Clark solution (pH ~-1) is prepared by adding 3.5 gm of hexamethylenetertramine to 1 L of 6 M hydrochloric acid

(HPLC grade), and is designed to strip away iron oxides and sulfides while leaving zero-valent metal intact. Treatment removed the corrosion products and biofilm after a brief (1–3 sec) immersion and subsequent rinse with pure anoxic water and drying with nitrogen. This revealed, without strongly affecting, the Fe surface itself beneath the corrosion/biofilm layer. If only half a coupon is immersed, then a clear demarcation between the "stripped" and intact regions forms, as illustrated in Fig. 27. The corrosion deposit is the perforated structure on the right-hand side. Analysis can be done on stripped and intact regions of the same sample, reducing time spent on the FEM.

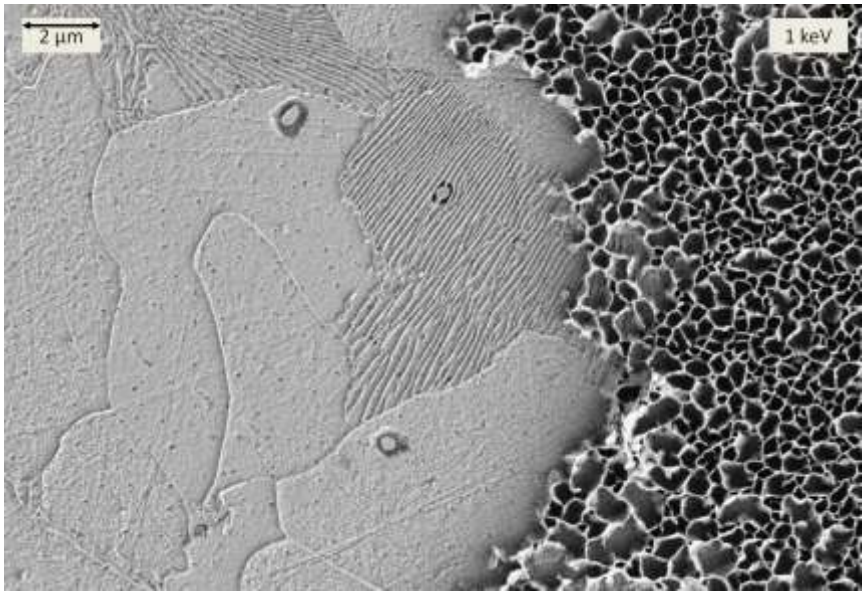

Figure 27: Removal of an iron sulfide corrosion deposit from a steel surface using Clark solution. Only half of the coupon was stripped, and so the demarcation between the two regions is clear.

Clark solution also selectively dissolved the tips of the MnS micro-wire inclusions on the clean steel surface. The FEM images in Fig. 28 show a group of MnS inclusions before (left) and after (right) exposure to Clark solution for seven seconds. The low-yield secondary electron emission from where the inclusions previously were

demonstrates that they have gone away. Notice that the surrounding zero-valent iron is not affected. In the EDX spectra, very few Mn or S characteristic X- rays are detected. The X–ray detector is oriented at a 55 degree angle to the normal of the sample surface and primary electron beam. Low-energy X–rays are strongly attenuated by their passage through the iron matrix between the excitation volume and the X–ray detector, indicating pit depth.

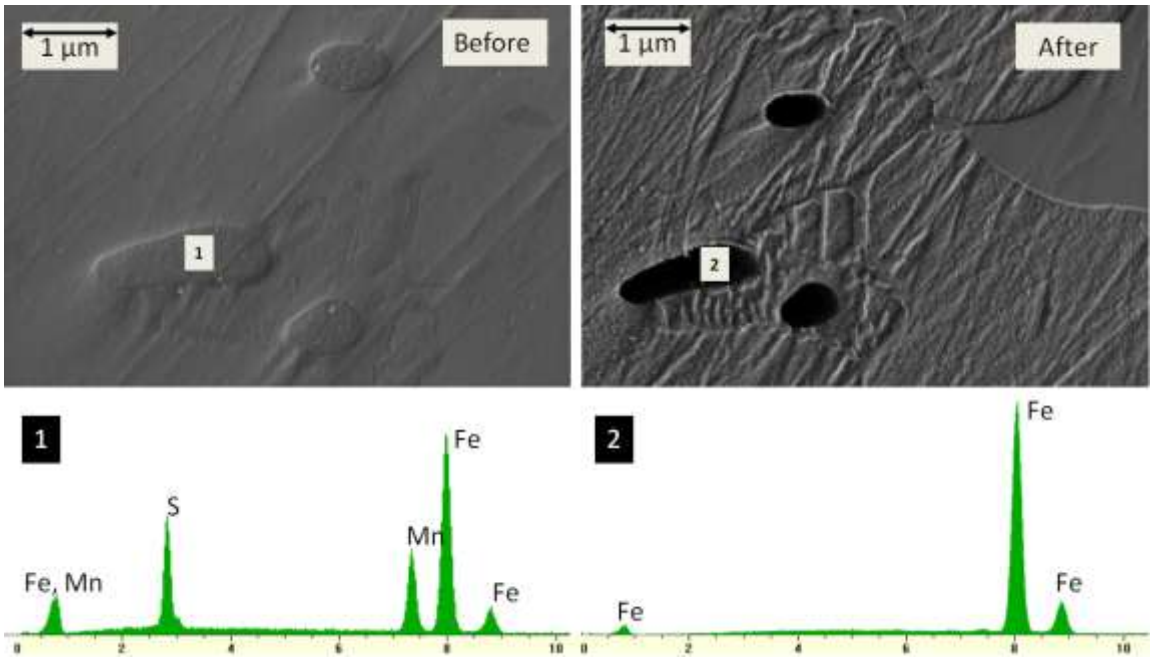

Figure 28: (Top) FEM at 1 keV and (bottom) EDX of MnS inclusions (left) before and (right) after treatment with Clark solution.

AFM is a technique in which the displacement of a cantilever is measured to obtain a highly resolved (nm to sub-nm) 3-D picture of surface morphology. As the cantilever rasters across the surface, it is deflected by morphological features. This deflection moves a laser point on a photodetector that translates into the surface morphology.

The AFM scans in Fig. 29 show that the depth of the inclusions increased after treatment with Clark solution. The depth after treatment cannot be measured, because the dimensions of the AFM tip will not allow it to reach the bottom. Originally, the inclusions possessed a depth of ~30 nm, which is comparable to the size of a silica polishing particle. It is speculated that the polishing process removed the slightly softer inclusions preferentially over the surrounding iron matrix.

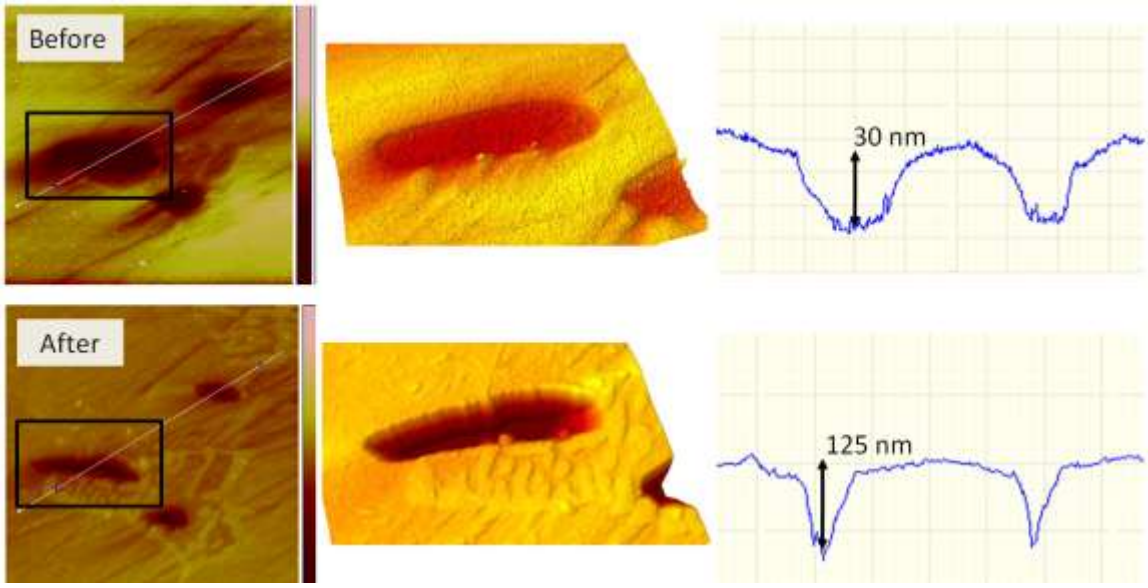

Figure 29: AFM scans of the same inclusion (top) before and (bottom) after treatment with Clark solution.

The Clark solution dissolved enough of the inclusion to conceal it from the AFM, FEM, and EDX, but these inclusions penetrate hundreds of microns into the steel surface. Clark solution removes only the very top region of the inclusion to a depth most likely comparable to its width.

Mass Loss Experiment

General corrosion was further assessed from the mass lost by the steel coupon. This was measured by taking the mass difference between the coupon before corrosion, and the coupon after corrosion and treatment with Clark solution. Samples were weighed in a Metter Toledo, model MT5 scale, which possessed a resolution of 1 microgram.

Corrosive Media

ALDC Media

The ALDC were grown in a brackish water mineral medium containing 25 mM basal sulfate (Appendix 1) (**Widdel**). As a first step, the medium was distributed into serum bottles using aseptic anaerobic techniques. After sterilization the medium was supplemented (assuming a one-liter volume) with 3.0 g of $NaHCO_3$ (from a 10% stock solution), 10 mL of an RST vitamin solution (Appendices 2 and 3) without mercaptoethanosulfonic acid and 0.01% yeast extract. The medium was reduced with 0.01 g of cysteine-HCl and 0.01 g of $Na_2S{\cdot}9H_2O$ to obtain a final pH of 7.2–7.3. The reducing agent introduces a small amount of H_2S (0.05 mM concentration), although most of this is meant to be absorbed in a reaction to remove any oxygen from the medium by reducing the dissolved oxygen and oxidizing the H_2S to thiosulfate ($S_2O_3^{2-}$),given in equation 13.

(13) $2\ S^{2-} + 2\ O_2 + H_2O \rightarrow S_2O_3^{2-} + 2\ OH^-$

Decane (5–10 mM) was provided in excess. The medium prepared in this way is herein referred to as “sterile ALDC medium.”

Bottles of sterile ALDC medium were anaerobically inoculated with 10–20% (by volume) of two month-old culture provided by the laboratory of Dr. J. Suflita of the University of Oklahoma at Norman, OK. The cultures were incubated at 30 °C under a N_2/CO_2 (80:20) gas phase for two months before use in corrosion experiments. At this stage, the media had concentrations of 5×10^6 cells/mL (**Davidova**). Herein, this is referred to as ALDC cell culture.

D. indonensis Media

D. indonensis were grown in an identical sterile medium, only with the substitution of 20 mM lactate ($CH_3CH(OH)COO^-$) for decane. The medium was anaerobically inoculated with 10% of in-house cell culture at maximum growth (after ~30 hours incubation). This was used in corrosion experiments after inoculation and only a few days of incubation under identical conditions as ALDC. Herein, this is referred to as *D. indonesiansis* (or *D. indonensis*) cell culture.

Abiotic Sulfide Control

Nonahydrate sodium sulfide salt is a water-soluble solid that completely dissociates to give strongly alkaline solutions according to the reaction in equation 14.

(14) $Na_2S + H_2O \rightarrow 2\ Na^+ + HS^- + 0H^-$

The equilibrium of sulfide species (H_2S, HS^-, and S^{2-}) is then established according to the solution pH (adjusted to 7.4) as described in the introduction. The control concentration of sulfide was chosen to reflect the maximum amount of sulfate reduction throughout the lifecycle of a batch of cell medium; this gave an upper bound to

the abiotic sulfide corrosion possible in our biotic solutions. When a batch of cell medium is grown, it starts with an initial amount of sulfate, which the SRB consume as they respire. It is important to stress here that for every one sulfate ion consumed, one sulfide ion is produced: the mass of sulfur is conserved. The control concentration of sulfide was chosen to match the starting concentration of sulfate, which was 25 mM. In reality, however, the biotic solutions averaged ~16 mM sulfide concentrations; they never reached the ultimate maximum. This was determined later by measurements of SO_4^{2-} concentration via ion chromatography (Thermo Scientific). The sulfide concentration was taken as the difference between the starting (25 mM) and final (as measured) sulfate concentrations.

The abiotic sulfide media were prepared under an anaerobic hood by dissolving sodium sulfide salt in a sterile deoxygenated ALDC medium or nanopure water to a final sulfide concentration of 25 mM. The pH was then adjusted to the physiological value of 7.4 by titration with 1:20 v:v sulfuric acid. Before being used to corrode a steel coupon, the solution was sterilized by filtering through a 0.2-μm filter. Herein, the medium prepared with sterile ALDC medium is referred to as the abiotic sulfide control. Experiments with Na_2S in deoxygenated nanopure water are also referred to as such.

RESULTS

General Corrosion

Measurable corrosion was induced on 1018 carbon steel coupons by exposure for two weeks to the corrosive media (sterile ALDC medium, 25 mM abiotic sulfide in sterile ALDC medium, ALDC culture, ALDC culture filtrate, *D. indonensis* culture, and *D. indonensiensis* culture filtrate). This was indicated by the observation of corrosion products on the surface, as measured by EDX and AES, and confirmed visually in the FEM. Fig. 30 compares general corrosion deposits on coupons exposed to the abiotic sulfide solution (left) and the ALDC medium filtrate (right). These deposits were observed uniformly covering the entire sample surfaces.

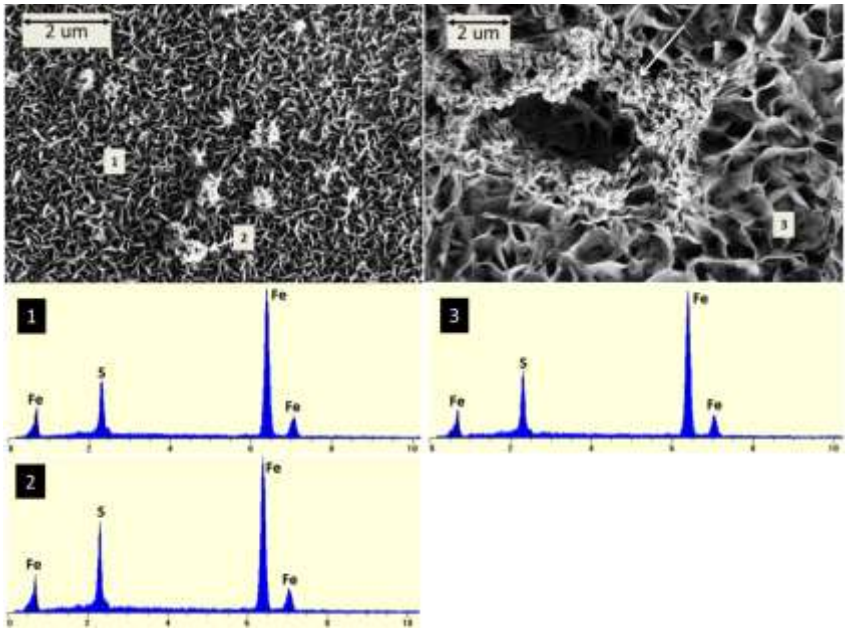

Figure 30: Comparison of corrosion deposits on coupons exposed to (left) abiotic sulfide control solution with [Na_2S] = 25 mM for 11 days and (right) ALDC filtrate for two weeks. Note the high-sulfur deposits atop uniform background in EDX spectrum 2 and similar deposits on a biologically corroded sample (pointed out with a white arrow in the image on the right).

The EDX reveals that both corrosion deposits are iron sulfide (FeS) and that they contain a similar amount of sulfur. The deposits are morphologically similar. They are arranged in chimney structures that may facilitate the passage of corrosion reactants between the metal surface and the bulk solution. However, the two images in Fig. 30 were taken at similar magnification, so it appears that biotic solutions produce larger, wider, and more open chimney structures. High sulfur clumps are seen on top of the uniform FeS background, as well. One of these is pointed out in Fig. 30, in the spectrum taken from the point labeled #3. Similar deposits were seen on coupons corroded by SRB as well, and an example of these is pointed out by the white arrow in Fig. 30.

Fig. 31 clearly shows a blister that has burst on the surface exposed to the abiotic solution.

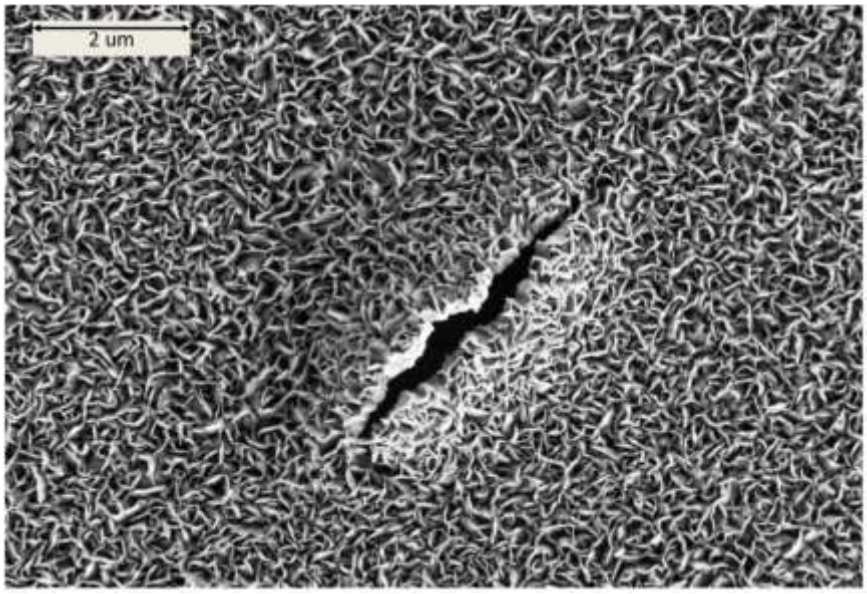

Figure 31: Cracking of FeS corrosion deposit on sample corroded by abiotic sulfide solution with [Na_2S] = 25 mM for two weeks.

These structures are attributed to density differences between FeS and Fe: corrosion takes place at the bottom of FeS deposits on the clean Fe surface, and as the fresh FeS deposits form on the clean surface they push up the old corrosion deposits accumulated above them, causing cracking and chimney structures.

A steel sample surface after exposure to the sterile ALDC medium, without any abiotic sulfide, is shown in Fig. 32. The least severe general corrosion was seen on these samples. The general corrosion layer was not deep enough to be detectable by EDX; however, some etching of the surface is clear in FEM. Deposits high in sulfur were seen as well. The sterile ALDC medium did contain 0.05 mM of sulfide because during its preparation some trace sulfide was introduced into the medium to scavenge any trace dissolved O_2 in solution.

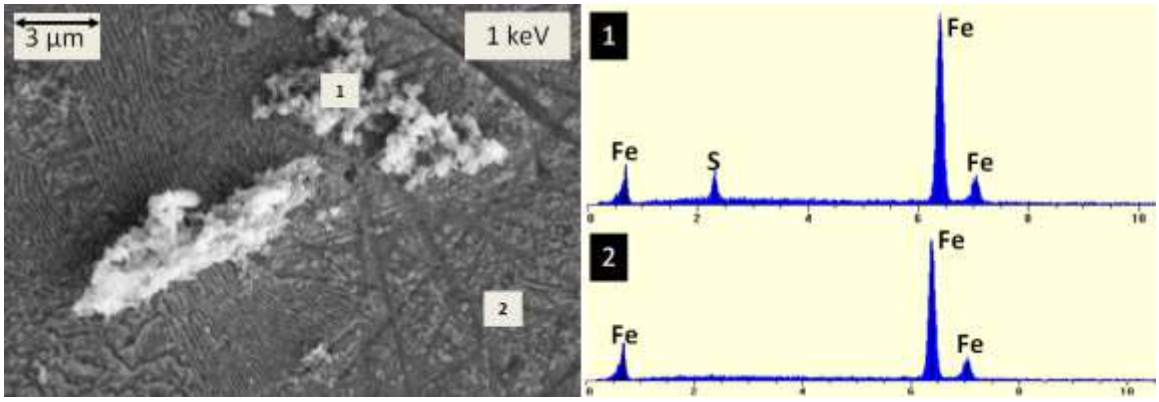

Figure 32: Coupon surface after exposure to sterile ALDC medium for two weeks with $[Na_2S]$ = 0.05 mM. Note trace amount of FeS corrosion deposit. However, the majority of the surface was not corroded.

Auger Analysis

Depth profiles taken by AES microprobes of samples exposed to sterile ALDC medium, abiotic sulfide control and ALDC cell culture are shown in Figures 33–35,

respectively. These confirm that the corrosion proceeds through the deposition of an iron sulfide layer, and that the depth of this layer is greatest in the biotic solution. The sputter rate is approximately 180 nm/minute.

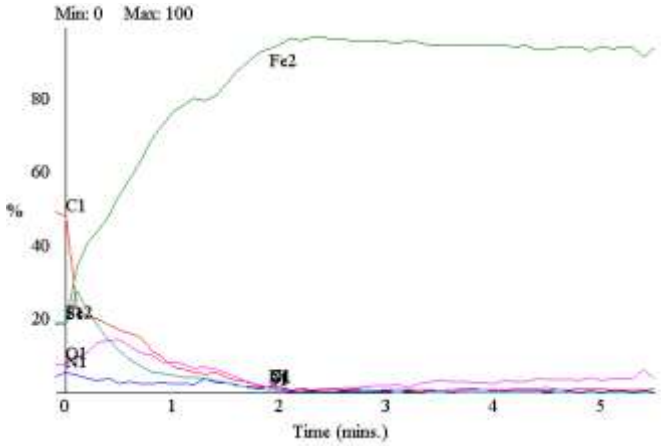

Figure 33: Depth profile of coupon surface corroded by sterile ALDC medium for two weeks with [Na_2S] = 0.05 mM. The depth profiles of elements are color-coded as follows: Fe2 (green), C1 (orange), O1 (pink), N1 (blue), S1 (teal). The x-axis is sputtering time. The y-axis is atomic percent. The deposit is ~360 nm thick.

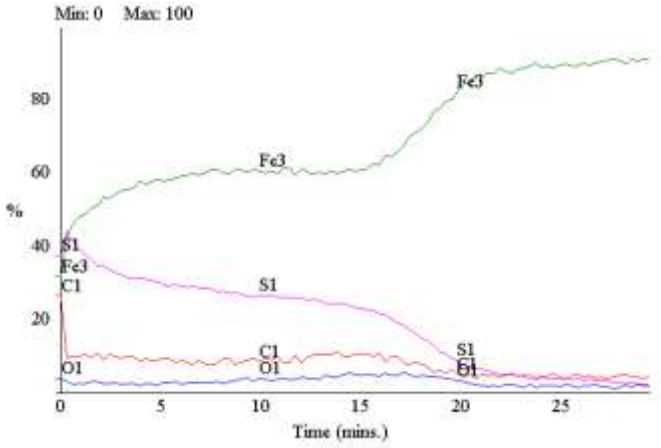

Figure 34: Depth profile of coupon surface corroded by the abiotic sulfide control with [Na_2S] = 25 mM for two weeks. The depth profiles of elements are color-coded as follows: Fe2 (green), C1 (orange), O1 (blue), and S1 (pink). The deposit is ~1.8 µm thick.

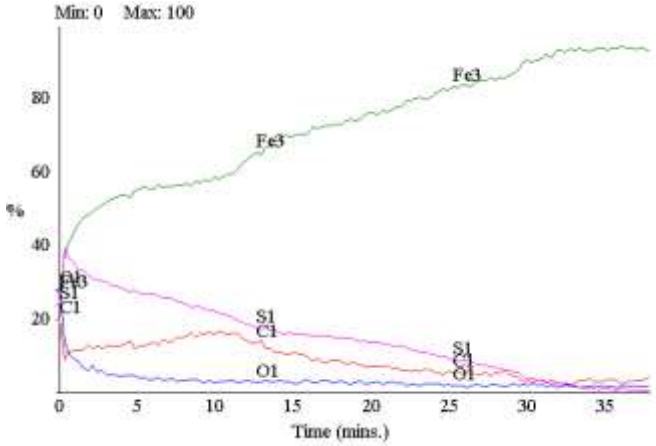

Figure 35: Depth profile taken of a coupon surface corroded by ALDC cell culture for two weeks. The depth profiles of elements are color-coded as follows: Fe2 (green), C1 (orange), O1 (blue), and S1 (pink). The deposit is ~3.6 microns thick.

Mass Loss Results

Mass loss was taken as a measure of the rate of general corrosion expressed in units of mass lost per unit surface area per day. Five samples each were exposed to sterile ALDC medium (for 225 hours), abiotic sulfide solution (for 60 hours), and ALDC filtrate (for 44 hours). The mean corrosion rates were extrapolated and are given in Table 5. The standard deviation in this rate among the sample set is given (in the same units), assuming a normal distribution.

Table 5: Summary of mass lost by coupons exposed to sterile ALDC medium with $[Na_2S]$ = 0.05 mM, abiotic sulfide solution with $[Na_2S]$ = 25 mM, and ALDC filtrate.

	Exposure time (hours)	Rate (µg/cm^2/day)	Standard Deviation
Sterile ALDC medium	225	10	1.67
Abiotic sulfide solution	60	27	2.5
ALDC filtrate	32	84	1.7

It was found that the biotic solution corrodes steel at a rate far exceeding those of the abiotic solutions. The abiotic sulfide corrodes steel at a faster rate than the sterile ALDC medium. This suggests that ALDC is a highly corrosive organism, and we hypothesize that the metabolic products of this organism participate in cathodic processes.

Preferential Corrosion Within Grains and Around Cementite

Coupon surfaces exposed to ALDC filtrate were clearly preferentially etched by the corrosion at the microscale. An FEM image taken of a coupon surface after exposure to ALDC filtrate and removal of corrosion deposits with Clark solution treatment is shown in Fig. 36. It can be seen that different areas were corroded at different rates. The reason for these differences is attributed to the differences in residual strain over the surface. The areas that had more residual strain corroded at higher rates.

Left behind after the corrosion has deeply etched the steel surface is the cementite (Fe_3C) phase that was part of the two-phase lamellar pearlite. In the initial corrosion processes this serves as a measuring stick for establishing the depth of ferrite material removed by corrosion. The cementite phase of pearlite is substantially more resistant to corrosion than the surrounding ferrite matrix at normal pH conditions. This is a measure of general corrosion, and its clear impact on coupons exposed to the ALDC filtrate suggests that these are losing substantial mass from the surface to corrosion in the form of freed ferrite cations. A detailed view of these cementite fins is given in Fig. 37.

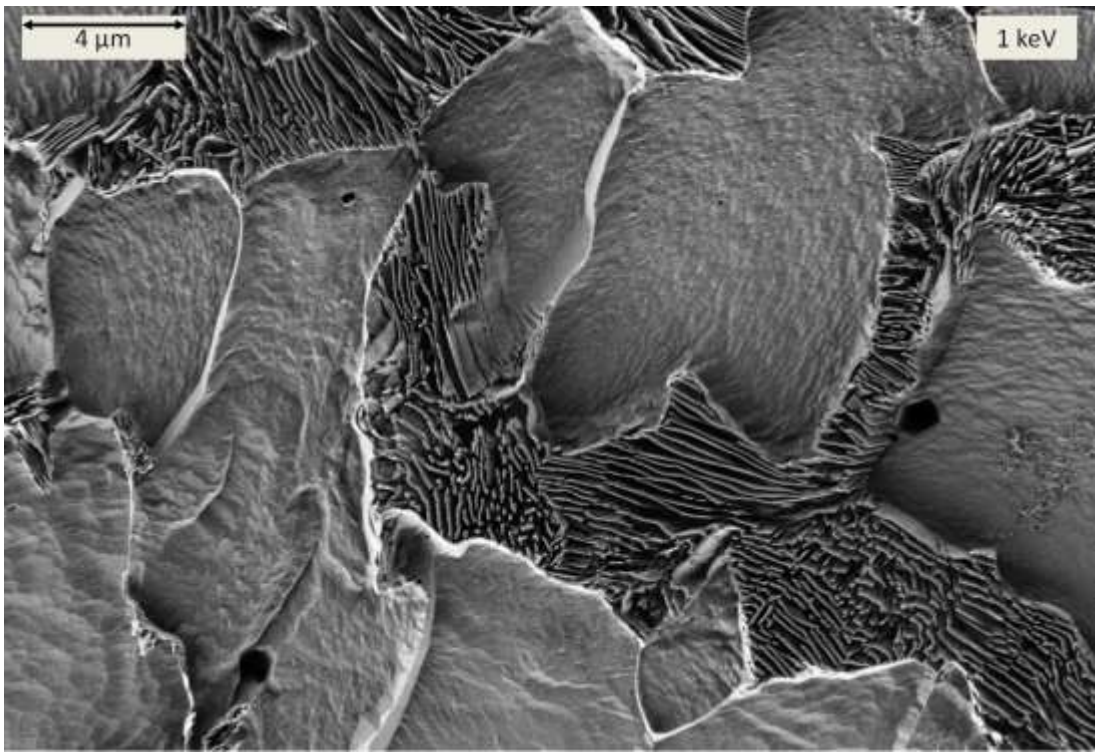

Figure 36: Differential corrosion within and among grains and between carbide fins in pearlite after corrosion by ALDC filtrate for two weeks and removal of corrosion deposits by treatment with Clark solution.

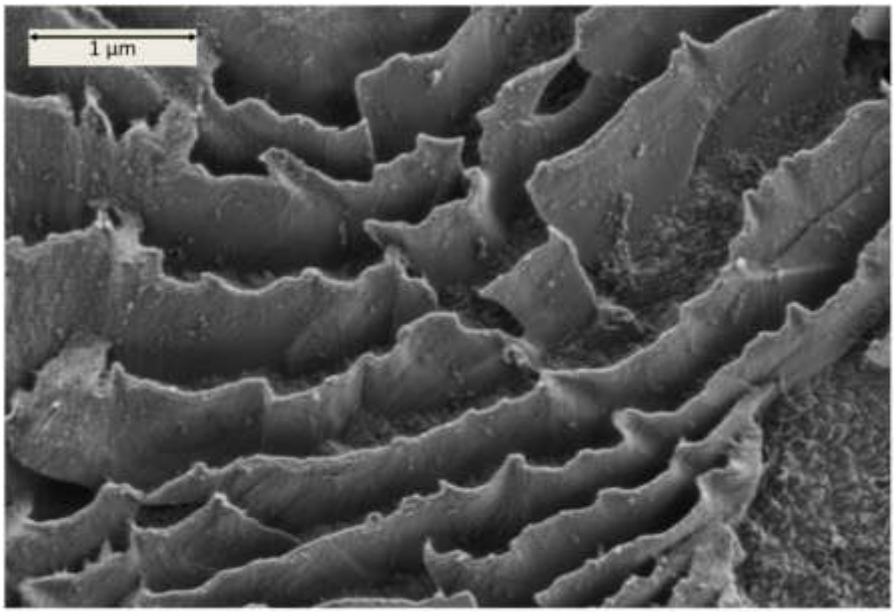

Figure 37: Detailed view of carbide fins starting to corrode in pearlite on a coupon corroded by ALDC filtrate for two weeks, after the removal of corrosion deposits by treatment with Clark solution.

Fig. 38 shows a coupon surface exposed for a long time (66 days) to a concentrated, 25 mM sodium sulfide solution in nanopure water and subsequently treated with Clark solution.

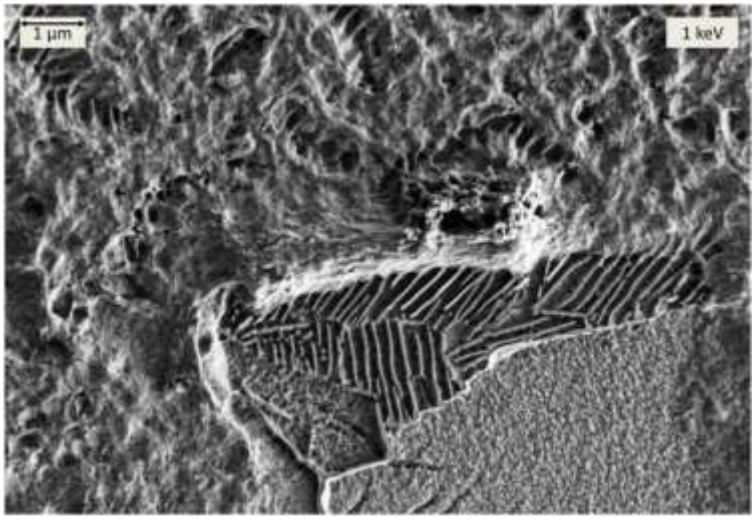

Figure 38: FeS corrosion deposit flaking off a coupon surface corroded by abiotic sulfide solution with [Na_2S] = 25 mM for a long time (66 days) reveals preferentially etched pearlite underneath.

The Clark solution did not completely remove the corrosion deposit, except in certain areas where it happened to flake off. An interesting note is that the corrosion deposit is clearly perforated and in line with the border of the pearlite structure. A comparison of the heights of the remaining carbide in pearlite corroded by abiotic and biotic solutions suggests accelerated corrosion in the presence of microbial life. Even for coupons exposed for a longer duration to an abiotic solution which had a sulfide concentration, the general corrosion was more severe on a coupon corroded biologically.

AFM scans of a region on the same biotically corroded coupon surface, shown in Fig. 39, confirm that these areas are different heights relative to a constant carbide height.

White arrows point out where the pearlite was and now only carbide is left. Heights relative to the carbide in the different domains are indicated in the section analysis. The color scale gives the depth.

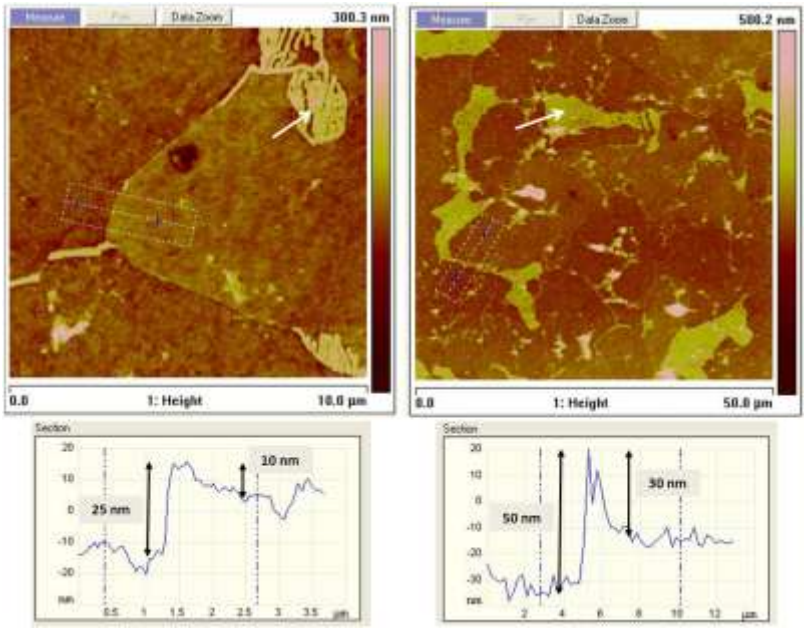

Figure 39: AFM scans of the same coupon surface corroded by ALDC filtrate for two weeks. Carbide serves as a measuring stick for corrosion.

Correlations Between Corrosion and Strain

These data strongly resemble the orientation and strain maps given by electron backscatter diffraction (EBSD). The EBSD crystal orientation map from Fig. 26 in Materials and Methods of a clean steel surface is superimposed on an FEM image of the corroded sample surface at the same scale for comparison between the differentially corroded areas and oriented domains. Note that these data are not from the same sample. The similarities suggest the hypothesis that there is a correlation between the residual strain and the corrosion rate.

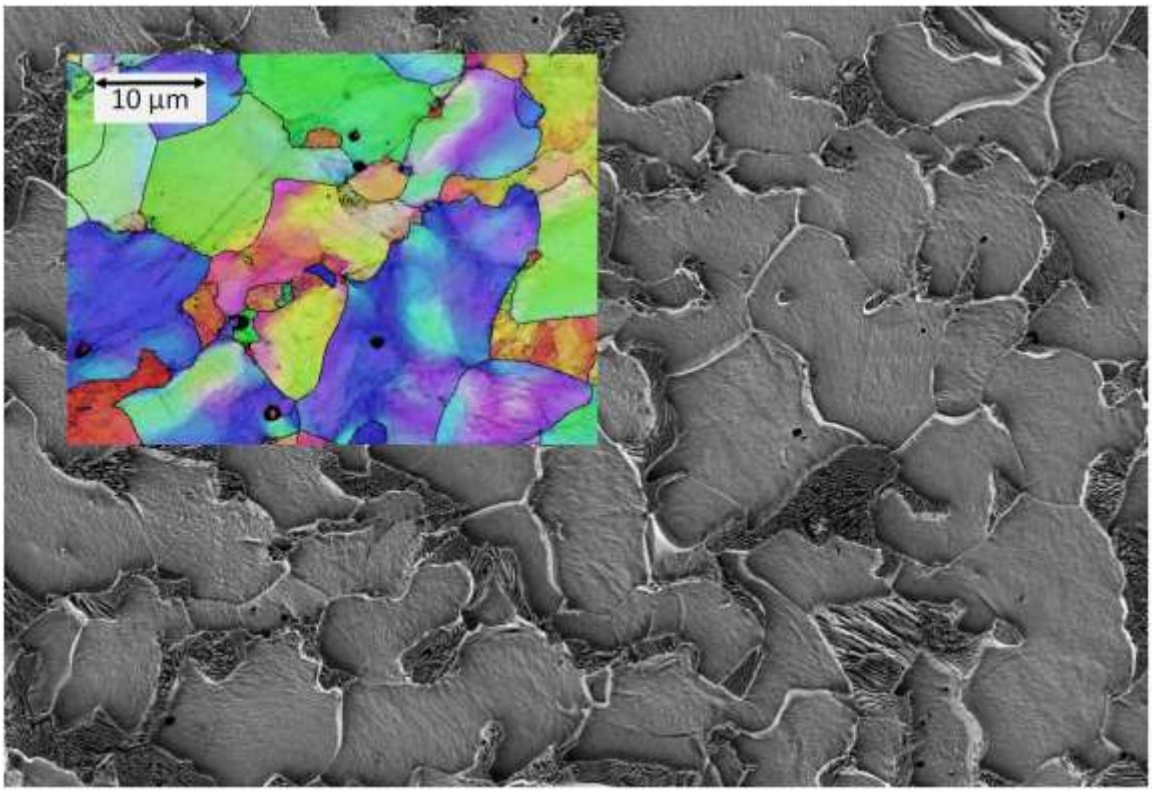

Figure 40: The same coupon surface as in Fig. 39 after corrosion by ALDC filtrate for two weeks and the removal of corrosion deposits at a lower magnification and with the orientation map of a (different) clean coupon surface at the same scale for comparison.

A similar result was observed in the differential sputtering of these domains after corrosion. This is illustrated by a sample exposed to the abiotic sulfide control (Fig. 41), but it was also observed on coupons exposed to all the other corrosive media and even on clean coupons which had not been corroded.

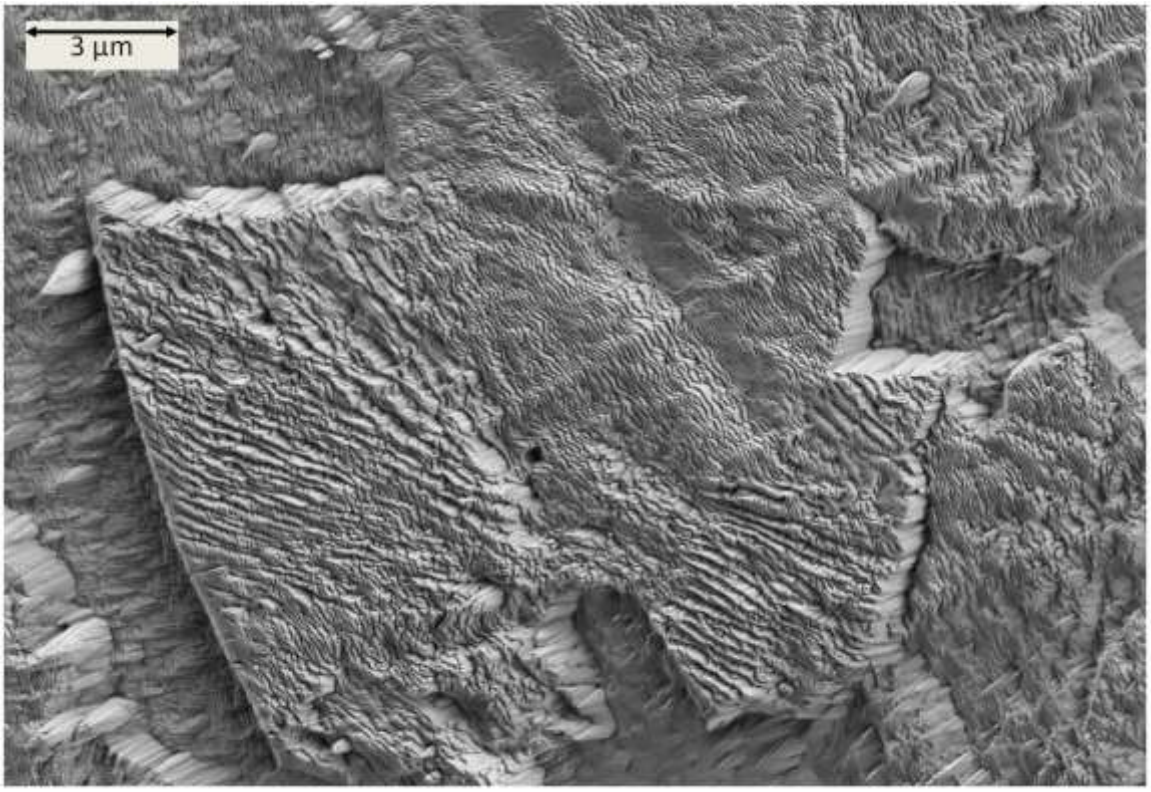

Figure 41: Coupon surface after corrosion by abiotic sulfide solution with [Na_2S] = 25 mM for two weeks and sputter etching to reveal the different grains.

A wider field of view of the same area on the corroded coupon is shown in Fig. 42, with an inset of the EBSD orientation map at the same scale for comparison. Note that these data are not from the same sample, but are given together to illustrate the guiding principle that corrosion originates in the residual strain present in the metal before corrosion even begins. Similar observations (not shown) were made regarding the differential sputtering of the uncorroded surface: it was hypothesized that the residual strain of local areas enters into the differential sputter rates of the surface. FEM images of sputtered clean surfaces reveal grains and grain boundaries because the residual strain along the grain boundaries exacerbates the etching of the surface.

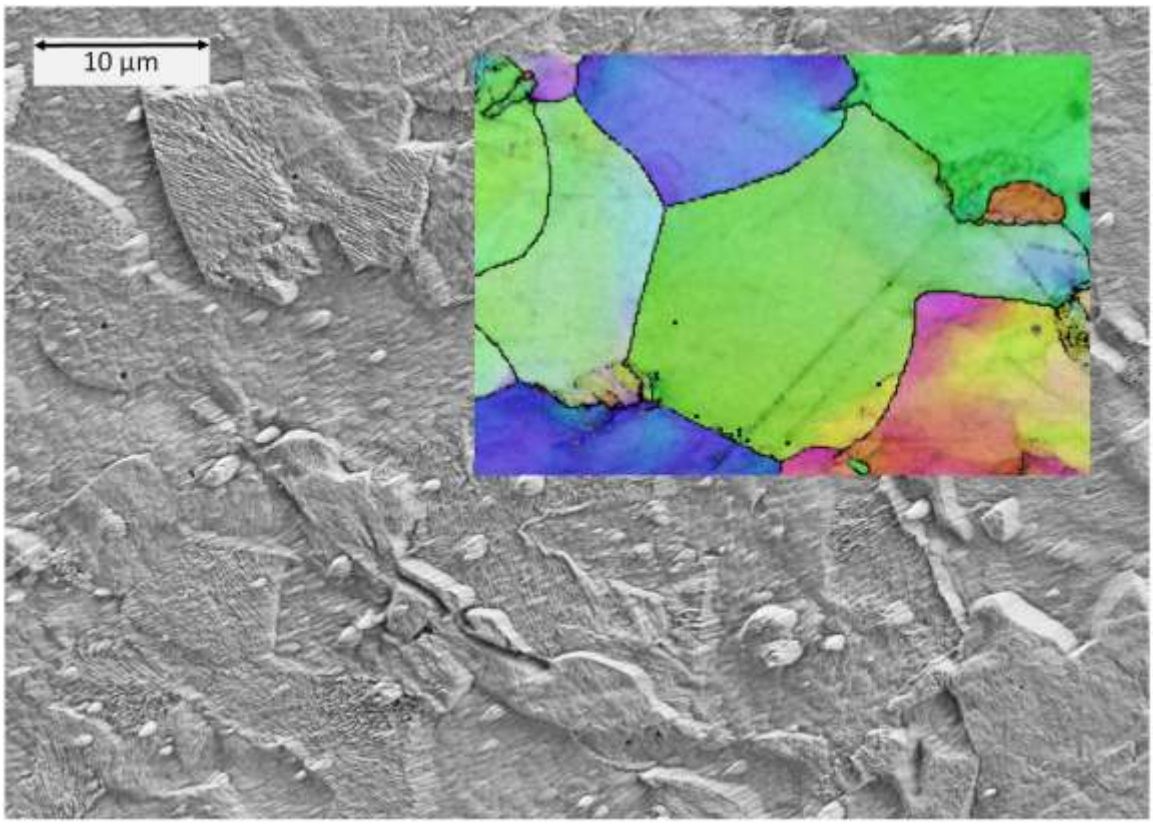

Figure 42: Same coupon surface as in Figure 41 after corrosion by abiotic sulfide solution, at a lower magnification, with the EBSD orientation map of a (different) surface on clean steel coupon inset at the same scale for comparison.

Summary

Comparison of the results between biotic solutions of ALDC and abiotic solutions, both with and without sulfide, show that the general corrosion is dominated by an iron sulfide corrosion mechanism, in which iron is lost from the steel coupon and combined with sulfide ions in solution to form a corrosion deposition layer of FeS. General corrosion is the least severe in the sterile SRB medium with a trace amount of sulfide (0.05 mM). The corrosion in the abiotic sulfide control and that in the ALDC biotic solution are morphologically similar, but the corrosion is more severe in biotic solutions, as indicated by mass loss and etching of ferrite. This suggests that the ALDC

cell culture produces metabolites which contribute to the cathodic processes besides H^+ and H_2S. The high corrosion rates in ALDC filtrates suggest that these metabolites are not filtered out at 0.2 µm and that it is not the cells themselves that are contributing to the accelerated corrosion.

Pitting

Mineral Inclusions Without Localized Corrosion

Corrosion pits were generated around MnS inclusions by exposure to either abiotic or biotic media. Other mineral inclusions, such as Si (shown in Fig. 43) and feldspar combined (shown in Fig. 44) did not progress to pits of localized corrosion in biotic or abiotic media, although their immediate surroundings show evidence of pit initiation. The Si inclusion in Fig. 43 was corroded by *D. indonensis* cell culture, and the feldspar inclusion in Fig. 44 was corroded by the abiotic sulfide control.

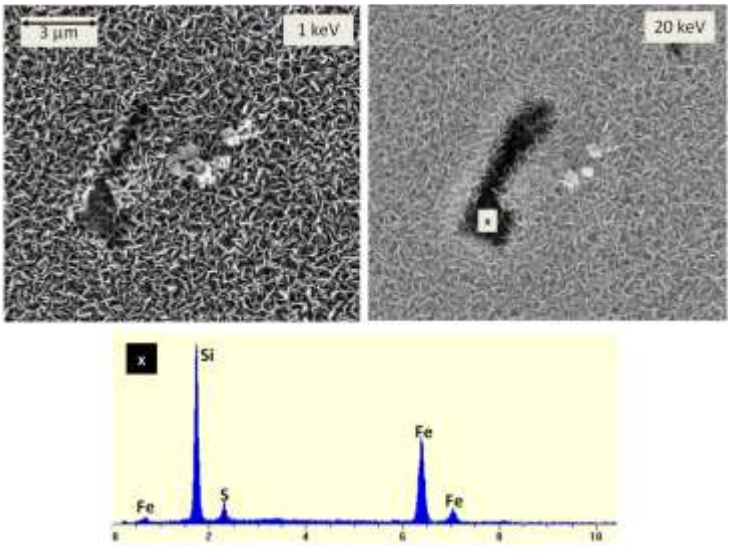

Figure 43: An inclusion of silica shows no pitting after exposure to abiotic sulfide solution with [Na_2S] = 25 mM for two weeks.

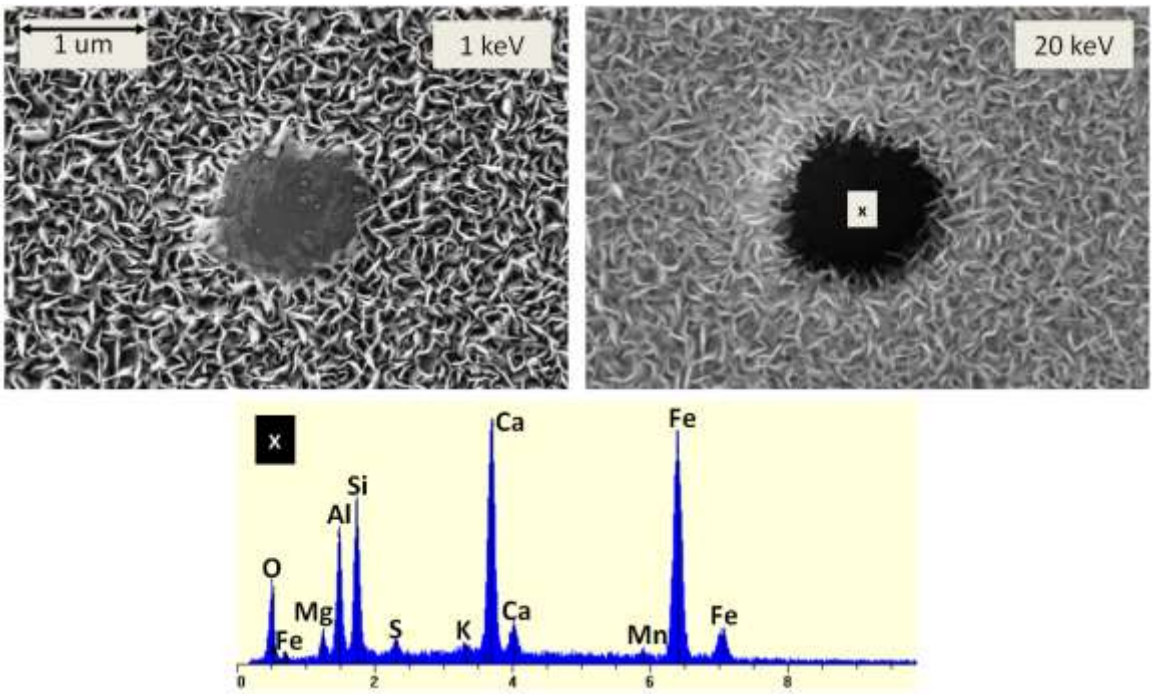

Figure 44: An inclusion of feldspar shows no pitting corrosion after exposure to abiotic sulfide solution with [Na_2S] = 25 mM for two weeks.

Active and Inactive MnS Inclusions

The MnS inclusions on the steel surface were numerous, and they did not all result in major pits. Inclusions that result in pits are deemed "active," whereas those that do not induce localized corrosion are "inactive." FEM images of groups of inclusions on a steel surface after exposure to *D. indonensis* cell culture are given in Fig. 45 and Fig. 46 The 1-keV images are given on the left, and the 20-keV images are on the right. The higher-energy, 20-keV electron beam used for taking EDX spectra is capable of penetrating the corrosion deposits to reach the steel surface underneath and image features such as the MnS inclusions under the biomass and inside the corrosion pits. The 1-keV beam is not energetic enough to do so. The surface in Fig. 45 was treated with Clark solution, whereas the one in Fig. 46 was not.

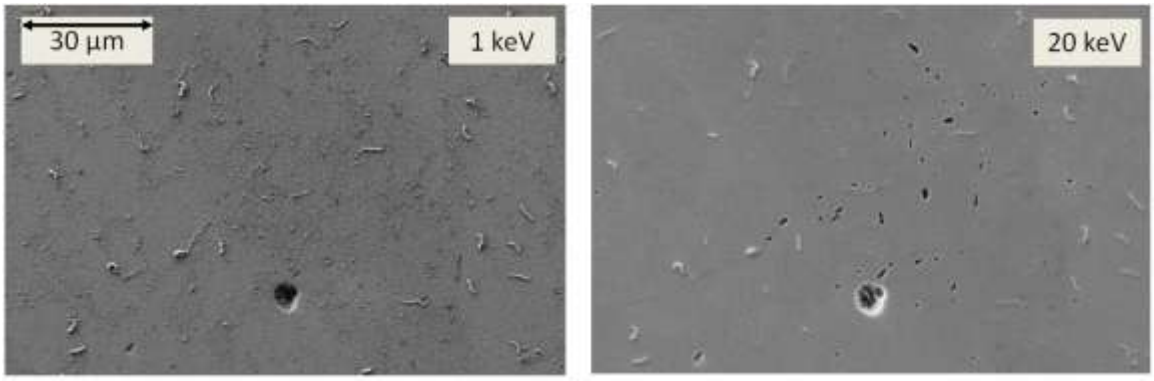

Figure 45: Single large pit among a group of inactive inclusions on a coupon surface corroded by *D. indonensis* cell culture for two weeks.

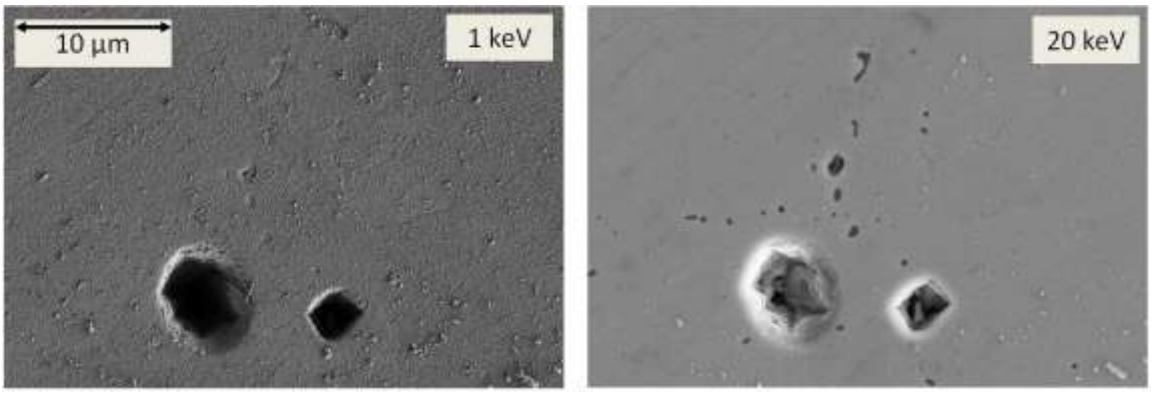

Figure 46: Large pits among a group of inactive inclusions on a coupon surface corroded by *D. indonensis* cell culture for two weeks.

Inclusions are seen at all stages of development. Detail of a totally inactive MnS inclusion on the surface illustrated in Fig. 46 is given in Fig. 47, and detail of an inclusion that has just been activated to localized corrosion is given in Fig. 48.

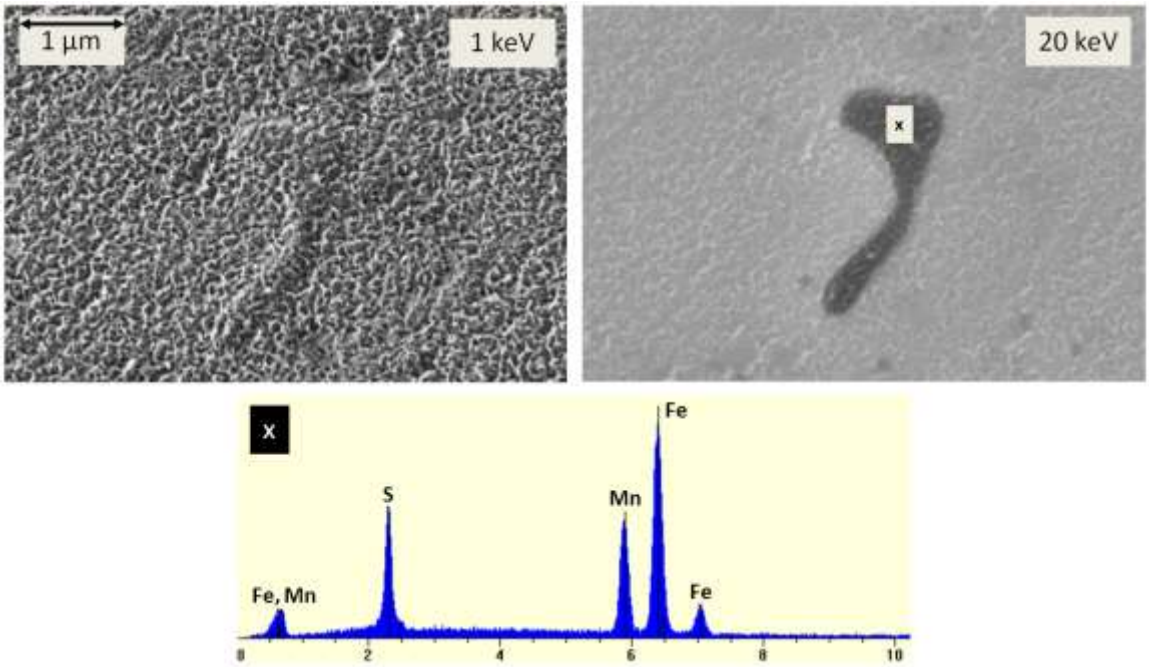

Figure 47: MnS inclusion on coupon surface shown in Fig. 46 that has not yet been activated to localized corrosion after exposure to *D. indonensis* cell culture for two weeks.

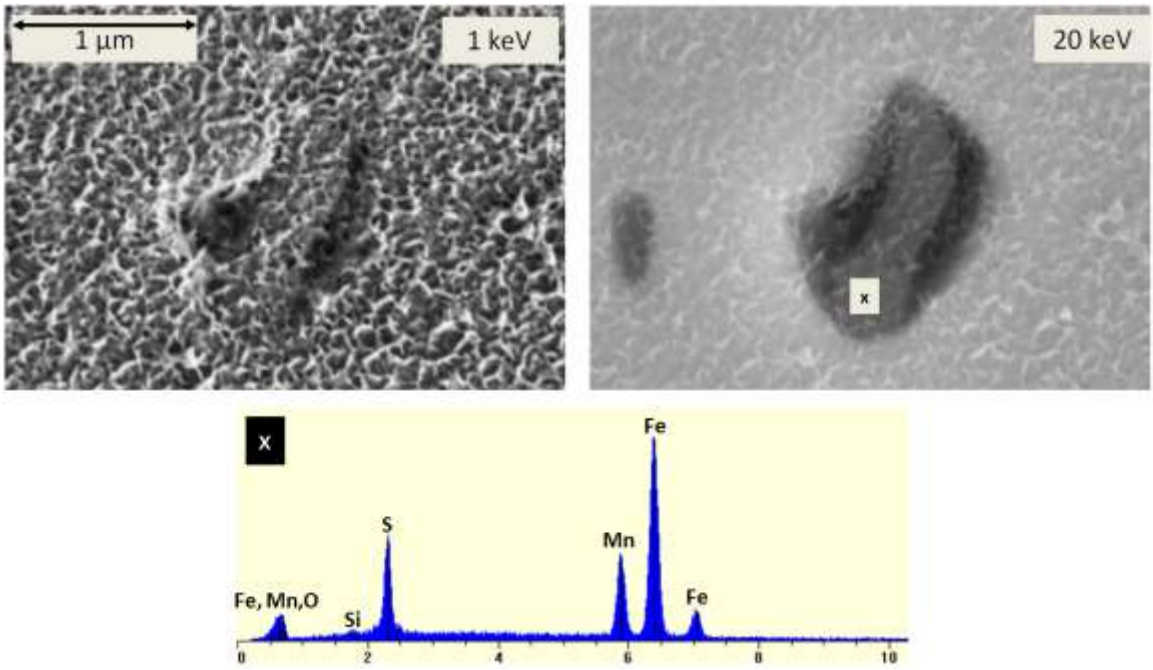

Figure 48: MnS inclusion with corrosion being initiated around a strained border with the Fe matrix on the coupon surface shown in Fig. 46 after exposure to *D. indonensis* cell culture for two weeks.

Pitting Initiation Around MnS Inclusions

The initiation of pitting around an inclusion takes place around the inclusion border, as shown in Fig. 49. This interface most likely had a slightly larger residual strain, and so is especially susceptible to initial attack. The surface elemental Auger nanoprobe maps of inclusion #1 in Fig. 10 in Materials and Methods showed an oxygen ring around the inclusion where this pitting was being initiated in the inclusion in Fig. 48. Inclusions containing Ca (Figs 20, 21, 24, and 25) had pitting initiate around their edges for the same reasons.

Surface elemental maps of an MnS inclusion corroded by sterile ALDC medium, taken with the nanoprobe Auger, are given in Fig. 49. These show the surface composition shortly after pitting has been initiated around the inclusion edge. The surface has been cleaned by the sputtering off of 10 nm.

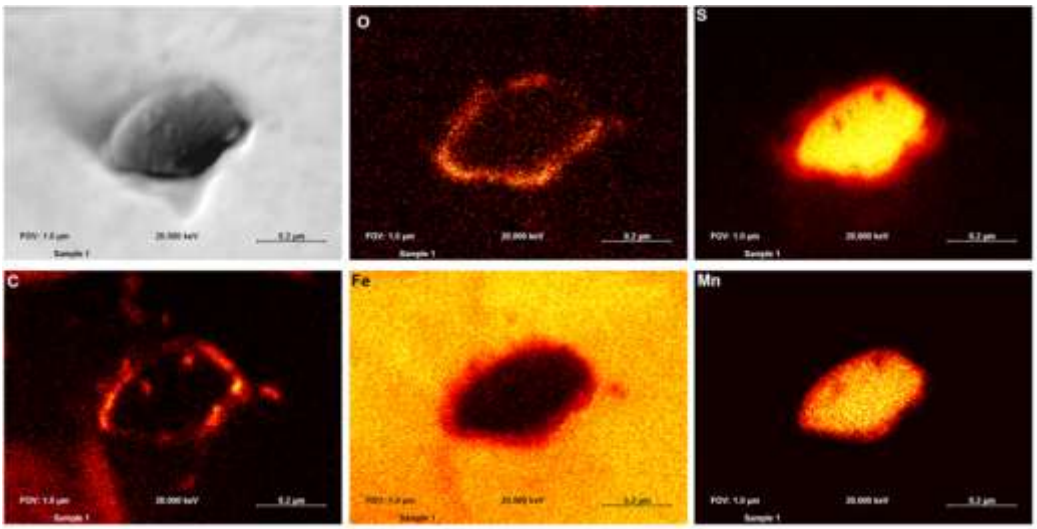

Figure 49: Surface elemental maps taken with Auger nanoprobe of MnS inclusion after corrosion by sterile ALDC medium with [Na_2S] = 0.05 mM for 11 days and 10 nm sputter cleaning. The FEM image at 20 keV is shown in the upper left corner. The elements mapped are (from second image, top row, left to right) oxygen, sulfur, (bottom row, left to right) carbon, iron, and manganese.

The carbon map shows that the inclusion has been effectively cleaned of C deposition on the surface, except around the inclusion edge. The sulfur map is dispersed around the inclusion, indicating that the MnS is mixed with the surrounding Fe matrix from the metallurgical processing. The Mn Auger signal, mixed with the Fe Auger signal, shows a sharp edge, which is an artifact of the signal processing.

The oxygen map shows an oxide ring around the inclusion where the initiation of corrosion is taking place. The strict anoxic conditions imply that this is not due to oxidation of the steel surface by dissolved O_2. Instead, this is a deposition around the inclusion edge of iron(II) hydroxide from hydrolyzed iron cations freed from the strained inclusion edge, as given in the reaction in equation 15.

(15) $Fe^{2+} + 2\ H_2O \rightarrow Fe(OH)_2 + 2\ H^+$

The production of protons in the above reaction creates acidic conditions around the inclusion. It was demonstrated clearly in Materials and Methods that these inclusions do not have a consistent elemental composition, but rather possess variable amounts of Cu_2S, Ca, Ti, and other elements. This may explain why some of these corrode actively while others do not at normal pH conditions. MnS inclusions actively seen in all stages of pit development imply that more inclusions become active with time. The rate at which these inclusions become active and the subsequent accumulation of pits on a steel surface are major corrosion parameters.

MnS Inclusion and Pit Distributions

The severity of corrosion in these systems is in part described by the density of pits that accumulate on the steel surface under exposure to SRB and other sulfidogenic

environments. By and large, inclusions were the most numerous on samples that were biologically corroded. This is a qualitative assessment based on hours spent investigating these surfaces under high magnification in the FEM. FEM images of a coupon surface after exposure to *D. indonensis* cell culture and treatment with Clark solution are given in Fig. 50.

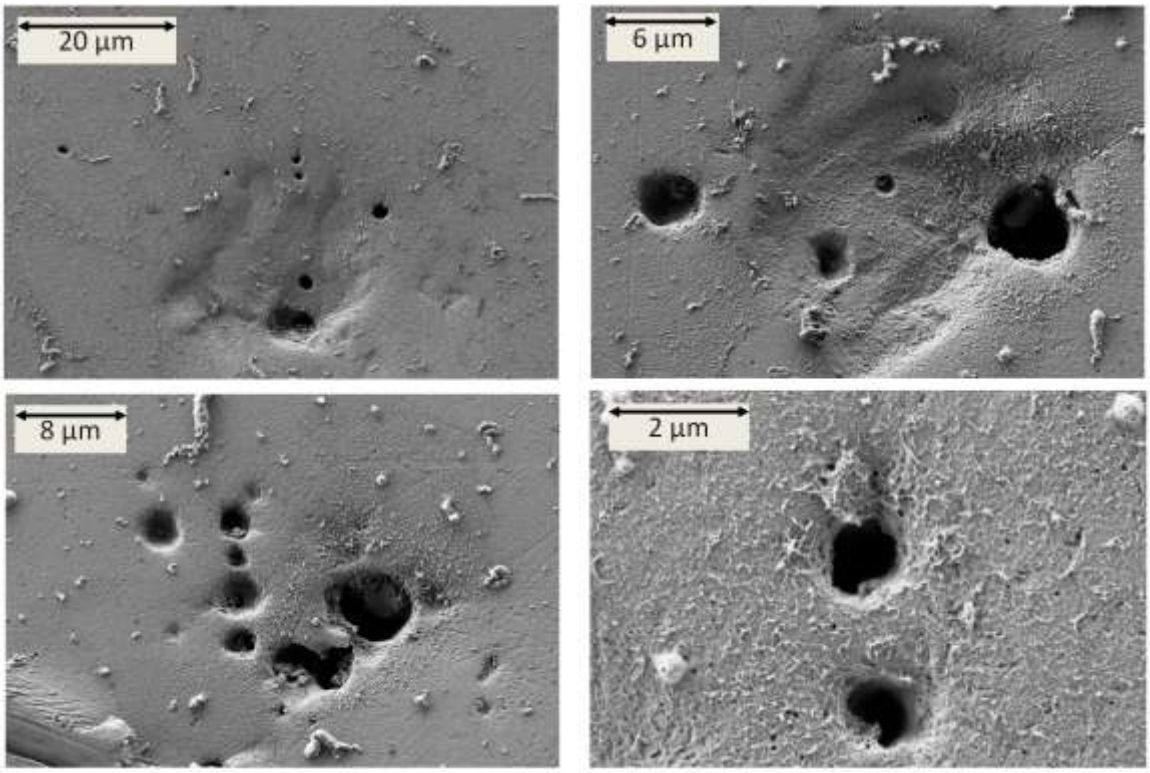

Figure 50: Groups of pits on coupon surfaces corroded with *D. indonensis* cell culture for two weeks and subsequently treated with Clark solution to remove corrosion deposits and biofilm.

The pit groups in the top two images are in a shallow depression. This may be a region of large residual strain on the immediate surroundings of MnS inclusions accelerating pitting corrosion.

Pairs of pits were also seen on coupons exposed to sterile ALDC medium and ALDC cell culture, as shown in Fig. 51 and Fig. 52, respectively. However, no regions were ever found with groups of pits as dense as those on coupons exposed to *D. indonensis*.

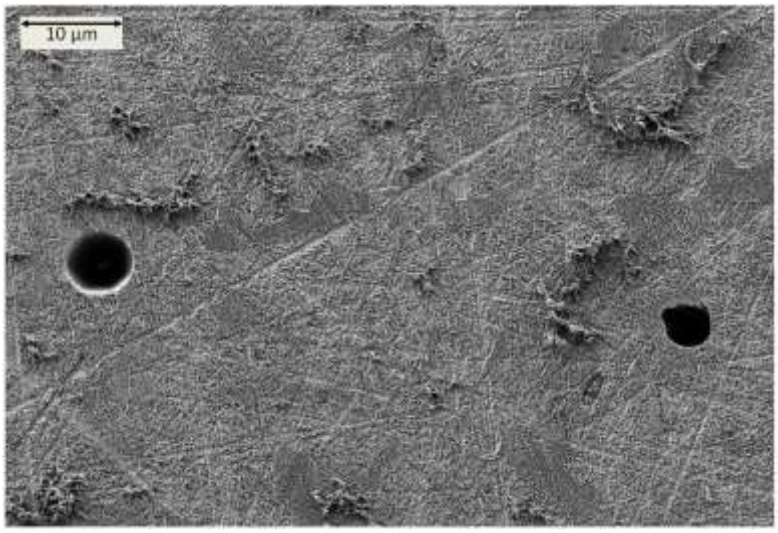

Figure 51: Pair of pits on coupon surface corroded by sterile ALDC medium with [Na_2S] = 0.05 mM for two weeks.

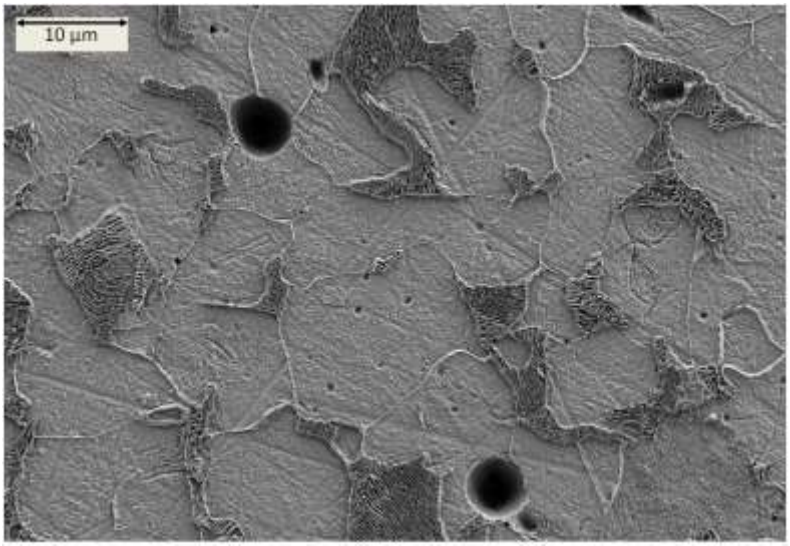

Figure 52: A similar pair of pits on coupon surface corroded by ALDC filtrate for two weeks after treatment with Clark solution.

Observing groups of pits in *D. indonensis* cell culture indicates that the area was more acidic than similar areas in ALDC cell culture, hence activating` otherwise passive MnS inclusions and causing the formation of excess pits in the low-pH areas.

Identifying the distribution of initial pits at normal pH and its relation to the distribution of MnS inclusions is one of the objectives of this proposal. For example, a high concentration of pits in a small area could form a large macro-pit of the type that leads to material failure. MnS inclusions were seen both distributed in tight groups, and totally solitary and at intermediate densities.

Two coupons, one corroded by sterile ALDC medium and another by ALDC cell culture, were used for finding the pit distribution statistics. A typical polished, clean steel coupon was used to find the inclusion distribution statistics. All coupons were treated with Clark solution to remove any corrosion deposits/biofilm from corroded samples. The Clark solution dissolved the MnS inclusions but not other inclusions, such as silica or feldspar, on the clean coupon surface, leaving them as distinctive high-contrast pits.

To find the distribution of MnS inclusions, FEM images were taken with a 20-keV primary beam energy at 512 different fields of view arranged on a grid on the sample. Each field of view (FOV) measured 75×52 μm^2 (3900 μm^2) in size. This gives a total investigated area of 2.0 mm^2. The size of the field of view was chosen so that the inclusions would be visible as small but clear spots to the naked eye. The FEM images were taken in high contrast in order to accentuate the dark pits against the background.

The grid coordinate system measured 8.5×8.5 mm^2, divided into 16×32 FOVs centered on the 1.27-cm-diameter coupon surface. Each FOV center was on a cross hair

and separated from the neighboring FOVs by 531 µm in the x-direction and 266 µm in the y-direction, so that no two FOVs would overlap. Figure 53 is a representation of the coordinate system on a sample surface.

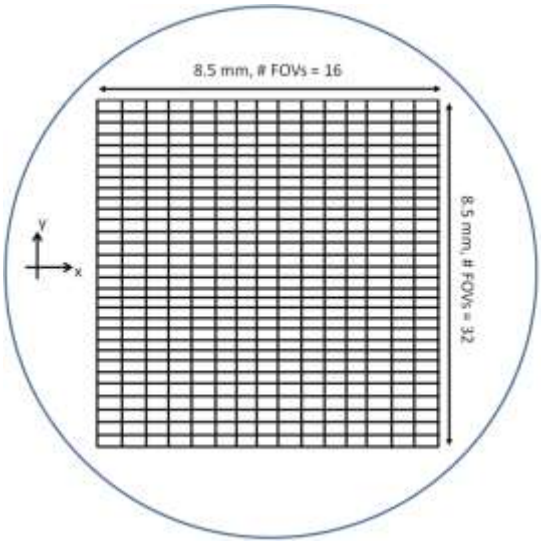

Figure 53: Illustration of grid on a clean coupon surface for keeping track of fields of view in which MnS inclusions were counted to find their distribution on the coupon surface.

The number of pits left by MnS inclusions on the clean coupon surface was counted per FOV by loading the 512 FEM images into a MATLAB program (Appendix). The program converted the original grey-scale images to binary images. The program transforms each of the pixels in an image with a luminescence greater than the assigned threshold to a white pixel and makes all other pixels black. An example of one of the FEM images and the corresponding binary image are given in Fig. 54 and Fig. 55, respectively. The identified inclusions are marked by white boxes.

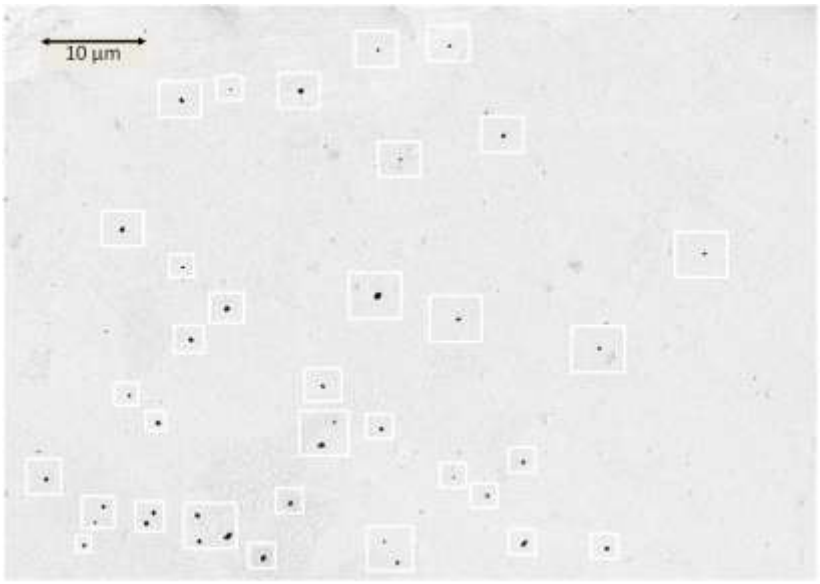

Figure 54: Typical field of view taken from a sample surface on which to count inclusions. The pits left from the inclusions after treatment with Clark solution show up as black dots on a white background in images taken in high contrast.

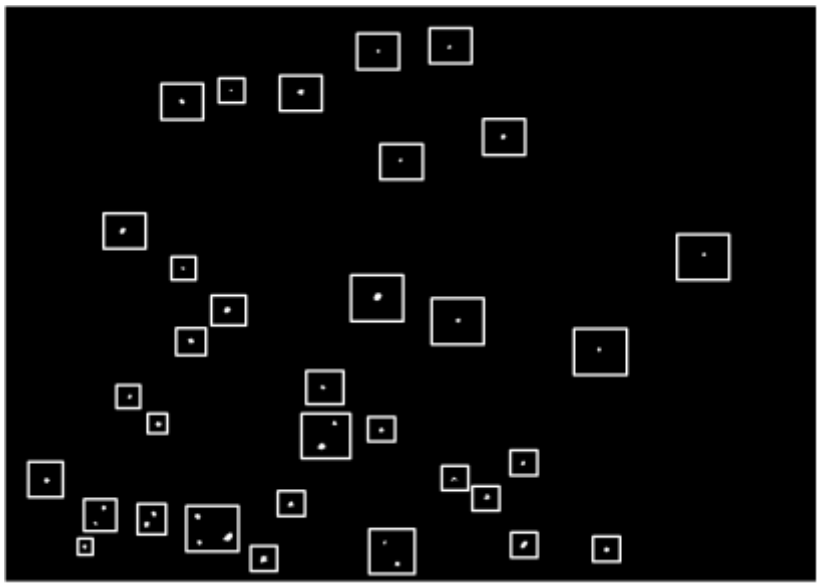

Figure 55: Same field of view after image processing has reduced it to a binary image, that is, white groups of pixels representing MnS inclusions and a black background. The number of groups of white pixels is counted to give the number of MnS inclusions in the field of view.

Groups of white pixels in the binary image were taken to be pits where there were once inclusions. These were counted in each image using the "bwconncomp" command in MATLAB. The number of MnS inclusions counted in Figs. 54 and 55 by the program was double-checked and found to be consistent at 39. The number, n, of inclusions in a FOV was plotted against the number, N (n), of FOVs in which n inclusions were counted. A histogram is built using 10 bins. The resultant distribution of MnS inclusions on the coupon surface is shown in Fig 56.

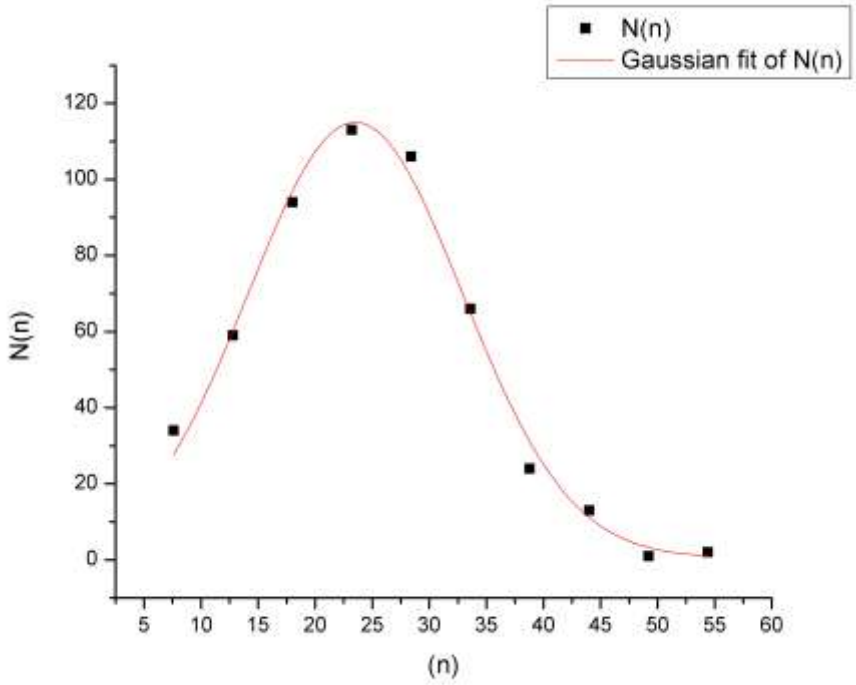

Figure 56: Distribution of MnS inclusions on clean coupon surface built from large (75 × 52 μm^2) fields of view. Distribution varies about the mean.

The distribution was fitted to a normal Gaussian, given in equation 16.

(16) $$N\,(n) = N_0 + \left[\frac{A}{w\sqrt{\frac{\pi}{2}}}\right] e^{-\frac{2(n-n_C)^2}{w^2}}$$

Gaussian fits herein will be fitted to this equation. The curve fitting parameters are given in Table 6.

Table 6: Curve fitting parameters to normal Gaussian for distribution of MnS inclusions on coupon surface over 512 fields of view. The parameters are unitless.

	Value	**Standard Error**
N_0	0.56	3.66
n_c	23.52	0.32
W	18.79	0.98
A	2695.53	190.05
Standard Deviation	9.39	-
FWHM	22.12	-
Height	114.48	-

The distribution averages 24 MnS inclusions per 3900 μm^2 field of view, or one inclusion per 163 μm^2.

The choice of FOV size determines the resolution of the distribution of the MnS inclusions. A FOV that is too large gives a distribution in nearly constant fluctuation about the mean, a very narrow Gaussian. The width of the Gaussian can be broadened by the choice of a FOV with small dimensions that are comparable to or less than the average spacing between inclusions, so that many FOVs are empty of inclusions. The distribution of the average spacing between inclusions in a field of view, *d*, was calculated using the RegionProps command in MATLAB (‘centroid’) and is given in Fig. 57. The distribution was fitted to a normal Gaussian with the fitting parameters given in Table 7.

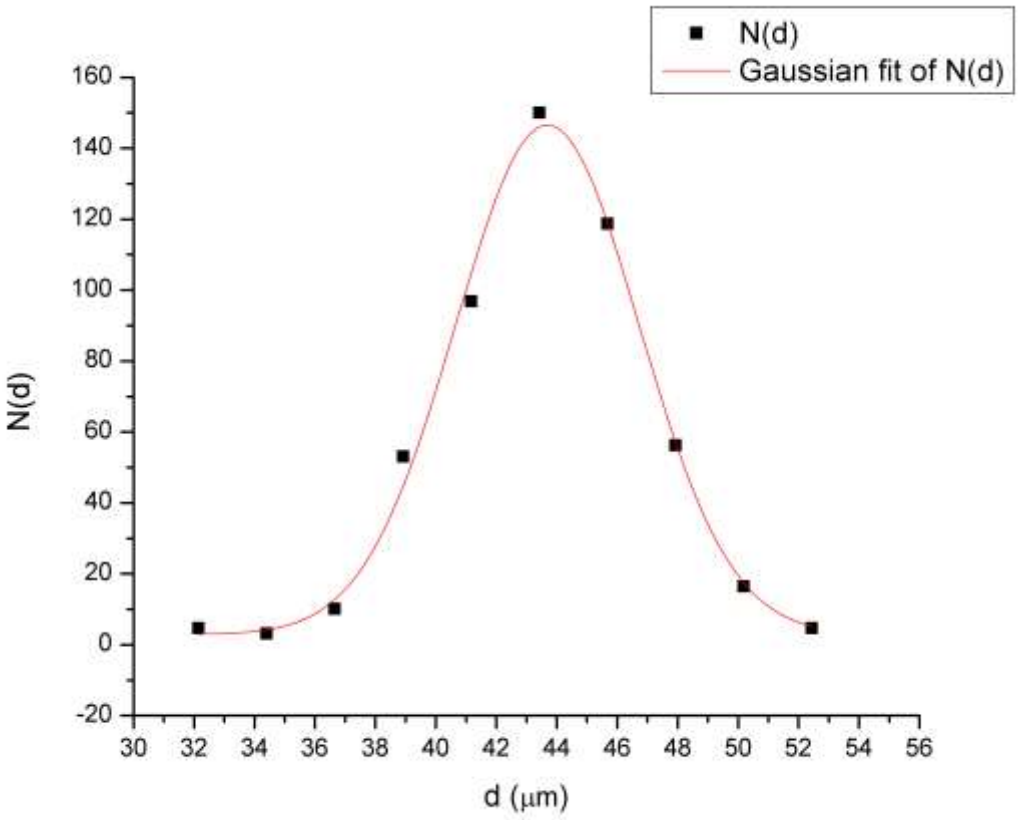

Figure 57: Distribution of average distance between MnS inclusions in 512 fields of view.

Table 7: Curve fitting parameters of normal Gaussian for distribution of average distance between MnS inclusions among 512 fields of view. The unit is μm, except where the parameter is unitless (N_0 and Height).

	Value	**Standard Error**
N_0	2.87	3.05
d_c	43.69	0.10
W	6.07	0.27
A	1094.65	58.28
Standard Deviation	3.04	-
FWHM	7.15	-
Height	143.78	-

The average distance between inclusions is ~44 μm with a full width at half maximum (FWHM) of 7 μm. The dimensions of the FOV are greater than this average

distance, and so the distribution given by these FOVs fluctuates normally about the mean, as expected. The necessary resolution was achieved by subdividing each 75 × 52 μm^2 field of view into twelve 15 × 15 μm^2 subfields of view as illustrated in Fig. 58.

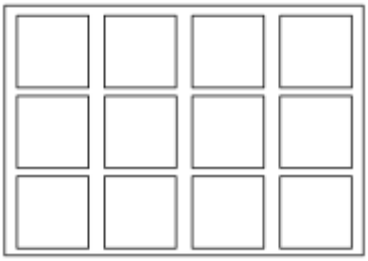

Figure 58: Illustration of subdivision of 512 large fields of view in to 6144 smaller (15 × 15 μm^2) fields of view.

This produced 6144 sub-FOVs measuring 15 × 15 μm^2 (225 μm^2) each, corresponding to a total analyzed area of 1.4 mm^2. The distribution of MnS inclusions throughout these FOVs is given in Fig. 59.

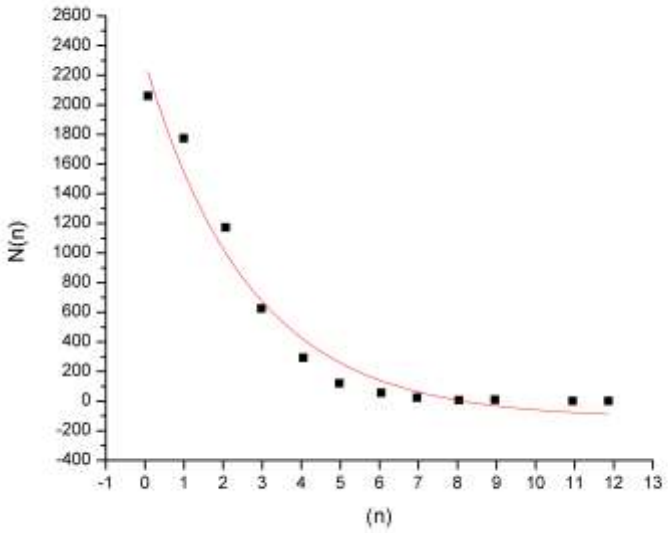

Figure 59: Distribution of MnS inclusions among 6144 small (15 x 15 μm^2) fields of view.

This distribution follows an exponential decay, and it is more instructive to image this in a semi-log graph, where the distribution is linear. Fig. 60 gives the data in the previous figure as the natural log of *N (n)* vs. *n*. The linear fitting parameters are given in Table 8.

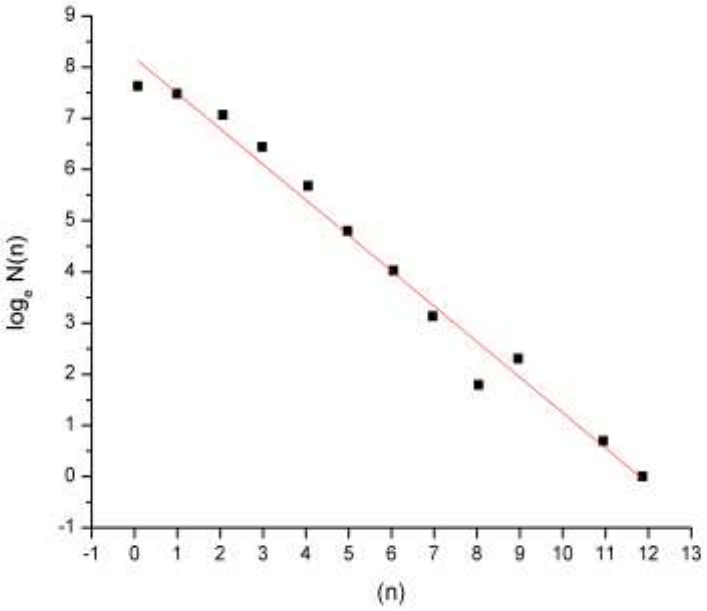

Figure 60: Semi-log plot of distribution of MnS inclusions on clean coupon surface among 6144 fields of view.

Table 8: Linear curve fitting parameters for semi-log plot of distribution of MnS inclusions on coupon surface among 6144 fields of view. The parameters are unitless.

	Value	**Standard Error**
Intercept	8.18	0.20
Slope	-0.69	0.03

This produces a good linear correlation between the natural log of N (n) and n. The slope of the fitted line gives the decay constant of the distribution in Fig. 59. The decay constant is the number of inclusions, (n), per FOV for which the number of FOVs, N (n), decreases by a factor of e. We determined whether the MnS distribution shown in Fig. 59 agreed with the pit distribution in the corroded samples by comparing the decay constants of the distributions.

To find the distribution of corrosion pits on the samples exposed to ALDC cell culture and sterile ALDC medium, larger-size FOVs were chosen, because we knew that the average distance between these pits is quite large (hundreds to thousands of microns). A total of 144 FOVs measuring 750 × 480 μm^2 (0.36 mm^2) were analyzed, corresponding to a total area of 51.5 mm^2, on coupons exposed to the ALDC cell culture. The magnification (500 x) was the limit at which the pits could be detected and counted with the naked eye, so no image processing was required. Analysis was conducted over a grid arranged as 9 x 16 FOVs. Pits on the surfaces of coupons exposed to the sterile ALDC medium were counted over 10 fields of view, measuring 375 × 240 μm^2, for a total analyzed area of 9 mm^2. The corrosion pits were large (> 2 μm) and morphologically distinct. Also, there was never more than a few pits in a given FOV, so they were easily counted by the human eye.

The distributions of abiotically and biotically induced corrosion pits are described and fitted in Fig. 61 analogously to the MnS inclusion distribution with 6144 FOVs given in Fig. 59. The distributions give similarly correlated results. The fitting parameters are given in Table 9.

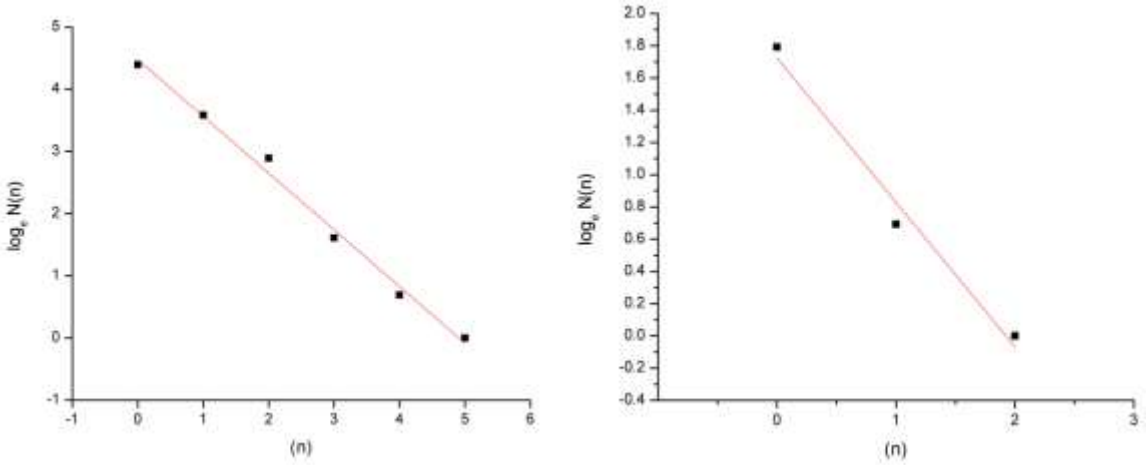

Figure 61: Semi-log plots of the distribution of pits on coupon surfaces corroded by (left) ALDC cell medium for two weeks among 144 fields of view and (right) sterile ALDC medium with [Na_2S] = 0.05 mM for two weeks among 10 fields of view.

Table 9: Linear curve fitting parameters of semi-log plots of distributions of pits on coupons corroded by ALDC cell culture and sterile ALDC medium. The parameters are unitless.

		Value	**Standard Error**
ALDC cell culture	Intercept	4.48	0.12
	Slope	-0.91	0.04
Sterile ALDC medium	Intercept	1.72	0.15
	Slope	-0.90	0.11

Other parameters relevant to corrosion are given in Table 10. The decay constants are in close agreement (~ 1 or 1.5), indicating a correlation between the pit distributions on corroded coupons and the distribution of MnS inclusions on a clean coupon.

Table 10: Summary of inclusion and pit density distributions for a clean coupon and coupons corroded by ALDC cell culture and sterile ALDC medium. The parameters are unitless.

	Density (μm^2 per pit or inclusion)	Density (inclusions per pit)	Decay constant	Total area analyzed (mm^2)	# of FOVs
Clean coupon	161	-	1.45	1.4	6144
ALDC cell culture	5.18×10^5	3180	1.10	51.8	144
Sterile ALDC cell medium	1.80×10^6	11043	1.11	9.0	10

Morphology and Elemental Composition of Corrosion Pits

Introduction

Corrosion pits were identified using high-resolution imaging in the FEM and elemental analysis using EDX of the coupon surface. Pits generated around MnS inclusions in a zone ranging from 20-100 nm in width surrounding the inclusion border. In advanced stages of pitting, this left the inclusion as an island within the void of the pit. In very advanced stages of pitting, the inclusion was no longer morphologically distinct in the pit.

FEM images acquired with both a 1- and a 20-keV energy primary electron beam of an MnS inclusion corroded by sterile ALDC medium, and the accompanying EDX from relevant spots, are given in Fig. 62.

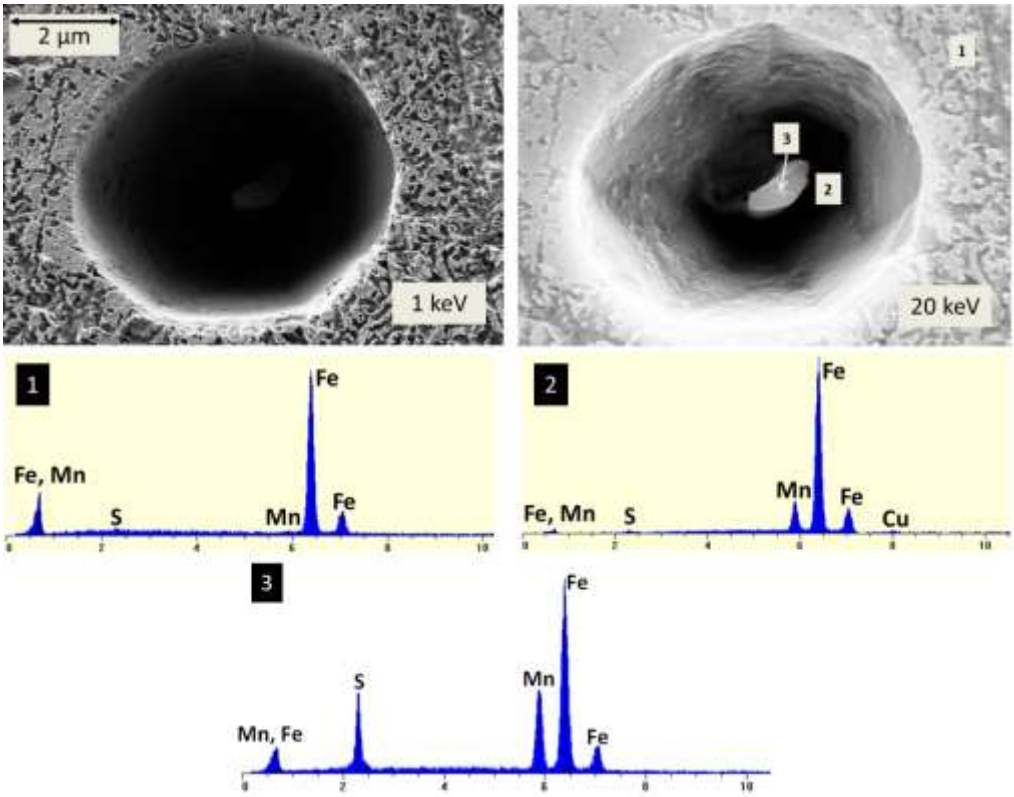

Figure 62: Pit around MnS inclusion after corrosion by sterile ALDC cell medium with $[Na_2S]$ = 0.05 mM for two weeks. The EDX spectra were taken from the background (1), the pit (2), and the MnS inclusion (3).

An inclusion is barely visible within the pit, as seen in the FEM image taken with the 1-keV energy electron beam. At high contrast and at a higher beam energy, more highly energetic secondary electrons reveal the inclusion clearly within the pit. It is morphologically similar in size and shape to the MnS inclusions investigated on the clean steel coupons. Therefore, FEM images of pits acquired with both 1- and 20-keV primary beams are shown in this thesis. The two measurements complement each other. The low-energy primary electron beam can image at a higher resolution. However, the higher-energy primary beam penetrates deeper into the specimen surface, yielding information hidden from the 1-keV primary beam.

The pit grew deeper and propagated radially from the inclusion. It can be seen that the inclusion penetrates into the pit and that the pit progresses much deeper than the surface of the inclusion. The inclusion microwires dive hundreds of microns into the steel surface, propagating accelerated localized corrosion in the immediate iron matrix to some depth.

Present in the accompanying EDX spectrum of the inclusion are manganese, sulfur, and iron, confirming the inclusion as MnS. Also present is copper deep within the pit, this time in a concentration sufficient to be measured by EDX, albeit in a small, ~1%, atomic concentration. The reliability of the quantitative analysis taken from EDX is questionable, however, in these scenarios because of the strong attenuation of the characteristic X–rays leaving the copper atoms at the bottom of the pit. The sulfur characteristic X–ray peak has the necessary intensity to be resolved in the spectrum taken from the inclusion, but not in the spectrum collected from deep within the pit. This is because these low-energy S K-α X–rays barely make it to the surface through the Fe matrix. The pit around the inclusion, however, descends deeper; thus, low-energy X–rays collected from within the pit are attenuated even more by the inelastic scattering events they experience transmitting through the steel matrix of the pit walls. The passage through the pit walls is necessary because of the geometry of the system, in which the X–ray detector is held fixed at a 55° angle to the coupon surface normal.

Low-Energy X–ray Attenuation in EDX Spectra

The path length of the X–ray between the surfaces of the inclusion and surrounding pit matrix is the sum of a distance (*D*) in the vacuum of the pit and a distance

(*d*) through the steel of the matrix. Fig. 63 illustrates the geometry in the plane of the pit profile. The pit depth and radius (*r*) approximating the pit walls as being at a steep, 90° angle to the surface normal are indicated.

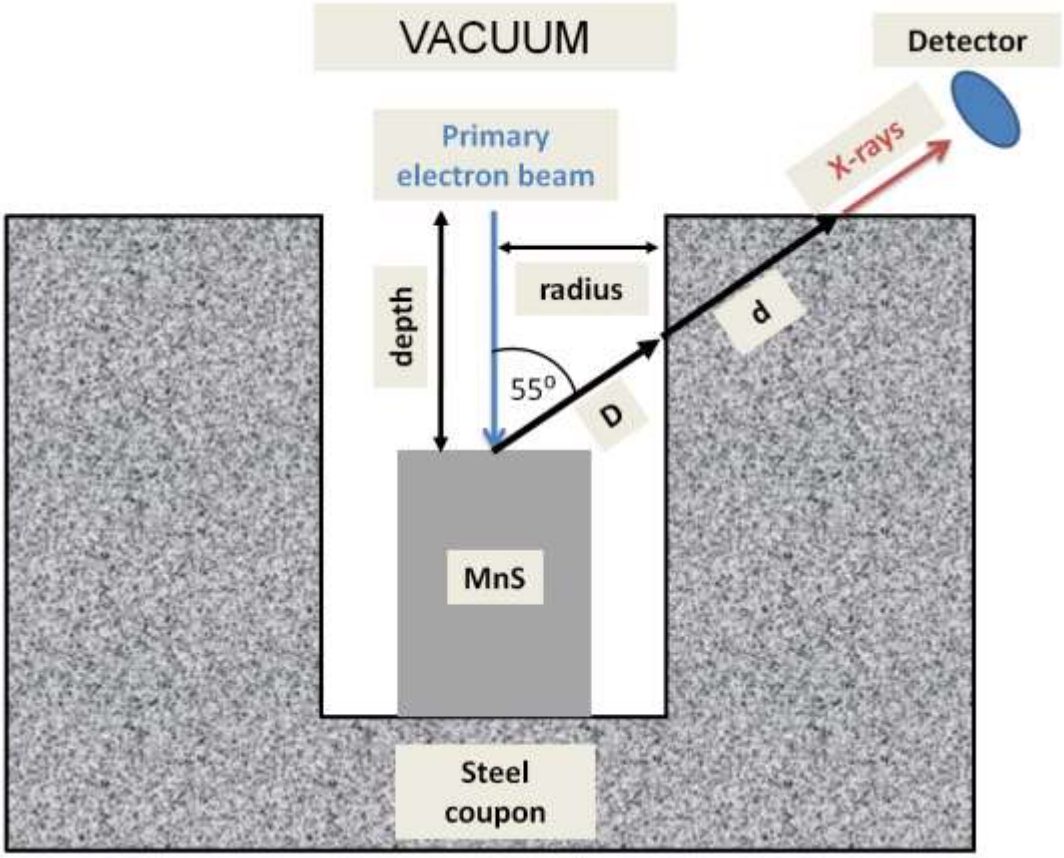

Figure 63: Geometry of pit as seen from a profile cross section. Also shown is the relative position between the sample orientation and the X-ray detector. *D* is the distance the X- rays travel through the vacuum of the pit, and *d* is the distance travelled through the iron of the pit walls. The radius of the pit is *r*.

The depth is the product of the total path length and the trigonometric factor cosine (55^0). Because of the ambiguity in the geometry of the pit, *D* is estimated as an upper bound by assuming that the pit walls are at a steep ninety degrees to the sample surface. This is the pit radius, along the line towards the detector, divided by

trigonometric factor sine (55^0). Conversely, the lower bound would be $D = 0$, where the pit walls are adjacent to the inclusion and slanted at an angle less than fifty-five degrees from the vertical.

The transmitted intensity (I) is a function of path length through the material (d) and X–ray frequency ω:

(17) $$I(\omega, d) = I_0 e^{-\mu(\omega)\rho d}$$

Where I_0 is the incident intensity, μ is the mass attenuation coefficient, and ρ is the density.

Mass attenuation coefficient μ (ω) is a tabulated parameter for a given material that determines the attenuation as a function of energy, (ħ ω). The material density of steel is ρ ~ 7.8 gm/cm^3.

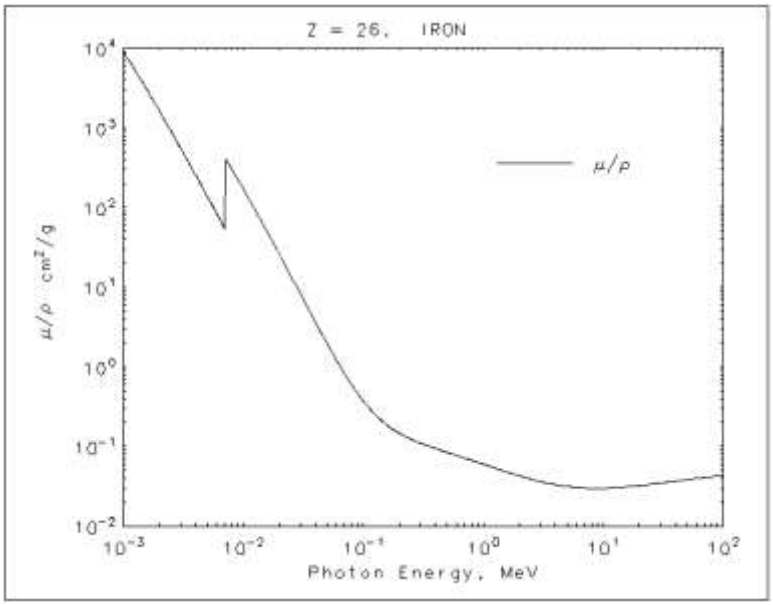

Figure 64: Tabulated mass attenuation coefficient as provided by NIST: http://physics.nist.gov/PhysRefData/XrayMassCoef/ElemTab/z26.html

The ratio of the transmitted and incident intensities is given in terms of the mass attenuation coefficient by equation 18.

(18) $I/I_0 = e^{-\mu(\omega)\rho d}$

The frequency is related to the energy of the X–ray by the quantum mechanical relationship $E = \hbar \omega$. The skin depth (ε) is the depth at which the radiation has been lost by a factor of *e*: $\varepsilon = (\mu\rho)^{-1}$. The skin depths and mass attenuation coefficients at the tabulated energies are given in Table 11 (**NIST**).

Table 11: Summary of mass attenuation coefficient (μ/ρ) and corresponding skin depth (ε) as a function of X–ray energy.

Energy (keV)	**μ/ρ (cm^2/g)**	**ε (μm)**
1.0	9.085×10^3	1.809×10^{-2}
1.5	3.399×10^3	4.836×10^{-2}
2.0	1.626×10^3	1.011×10^{-1}
3.0	5.576×10^2	2.948×10^{-1}
4.0	2.567×10^2	6.403×10^{-1}
5.0	1.398×10^2	1.176
6.0	8.484×10^1	1.937
7.1	5.319×10^1	3.090
8	3.056×10^2	5.378×10^{-1}
10	1.706×10^2	9.635×10^{-1}
15	5.708×10^1	2.880
20	2.568×10^1	6.401

The transmitted intensity discussed is taken as the X–ray spectrum from the feature (such as MnS) within a pit. The hypothetical incident intensity on the inclusion is taken as a spectrum collected from the level surface directly next to the pit under identical conditions. The transmitted X–ray intensity of interest is the Bremsstrahlung radiation that forms the continuous background in the X–ray spectrum. This provides a continuous functional relationship between the attenuation of the transmitted intensity and the path length through the medium, because it is a continuous function of X–ray

energy. Also, its intensity is independent of the elemental composition of the information volume from which the X–rays were emitted. These are reasons the incident X–ray intensity from the MnS inclusion can be interpreted as analogous to a spectrum collected from the steel alongside the pit under identical measuring conditions. The MnS inclusions investigated in this study emit a clear range of continuous radiation clear of substantial interference from characteristic X–rays between the sulfur K – α and manganese K – α lines (~2.5 – 5.5 keV), making this system accessible to measurement of pit depth; this topic is discussed in Future Work.

It is clear that the attenuation increases with decreasing energy from the calculated values of skin depth as a function of X–ray energy in Table 11. This explains the loss of low-energy X–ray intensity from EDX spectra taken from deep within pits. The ratio of the transmitted and incident X–ray intensities is indicative of pit depth, an important corrosion parameter. For example, if a 4-keV X–ray intensity in the EDX spectrum decreases by a factor of 2*e* compared to the background on a steel sample, the path length taken through the metal can be concluded to be ~1.5 μm.

This result, combined with the application of the geometry of the transmitting volume and the X–ray/sample geometry, gives great insight into the depth of features on any metal surface that have dimensions on the order of the skin depth of that metal. Features on this scale are those often encountered in SEM applications, and most modern systems are equipped with X–ray detectors capable of acquiring high-resolution EDX spectra. The applications are obvious. To name a couple, the method could reveal the depths of corrosion pits and measure the heights of different domains in corroded steel,

giving measures of differential corrosion or of general corrosion when measured against carbide fins. The method has high spatial resolution and is faster, more streamlined and more accessible than other 3–D imaging techniques, such as confocal microscopy, digital microscopy, AFM, or photogrammetry.

Examples of the types of pits induced around MnS inclusions under exposure to the various media are given in the following subsections. Some examples come from coupons after exposure to Clark solution. FEM images acquired with 1- and 20-keV primary beams are provided along with accompanying EDX spectra from significant spots.

Sterile ALDC Medium

These pits formed radially around MnS inclusions, which were always found still within the pit. Their diameter was approximately 5-6 μm. A typical example of these pits was illustrated in Fig. 62 and the succeeding discussion.

Fig. 65 is of a large pit that formed as a result of multiple smaller pits combining. Multiple MnS inclusions are left behind, at the centers of the constituent pits. Inclusion #3 appears to have formed the main pit, whereas inclusions #1 and #2 formed on the main pit walls as secondary pits. Inclusion #1 appears to be inducing the most severe pitting, as evidenced by the visibly deep trench around it. This inclusion contains copper in amounts detectable by EDX, whereas the other two do not. Carbide fins of pearlite were etched around during formation of the pit, indicating that the α-ferrite phase was preferentially etched over the harder carbide.

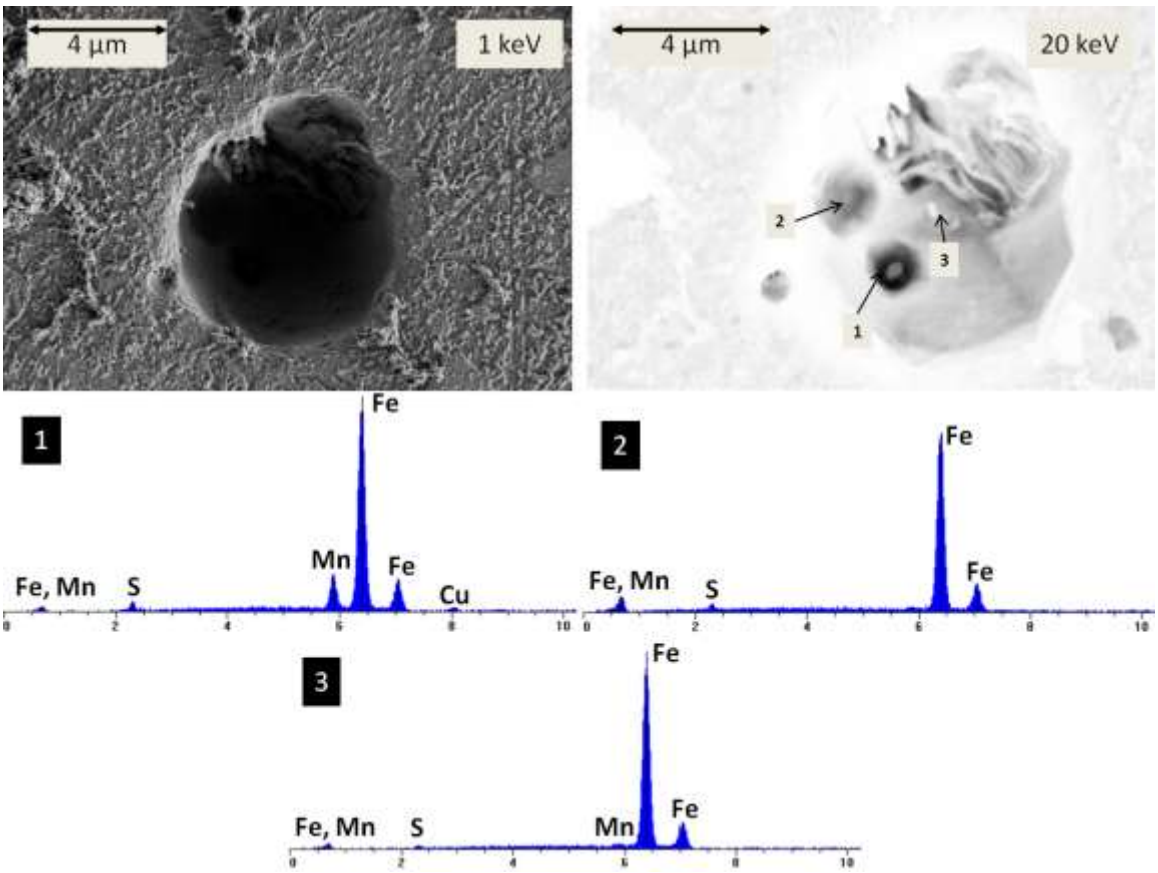

Figure 65: Localized corrosion around a group of active MnS inclusions has resulted in a large pit on a coupon surface corroded by sterile ALDC medium with [Na_2S] = 0.05 mM for two weeks.

Because of the lack of biofilm and thick corrosion deposits, none of these samples were treated with Clark solution for further analysis.

Abiotic Sulfide Control

Pits were found growing deeper and radially around inclusions on coupon surfaces exposed to the abiotic sulfide control; these were approximately 5-6 µm in diameter. Also found were pits without any mineral inclusion remains within, indicating that whatever had generated the pit was now hidden. These pits extend very deep and out of the range of secondary electron imaging. An example is given in Fig. 66.

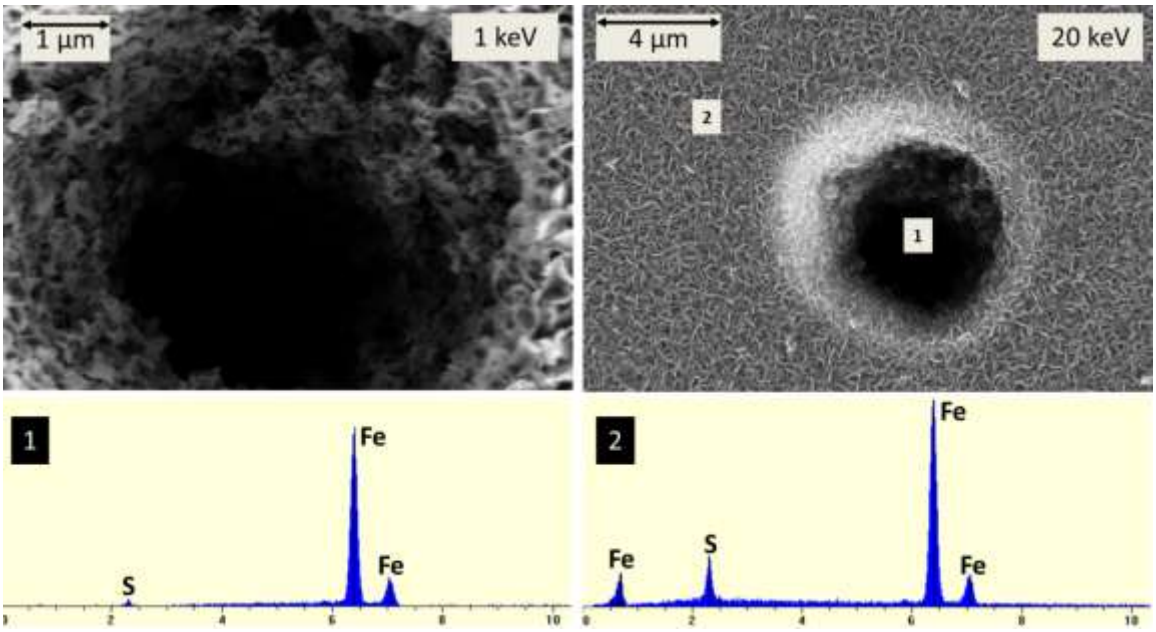

Figure 66: A corrosion pit on a coupon surface corroded by abiotic sulfide solution with [Na_2S] = 25 mM for two weeks.

It is noteworthy that the corrosion deposit extended deep into the pit and even changed in morphology, as shown in the high-magnification 1-keV image.

The example in the previous figure had no MnS inclusion left, but a very similar pit was found on a coupon corroded by 30 mM sodium sulfide in pure water. Close investigation revealed that this one did contain an MnS inclusion located at the center and bottom of the pit.

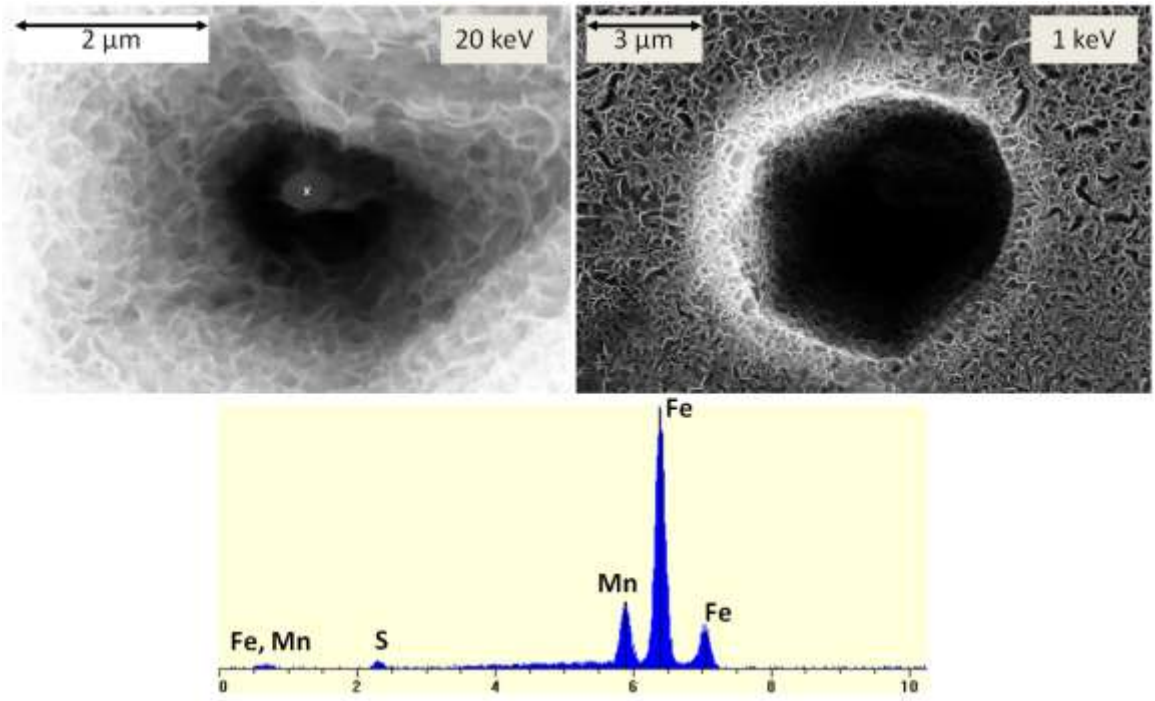

Figure 67: Corrosion pit around MnS inclusion on coupon surface corroded by abiotic sulfide in nanopure water with [Na_2S] = 30 mM for six days and accompanying EDX spectrum.

Pits could not be found on coupons corroded with ALDC or *D. indonensis* filtrate before treatment with Clark solution. This is probably due to a thick corrosion deposit that covered the surface and consequently all of the pits. All of the examples given here are of samples treated with Clark solution.

ALDC Filtrate

Pits were found with 5-6-µm diameters generating radially from centers. It was presumed that these were MnS centers but that the acidification due to corrosion had removed them. The morphology of the pits is clearly different from the other examples. These pits have walls with many jagged and sharp edges, indicating that pits are forming inside pits. The reason for smooth walls in abiotic pits and jagged walls in biotic pits is

the acidification of the pit regions due to the occlusion of the pits by the formation of biofilms in these areas creating pockets of low-pH zones causing the dissolution of MnS inclusions and increasing the local abiotic H_2S.

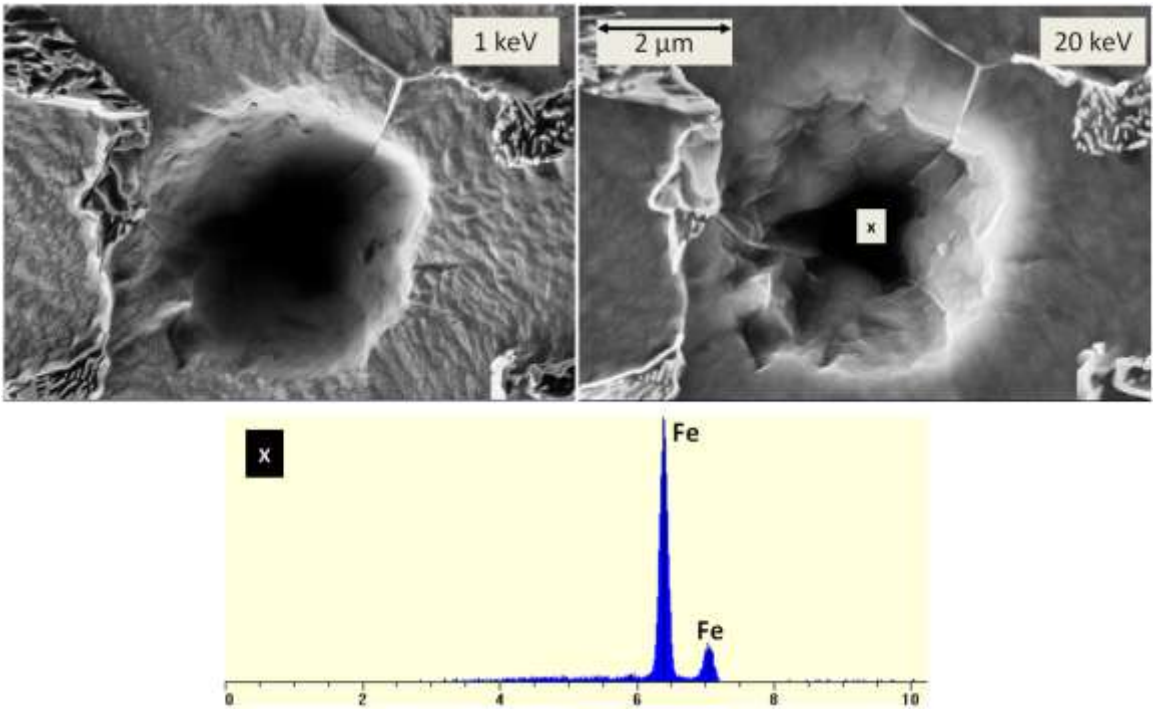

Figure 68: Corrosion pit on a coupon surface exposed to ALDC filtrate for two weeks after the removal of corrosion deposits by treatment with Clark solution.

Figure 69 is of a feldspar inclusion that contained regions, especially around the border, which had been preferentially etched away. These are presumed to have been highly strained. However, these pits did not grow because, unlike MnS inclusions, other inclusions do not produce abiotic H_2S as they dissolve. Also present in the EDX spectrum are P and Ti. Inclusions of this sort were found with an array of impurities before exposure, and these elements were among them, so their presence is of no surprise. The differential appearance of the corroded iron between grains in the 1-keV image is noteworthy.

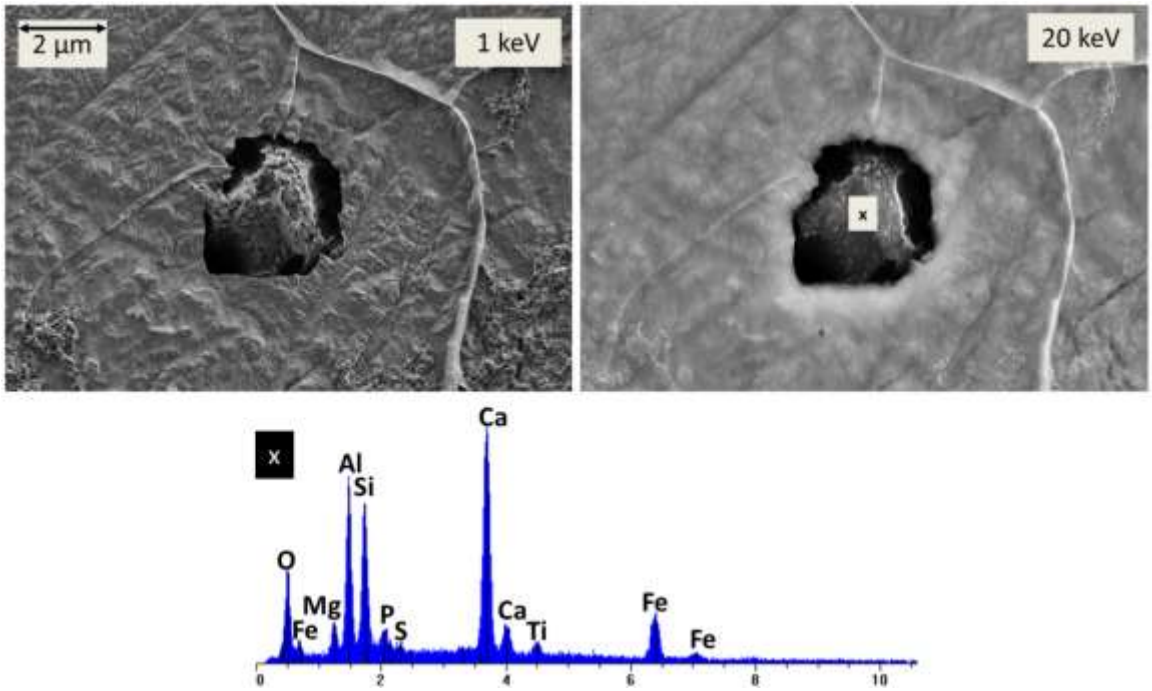

Figure 69: Corrosion induced in strained region immediately surrounding feldspar inclusion after exposure to ALDC filtrate for two weeks and the removal of corrosion deposits by Clark solution. Corrosion did not advance beyond this stage.

ALDC Cell Culture

Circular pits, again ~5 µm in diameter, were found on coupon surfaces after corrosion by ALDC cell culture without the aid of Clark solution. An example of one of these is given in Fig. 70. The pit is very deep, and, consequently, the inclusion remains cannot be seen within, although they register on the EDX. The corrosion deposit surrounding and sinking into the pit is reminiscent of that on coupons exposed to the abiotic sulfide control.

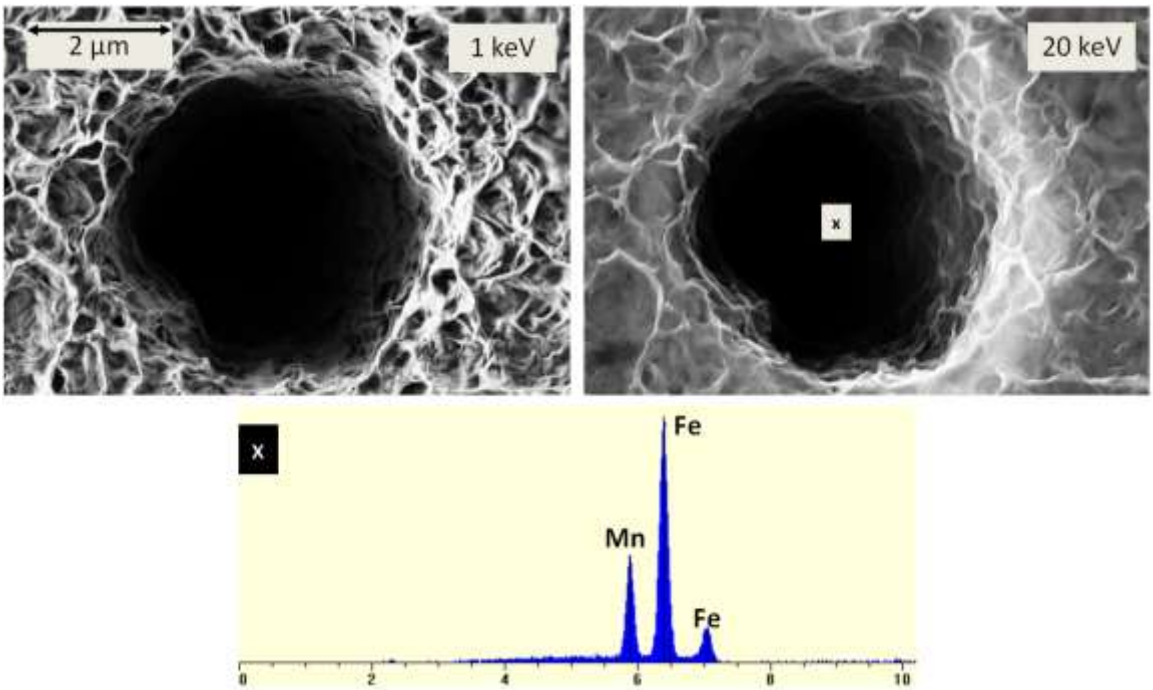

Figure 70: Corrosion pit containing MnS that is invisible to FEM but not hidden from EDX. The coupon surface was corroded by ALDC cell culture for two weeks.

Other pits, however, were found with their inclusion remains still intact, such as the example given in Fig. 71. This inclusion is seen diving deep into the pit. When only the tip was exposed to the surface, the pit initiated radially, and so formed a circle. As the pit progressed, the inclusion turned so that it was slightly more parallel with the sample surface, and so the pitting became a square. The Si in the EDX spectrum is an impurity in the inclusion.

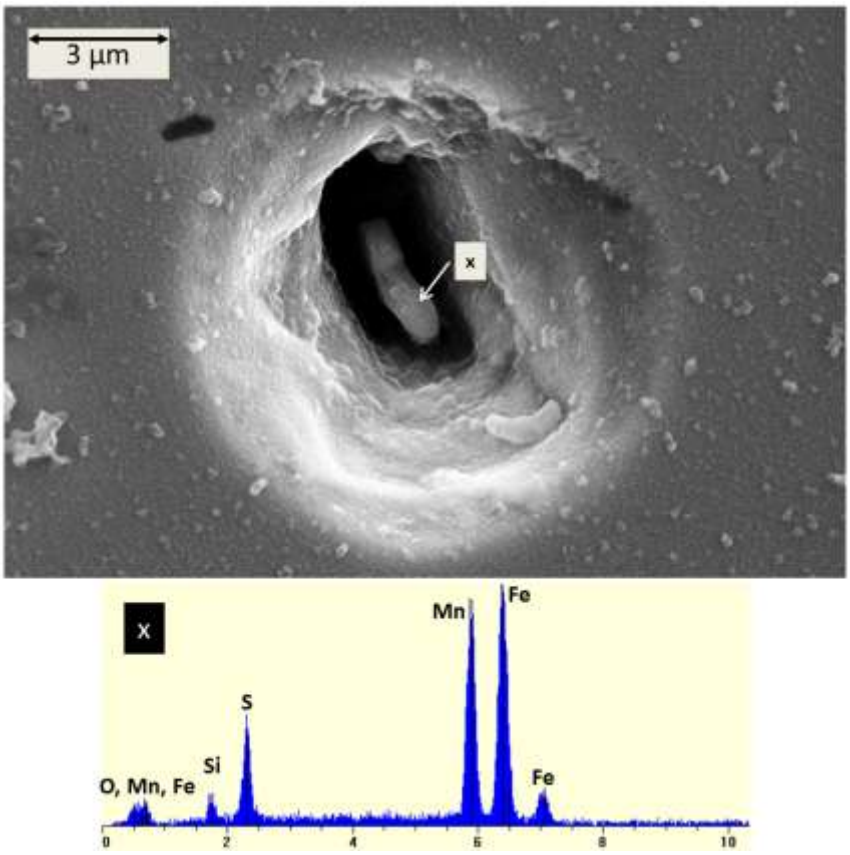

Figure 71: Corrosion pit on coupon surface corroded by ALDC cell culture for two weeks. The MnS inclusion is still visible within the pit.

<u>*D. indonensis* Cell Culture</u>

One morphological difference between coupons corroded by ALDC and coupons corroded by *D. indonensis* was square-shaped pits around MnS inclusions. These were of the same dimensions as the other pits, a few microns extending from the pit center. An example is shown in Fig. 72.

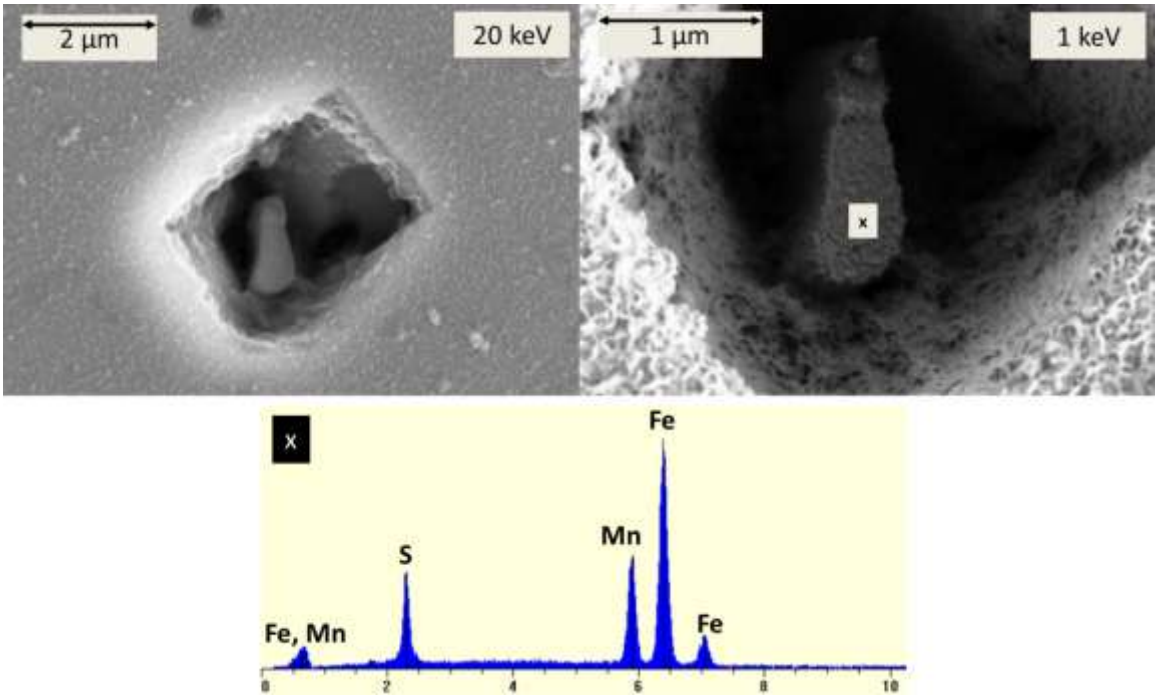

Figure 72: Localized corrosion in the shape of a cube around an MnS inclusion after exposure to *D. indonensis* cell culture for two weeks.

An example of multiple pits forming a large networked pit is given in Fig. 73. Overlapping squares are clear from multiple pits around the multiple MnS inclusions. Different pits are seen at different stages of development. Two of these, labeled #1 and #2, are pointed out. The pitting around inclusion #2 has progressed significantly deeper than that around inclusion #1, despite the fact that the square pits around them are of roughly the same size.

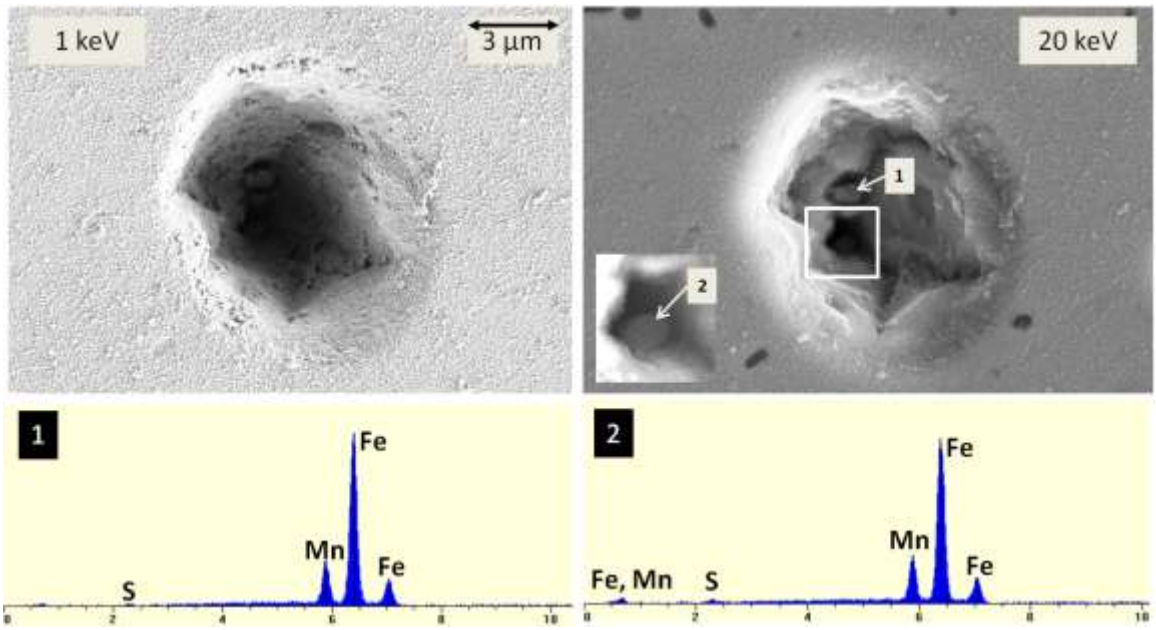

Figure 73: A group of cubic pits around MnS inclusions on a coupon surface corroded by *D. indonensis* cell culture for two weeks has formed into a single large pit.

After treatment with Clark solution, pits were found of approximately the same size but devoid of mineral inclusions and possessing the remains of a cap. The pit shown in Fig. 74 is an example. The cap atop the pit looks exceptionally complex, with clear, different structures of biofilm and corrosion deposit all mixed into one consortium. However, it is thin enough not to be detected by EDX; the high-energy primary beam penetrated it and continued down into the pit bottom.

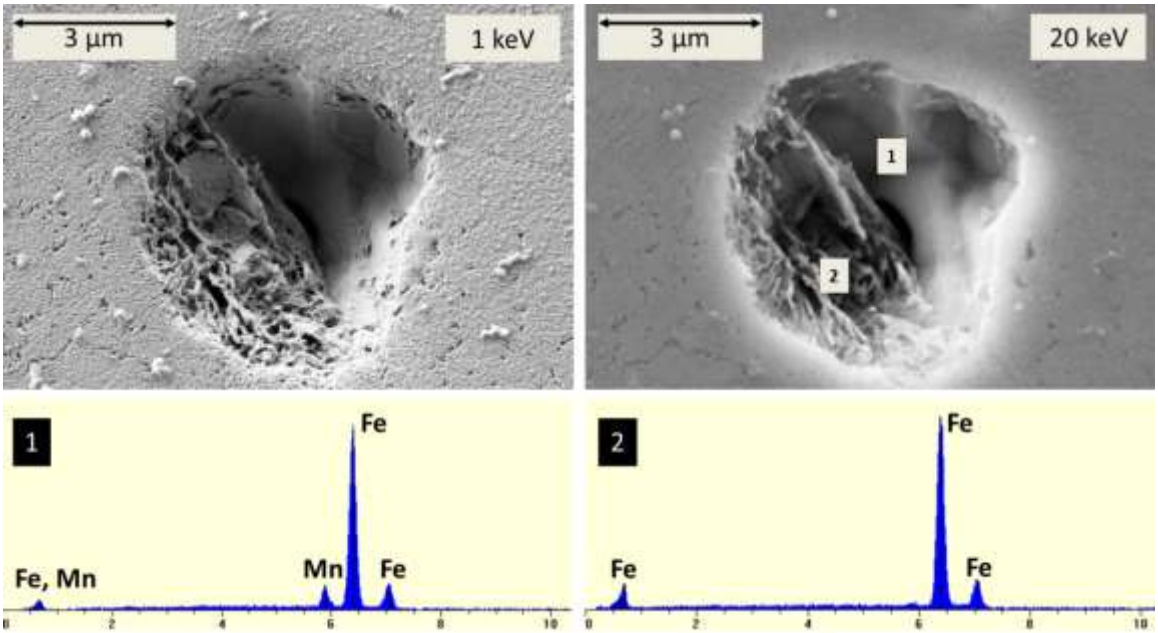

Figure 74: A group of circular pits has formed into a single large pit on a coupon surface corroded by *D. indonensis* cell culture for two weeks. The MnS inclusion was not visible to FEM, but the Mn characteristic peak was clear in an EDX spectrum taken from the pit center. Also of note are the remains of a cap, although it cannot be resolved by EDX.

Summary

These results may be summarized as follows. Pits develop at this stage (after two weeks' corrosion) to a size approximately 5-6 µm across. Pits developed deeper and radially from the inclusion center. In the case of coupons corroded by the *D. indonensis* cell culture, these were square; in all other cases they were circular. Some pits exposed to biotic solutions showed the remains of caps. Severe corrosion induced in biotic solutions required Clark solution to reveal the pitting underneath. Pits were seen with and without inclusions left within, although EDX sometimes confirmed MnS within the pit when FEM could not see it. In some cases, pits formed inside other pits and combined to form larger, networked pits.

Biofilm

Biofilm was observed on coupons exposed to the cell cultures of ALDC and *D. indonensis*. The FEM image in Fig. 75, of a region heavily infected with biofilm, so much so that not all of it was removed by a 5-second immersion in Clark solution, shows a high density of small pits. To provide a better view of the biofilm and sample surface, a higher-magnification image is given in Fig. 76. The ALDC cells are rod-shaped and approximately 2 µm long, and they are seen on the sample surface and tangled in leftover biofilm and corrosion deposit.

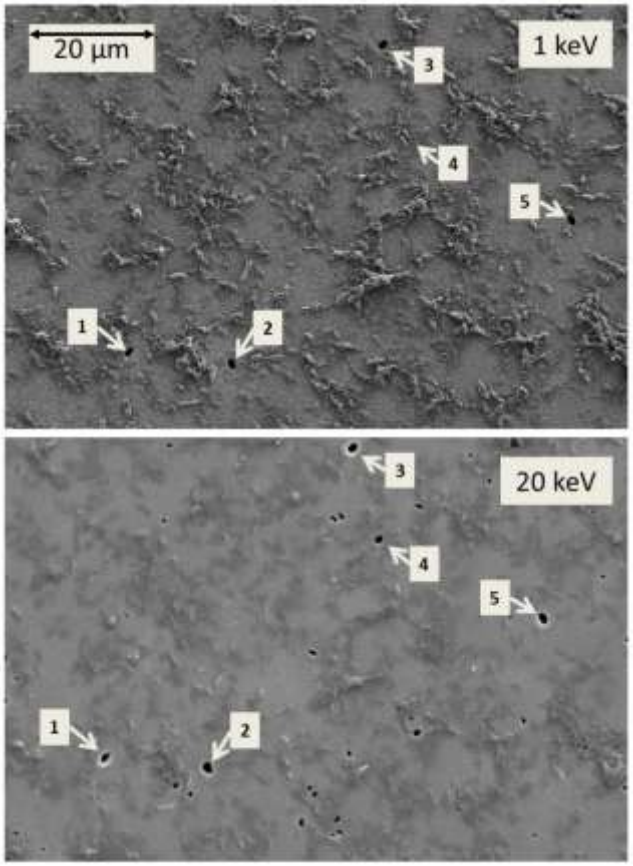

Figure 75: Biofilm occluding pits and MnS inclusions on coupon surface corroded by ALDC cell culture for two weeks and subsequently treated with Clark solution to remove corrosion deposits. The five pits visible on the surface in the 20-keV image are indicated.

The 20-keV image, shown for comparison in Fig. 75, reveals the sample surface below the leftover biofilm and corrosion deposit. MnS inclusions and pits appear as black spots underneath the biofilm. Here is another application where 1- and 20-keV images provide very useful complementary information. Further study could be done in combination with the pit counting program used to calculate MnS distributions to find the ratio of MnS inclusions with biofilm colonization to those without. This would shed light on whether or not these microbes specifically use dissolving Fe^{2+} ions around the MnS inclusions for metabolic activities. One pit, labeled #4, is actually seen below the biofilm in the 20-keV image but is hidden in the 1-keV image.

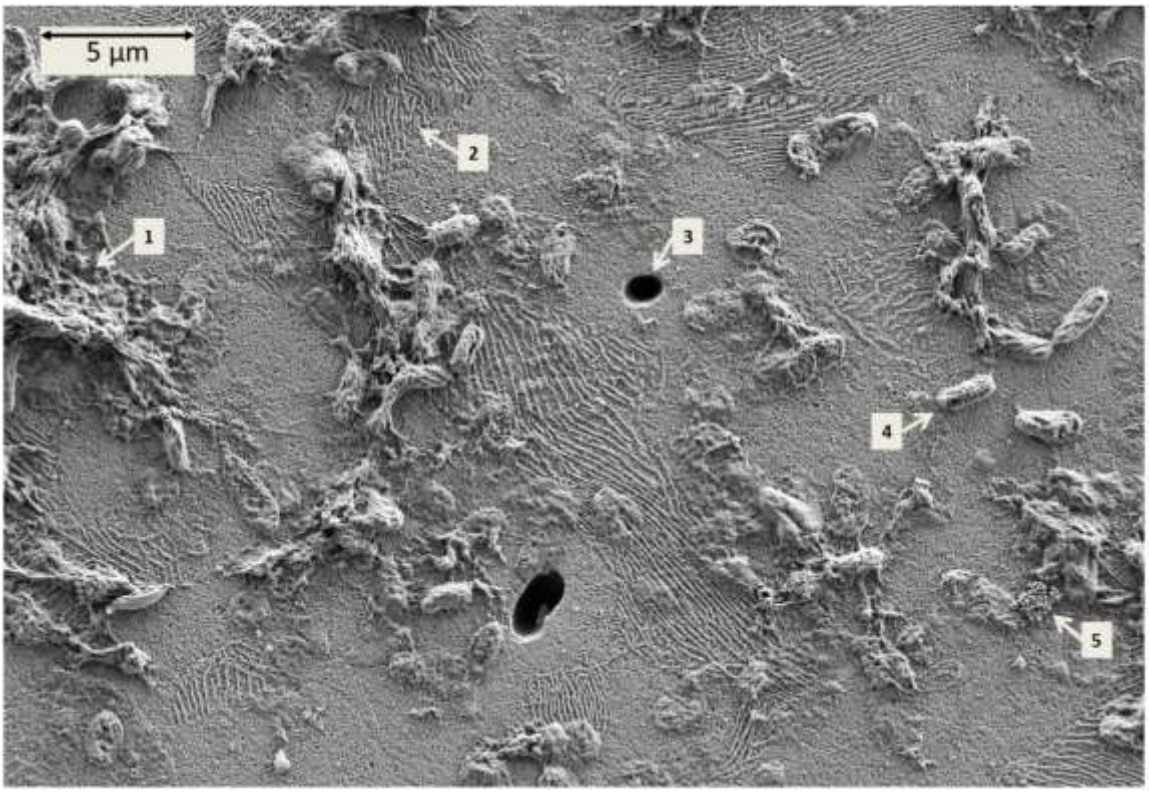

Figure 76: High-magnification image of the same area as in Fig. 75 on the coupon surface corroded by ALDC cell culture for two weeks. Indicated are biofilm (1), etching around carbide (2), a pit (3), a single ALDC cell (4), and an interesting deposit of spheres that is of note (5).

Comparison of these pits with the dark spots of the MnS inclusions on the 20-keV image in Fig. 75 shows that they are larger, and so are not simply exposed MnS inclusions that were dissolved by Clark solution. Their high concentration suggests that the biofilm accelerates the pitting process by initiating more pits.

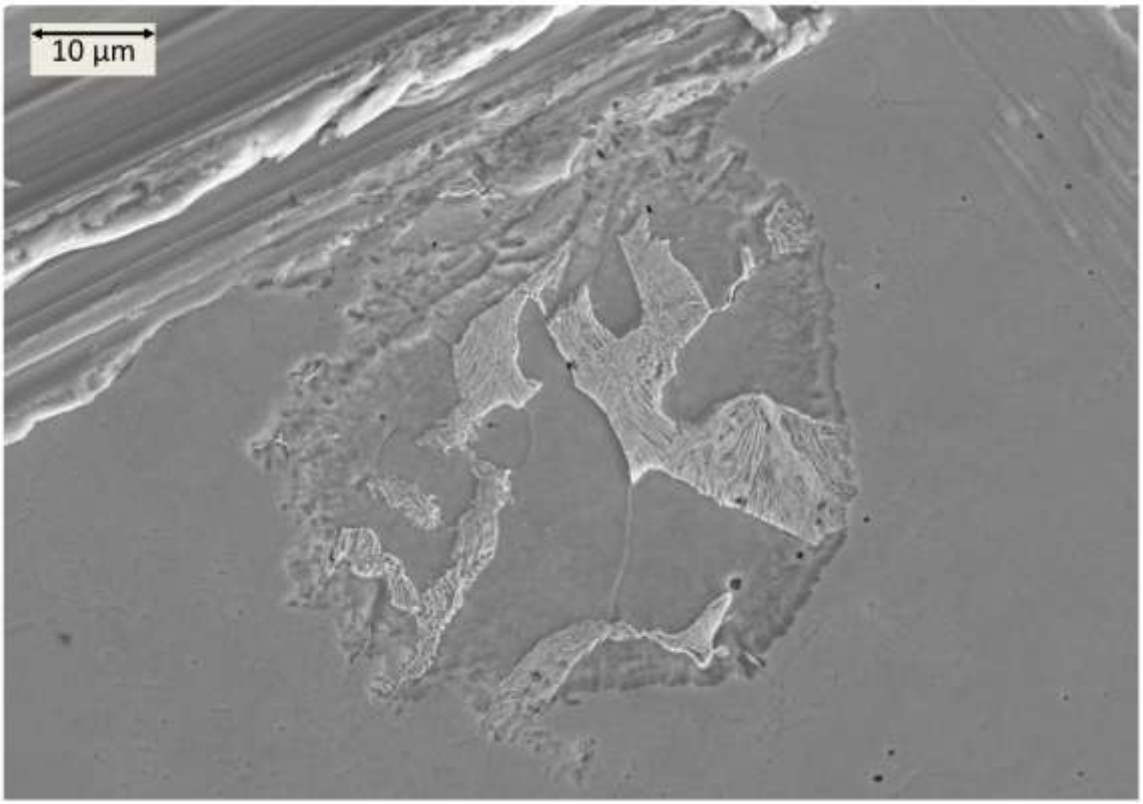

Figure 77: Region on coupon surface corroded by ALDC cell culture for 11 days. There is clearly a circular area that corroded at an accelerated rate relative to its surroundings, as indicated by the deep etching of ferrite that has occurred around the harder carbide in pearlite. Note the X scribed on surface for tracking inclusions.

Figure 77 is an FEM image of a large region that underwent accelerated corrosion relative to the surrounding steel surface. This could be due to a biofilm or corrosion products that formed over the region, creating an isolated environment that resulted in the demarcation. The area was found after treatment with Clark solution, so any

biofilm/corrosion deposit would have been removed. The accelerated corrosion is obvious from the etching around the pearlite relative to the surroundings, which forms our measuring stick for corrosion.

CONCLUSIONS

The chief result was that in all corrosive media some mineral inclusions yielded to pitting while others did not. MnS inclusions were found to be the sites of the most severe pitting, which developed as a deep trench around the inclusion edge, leaving the inclusion as an island in the pit void. Inclusions of other compositions, such as Si or pure feldspar, initiated pits in their surroundings but did not grow and develop to form deep, wide pits.

Exceptionally corrosively active regions in the matrix of MnS inclusions occur because (1) the initiation of the pits is due to residual strain in the Fe located in the immediate surroundings of the MnS; (2) the dissolution of Fe^{2+} ions leads to acidification of the local region through hydrolysis, $Fe^{2+} + 2H_2O \rightarrow Fe(OH)_2 + 2H^+$, and (3) the dissolution of MnS at low pH due to $MnS + 2H^+ \rightarrow H_2S + Mn^{2+}$ produces local abiotic H_2S in the pits, which promotes the growth and development of the pits. Because of this last effect and the unusually long lengths (100s of microns) of MnS inclusions (and inclusions of other sulfides, such as Cu_2S) are the most dangerous trace minerals in the Fe matrix.

The specific elemental composition of individual MnS inclusions on clean steel was determined using Auger nanoprobe, which possesses the resolution to reveal that each inclusion has a unique composition, and depth profiling, to show that it varies as a function of depth. EDX can be used to verify whether an inclusion is MnS or not, but in most cases cannot resolve the fine structure. As of yet, no extensive studies have been done on the sort of large corrosion pits presented in this work by the Auger nanoprobe; therefore, exactly which inclusion compositions lead to enhanced pitting is yet to be

verified. We hypothesize all localized corrosion in Fe is driven by the residual strain distribution. Trace mineral impurities or the metallurgical processes introduce a residual strain distribution throughout the Fe. This strain is more pronounced in the immediate surroundings of inclusions, where Fe meets the inclusion. These areas are potential local areas for pits to initiate.

The severity of pitting corrosion was measured by the number of pits that developed on a steel surface in a given period of time and by how advanced the stage of propagation of the pits was. We found that biotically corroded coupons were more severely pitted than abiotically corroded coupons from the density of pits on their surfaces, and that is the pitting corrosion correlated with the distribution of MnS inclusions. Also, large pits on coupons exposed to biotic solutions and abiotic sulfide were found without any visible MnS inclusions left within them, although the remains of MnS inclusions could sometimes be found, indicating an advanced stage of corrosion in which the inclusion has finally yielded to the acidification of the pit and dissolve. All pits observed on the coupons corroded by sterile ALDC medium had an inclusion clearly visible within the pit.

The general corrosion on coupons exposed to biotic solutions was likewise accelerated. This was evidenced by the mass loss data, which showed coupons losing more mass to a biotic SRB solution. Also, the corrosion of ferrite around carbide fins in pearlite structures illustrated the depth of the iron layer lost to corrosion in biotic solutions compared to abiotic solutions, which did not exhibit the effect strongly.

The microbially accelerated corrosion is attributed to the formation of biofilms over inclusions on the surface that create pocket microenvironments and the production of alternative electron acceptors that serve to enhance the corrosion. A particularly thick biofilm may lead to an especially dense group of pits (see Fig. 75) or a large region of accelerated corrosion (see Fig. 77).

Pit Initiation and Propagation

The pit microenvironment begins with the dissolution of the strained iron metal around the MnS inclusion.

(19) Anodic reaction: $Fe^0 \rightarrow Fe^{2+} + 2\ e^-$

Two reactions in which these iron cations participate are recognized. Comparison of the general corrosion on coupons exposed to the biotic solutions and the abiotic sulfide control show that the dominant mechanism in both systems is sulfide-driven, with the end result of a deposition layer of FeS on the steel surface via the reaction given in equation 20.

(20) Deposition reaction: $Fe^{2+} + S^{2-} \rightarrow FeS$

FeS is a conductor under anaerobic conditions that can easily shuttle electrons from an isolated anode to many cathodes over a large volume. In a pit micro-environment, where the anodic reaction occurs on the side walls of the pits, FeS corrosion deposits can mediate the electron transfer from the confined localized region of the pit to a large volume in the bulk surroundings, where the cathodic reaction occurs through a diaspora of mechanisms. This generates a high corrosion current and consequently a high anodic current density, resulting in rapid dissolution of the metal in the pit matrix.

These anaerobic conditions are favorable for the Fe^{2+} ions to be hydrolyzed to iron hydroxide through the reaction given in equation 21.

(21) Fe^{2+} hydrolysis: $Fe^{2+} + H_2O \rightarrow FeOH^+ + H^+$, $\log([FeOH^+] / [Fe^{2+}]) = -7 + pH$

This acidifies the environment and produces the oxygen deposits shown within the initiated corrosion around the edge of the MnS inclusion of Fig. 49.

We observe in some cases that corrosion deposits in the early stages of pit initiation shows the formation of a porous cap structure around the MnS inclusion. The elemental composition of this cap has not yet been understood, but preliminary data suggest it is composed of elemental S and iron oxide deposits. A pit with a clearly developed cap on a coupon surface after exposure to sterile ALDC medium is given in Fig. 78.

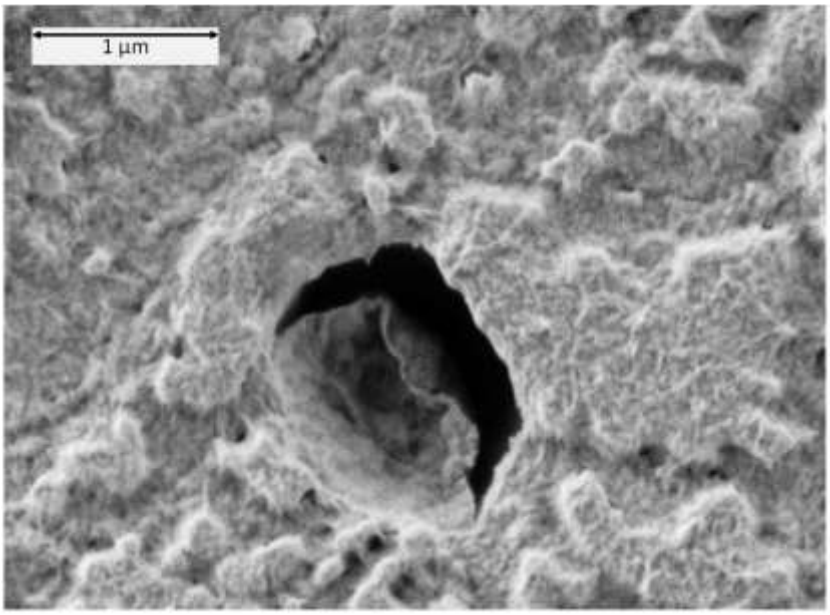

Figure 78: Corrosion pit with cap on coupon surface corroded by sterile ALDC medium with $[Na_2S] = 0.05$ mM for two weeks.

Cracks and chimneys in the cap will allow the diffusion of some anions into the pit and some cations out. Negative chloride ions will diffuse inward to balance the outward flow of positive iron cations. These adsorb on the pit walls and push the conduction electrons away from the surface, causing the dissolution of Fe^{2+} from the Fe matrix. Chloride anions are highly concentrated in anaerobic marine sulfidogenic environments, and our media possess 300 mM concentrations.

As time passes, all these factors make the pit microenvironment more and more acidic. Eventually, at a sufficiently low pH, the MnS inclusion itself will begin to dissolve according to equation 22.

(22) $MnS + 2\ H^+ \rightarrow H_2S + Mn^{2+}$

Combining the hydrolysis of Fe^{2+}, $Fe^{2+} + H_2O \rightarrow FeOH^+ + H^+$, with the dissolution of MnS, $MnS + 2\ H^+ \rightarrow H_2S + Mn^{2+}$, is the key to understanding accelerated pit initiation and pit development. Hydrolysis reactions lower the pH under occluded regions, while the dissolution of MnS locally supplies H_2S abiotically in the region to act as an electron acceptor in addition to protons and other electron acceptors. The combination of these two processes fuels the pit initiation and development process. At normal pH, on the average only 2 pits per mm^2 are observed. However, there are on the average 4200 MnS inclusions per mm^2. Although at normal pH these do not pose a threat, at high pH each and every one of these inclusions is a potential pitting threat. Therefore, at a low pH, instead of 2 pits, we may have, in principle, 4000 pits per mm^2. These pits will propagate along the MnS microwires, joining other pits and leading to macroscopic pitting in some cases.

This model describing the mechanism of pit initiation and propagation in anaerobic marine sulfidogenic environments is summarized and illustrated in Fig. 79. Refer to the figure caption for details.

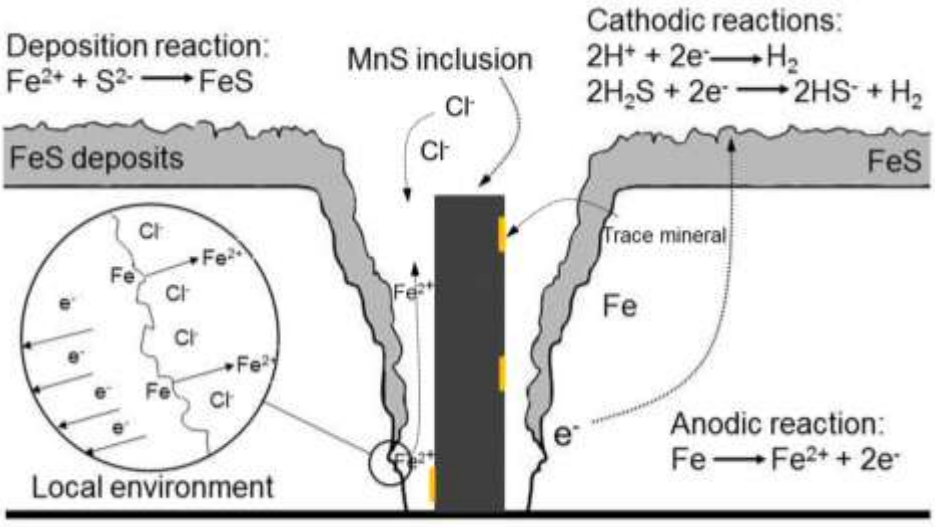

Figure 79: Corrosion mechanism at an active MnS inclusion: MnS inclusions do not dissolve in the initial stages of pit initiation under normal pH conditions. The areas surrounding some inclusions are highly susceptible to anodic attack because of the contamination of these areas causing disorder and residual strain in the Fe matrix. The adsorption of Cl^- ions on the surface chases away the conduction electrons of the strained matrix and results in the anodic dissolution of iron from these regions. Cathodic and depositional reactions perpetuate the corrosion process indefinitely, since under anaerobic conditions FeS deposits cannot block the cathodic reactions because of the high conductivity of FeS deposits.

Closing Remarks

The biological systems studied here are highly complex and need special attention if high-precision physics is to be applied. To analyze the reality of corrosion induced by biological systems, we have used nanoscale methods that can measure to a few nm (1/100,000 the width of a human hair). However, we are dealing with richly diverse microbial life forms, which may be changing their environment on a much greater scale.

Biophysics requires a progressive mind that extends beyond the traditional schools of thought held in both physics and biology. It is on the cutting edge of an increasingly technological society that is waiting to be discovered.

FUTURE WORK

Current Direction in Project

The model of the fuel tank presented here is not the practical reality of the true system; instead, it is meant to provide the basic groundwork for developing a more complete, and hence more complicated, model. The objective of the MURI project as a whole is to establish the extent to which microbial life influences the degradation of fuels and tank materials within SWFBTs. Corrosion experiments are currently underway in ICAL that integrate Navy fuels and microbial consortia that comprise both aerobic bacteria (model bacterium *Marinobacter*) and anaerobic SRBs. These experiments are analogous to the ones described here, but involve seawater with a layer of fuel that sits atop, all contained within the same sample vial with the microbial culture. Instead of steel coupons on the bottom of the vial, coupons are exposed to different levels of the fuel/aqueous profile. The oxygen profile of this system determines the regions the different microbes will populate and their synergistic relationship, and is measured by high-spatial-resolution dissolved O_2 sensors.

Metabolites are continuously assimilated and dissimilated (especially those that revolve around reduced or oxidized species of carbon, sulfur, and oxygen) by the aerobic and anaerobic bacteria. They are utilized and transformed by both types of bacteria in complementary ways, weaving the synergistic network in which the metal plays a critical role for its contribution of electrons. This has major consequences on the corrosion of the metal, and so these systems are currently of primary concern.

Further Studies

Corrosion Products

An aspect of this work that requires further attention, and illustrates the complexity of these systems, is the role played by different corrosion products. Models, such as the one described, that involve coupons corroded by consortia of aerobic and anaerobic bacteria and different solutions introduce a much wider gamut of corrosion deposits. Fig. 80 is of unique mineral deposits found on a coupon exposed to the sterile SRB medium (left) and the ALDC cell culture (right); the environments of these coupons were not necessarily strictly anaerobic. The roles of trace O_2 in solution and related mineral deposits such as these in corrosion are not currently understood, but must be studied for us to have a more realistic assessment of the corrosion mechanisms in suboxic environments.

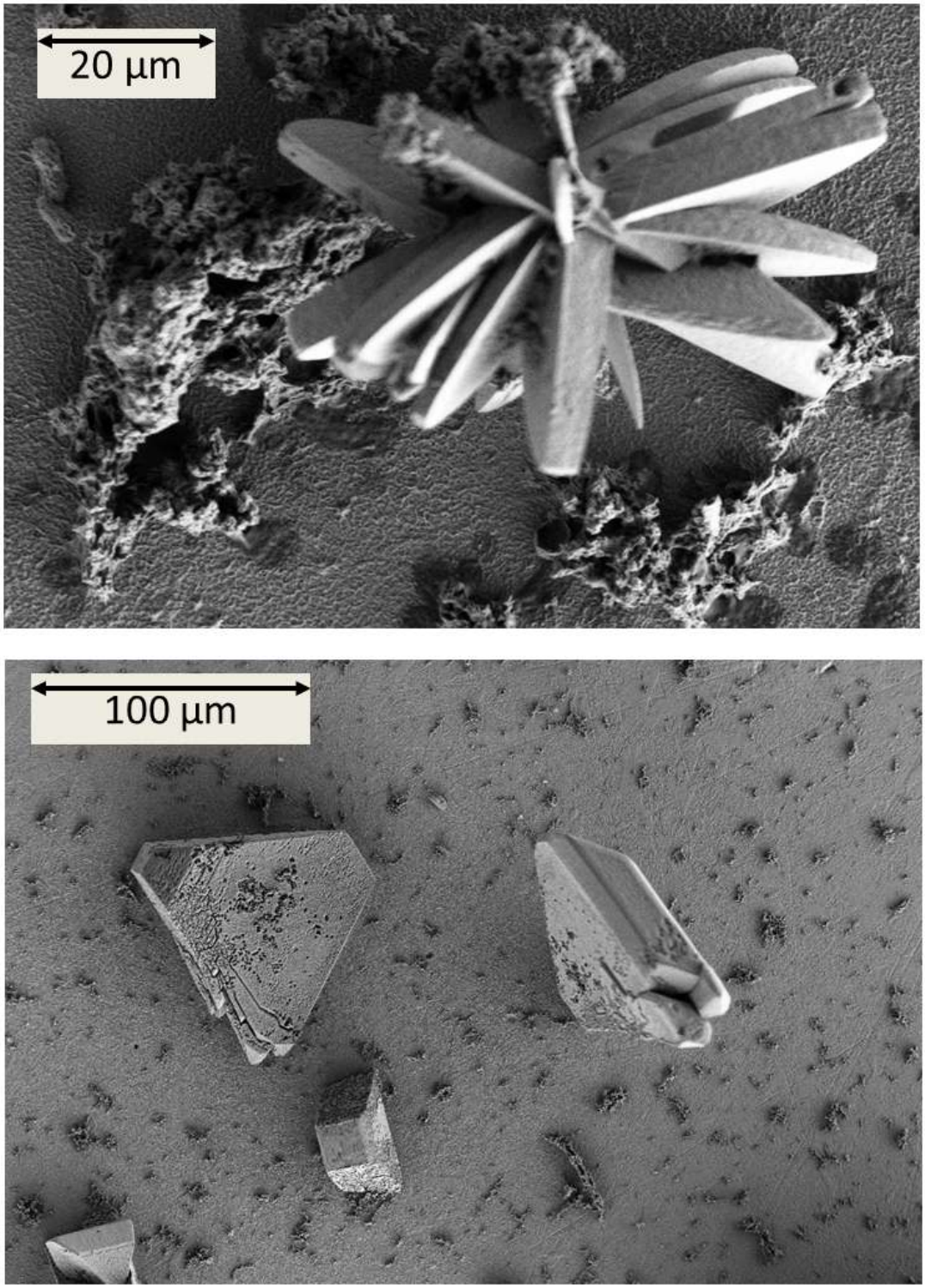

Figure 80: Unique corrosion mineral deposits found on coupon surfaces corroded by (top) ALDC cell culture and (bottom) sterile ALDC medium, both for two weeks.

Measurement of Pit Depth
by X–Ray Attenuation

As mentioned in Results, by measuring incident and transmitted X– ray intensities using EDX in the FEM and tabulating the mass attenuation coefficient, we are able to deduce the path length, *d*, of the X– rays through the material, leading to a measurement of pit depth (*depth* = cosine (55^0) × (*d* + *D*)). This was done by calculation in a MATLAB program. However, as of yet, a suitable control for measuring depth has not been produced, making it a subject for further study. The progress made thus far is presented.

The NIST-provided mass attenuation coefficient is for iron, and so it should be noted that this is approximated to carbon steel. Also, only twelve data points in the energy range of interest are tabulated, so the mass attenuation coefficient as a function of photon energy, μ (E), was fitted to power law functions. The sharp kink in the mass attenuation coefficient/energy relationship at ~7 keV demands the relationship be split into two functions, μ_1 (E) (equation 23) in the energy domain of $0 \leq E < 7$ keV and μ_2 (E) (equation 24) in the range of $7 \leq E < 20$ keV. These were fitted to the energy domains of 0 – 7.1 keV and 8 – 20 keV, respectively, in the NIST-provided data set given in Table 12.

(23) $\mu_1(E) = A_1 E^{-B1}$

(24) $\mu_2(E) = A_2 E^{-B2}$

The fitting parameters, with the number of-NIST provided data points in the respective sets (*N*), are given in Table 12 for μ_1 (E) and μ_2 (E) for energy in units of keV and for μ (E) in units of cm^2/gm.

Table 12: Summary of power law function fitting parameters for the mass attenuation coefficient (μ) as a function of X– ray energy (E). *A* has the same units as μ (E). *B* and *N* are unitless.

	A	*B*	*N*
μ_1 (E = 0 – 7 keV)	1.33×10^{-4}	2.62	8
μ_2 (E = 7 – 20 keV)	7.31×10^{-4}	2.68	4

Now, the path length can be easily calculated at each energy point in the EDX spectra from the mass attenuation coefficient and the incident and transmitted intensities using equation 25.

(25) $$d(\mathrm{E}) = (\mu(\mathrm{E})\rho)^{-1}\ln(\frac{I_0}{I})$$

The data are noisy so the true path length is taken to be the mean of the path lengths calculated from the energy range in which Bremsstrahlung X- rays dominate the spectrum.

A control for measuring the depths of features to high accuracy in the AFM and then with the X– ray technique described was attempted. Square pits were sputter etched into a coupon surface with a high-accuracy Ga^+ ion gun equipped into the time of flight secondary ion mass spectrometer (ToF SIMs) (courtesy of Muhammedin Deliorman), as shown in Fig. 81. The sputter time translates to the depth of the pit. Four pits were carved, with sputter times of 1×10^2, 5×10^2, 1×10^3, and 2×10^3 seconds, giving approximate depths of 1, 5, 9, and 18 μm, respectively. AFM scans and FEM images were taken from each one, as well as X– ray spectra from spots within and outside the pit, to tabulate the path length distribution.

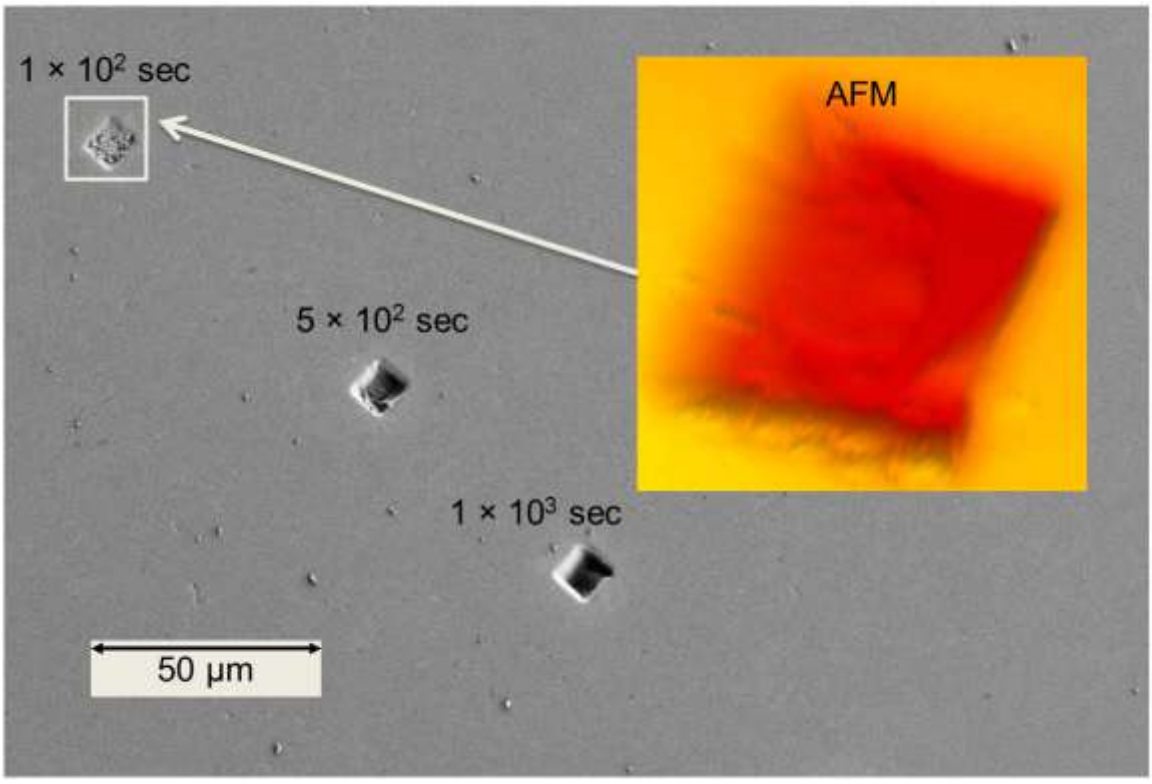

Figure 81: Squares sputter etched into coupon surface by ToF SIMS.

However, as shown in Fig. 81, the ToF SIMs did not etch the steel evenly. In the deeper pits, this created features that the AFM tip could not resolve and so did not give a reliable measurement of depth. The square pit sputtered for 100 seconds, on the other hand, was shallow enough not to create these features. A point on this pit that was thought suitable for the measurement of attenuated X- rays was measured to be 0.4 µm deep by AFM. This is only one point and therefore can only offer a calibration and does not serve as a true control.

The path length was calculated from the measured X– ray intensity attenuation between 1.5 and 5 keV for the pits, and histograms were built of the resultant distributions; these are given in Figs. 82 – 84. The fitting parameters are given in

Table 13. The X– ray detector is pointing at the specimen from the upper right-hand corner of the screen, so the primary beam is buttressed up against the top right-hand corners of the square pits to minimize the path lengths of the emitted X–rays through the vacuum.

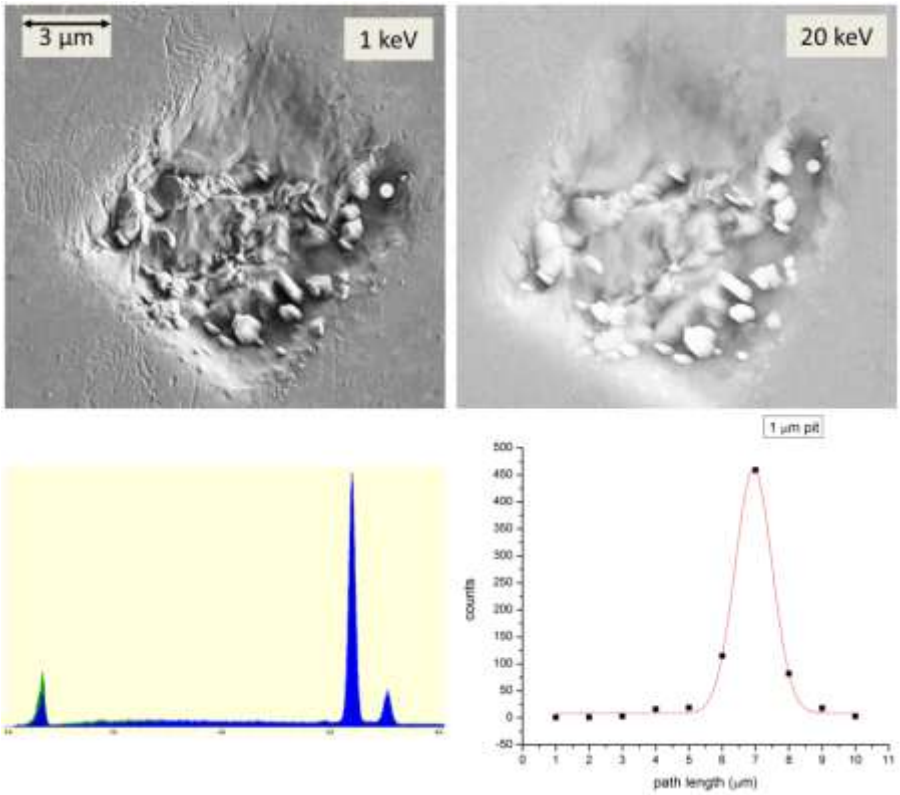

Figure 82: Targeted 1-µm-deep pit. The FEM images at 1 (left) and 20 (right) keV are given on top, and the EDX spectrum taken from the spot indicated by the white dot in the FEM images is given on the lower left. The distribution giving the pit depth is given by the chart on the lower right.

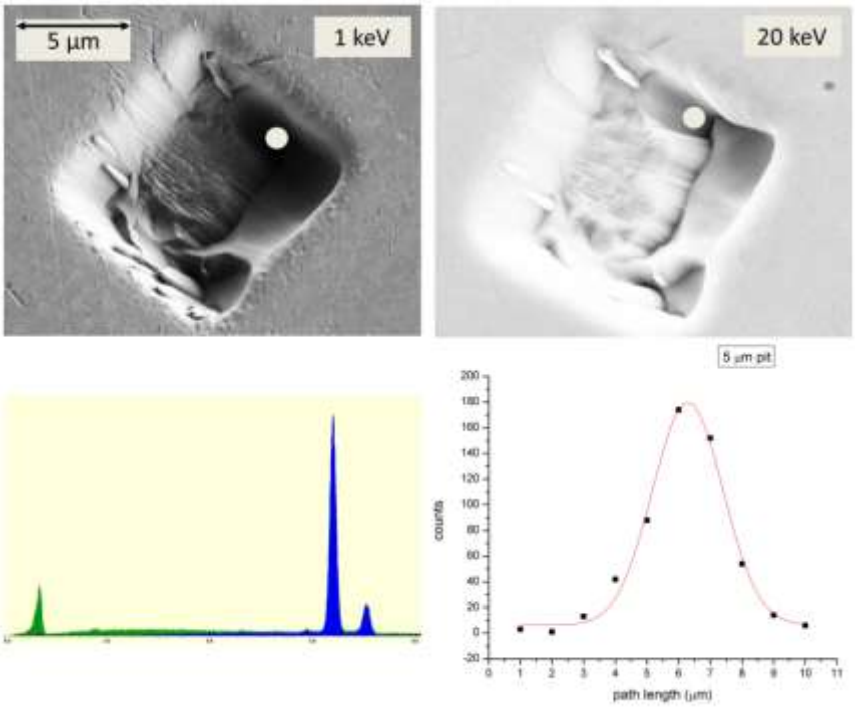

Figure 83: Targeted 5-µm-deep pit.

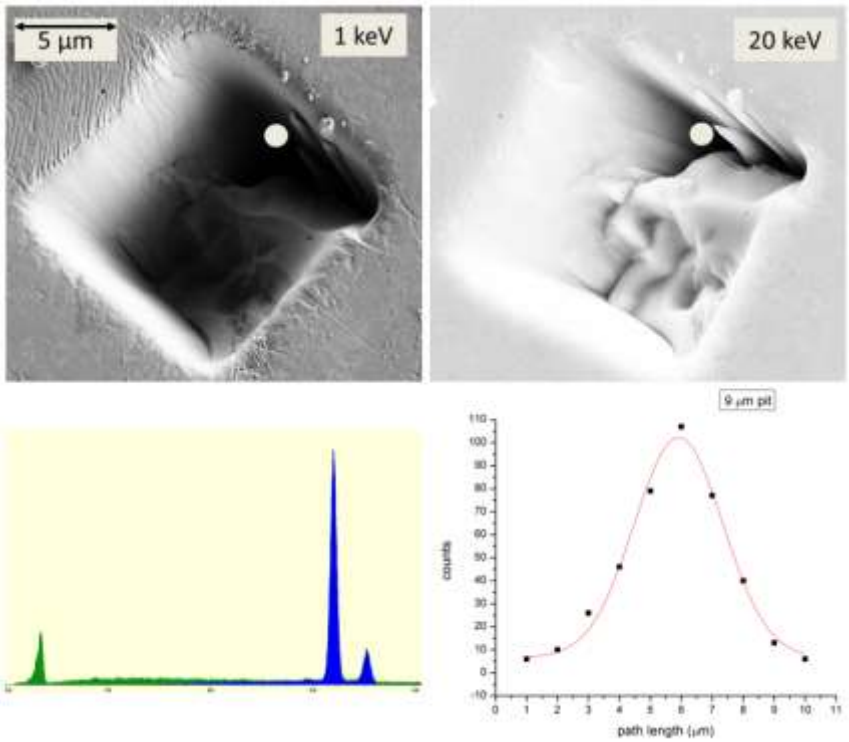

Figure 84: Targeted 9-µm-deep pit.

Table 13: Curve fitting parameters for normal Gaussian fits of the path length distributions of the 1-μm-deep, 5-μm-deep, and 9-μm-deep targeted pits. The unit is μm, except where unitless (N_0 and Height).

		1-μm pit	5-μm pit	9-μm pit
N_o	value	8.55	8.20	6.52
	error	3.15	4.00	2.94
d_c	value	0.24	3.95	5.13
	error	0.02	0.06	0.06
W	value	1.22	2.76	2.94
	error	0.03	0.16	0.18
A	value	692.30	607.73	350.13
	error	19.87	38.29	26.34
Standard deviation	value	0.61	1.38	1.47
FWHM	value	1.43	3.25	3.46
Height	value	452.71	175.67	95.14

To get the depth from the path length, multiplication by the trigonometric factor cosine (55^0) is required. It should be noted that this is a lower bound on the pit depth, because there is also an X– ray path length through the vacuum of the pit. The pit depths are given in Table 14.

Table 14: Summary of pit depths measured by the X– ray method described here and AFM.

	Measured pit depth (μm)	
	X– ray method (lower bound)	**AFM**
1 μm pit	0.1	0.4
5 μm pit	2.3	-
9 μm pit	2.9	-

To verify the results, another method for measuring pit depth was developed that utilized the variable geometry of the system, as afforded by the rotational and translational specimen stage. By tilting the stage a known amount (α) and measuring the

lateral difference in the inclusion location ($L_1 - L_2$), we could deduce the depth using simple trigonometry, given in equation 26.

(26) $$depth = \frac{L_1 \cos(\alpha) - L_2}{\sin(\alpha)}$$

A diagram of the trigonometry of measuring a pit profile is given in Fig. 85. FEM images of a corrosion pit on a coupon exposed to sterile ALDC medium with [Na_2S] = 0.05 mM for two weeks are shown both tilted 15° and flat, with the lateral distances labeled, as well.

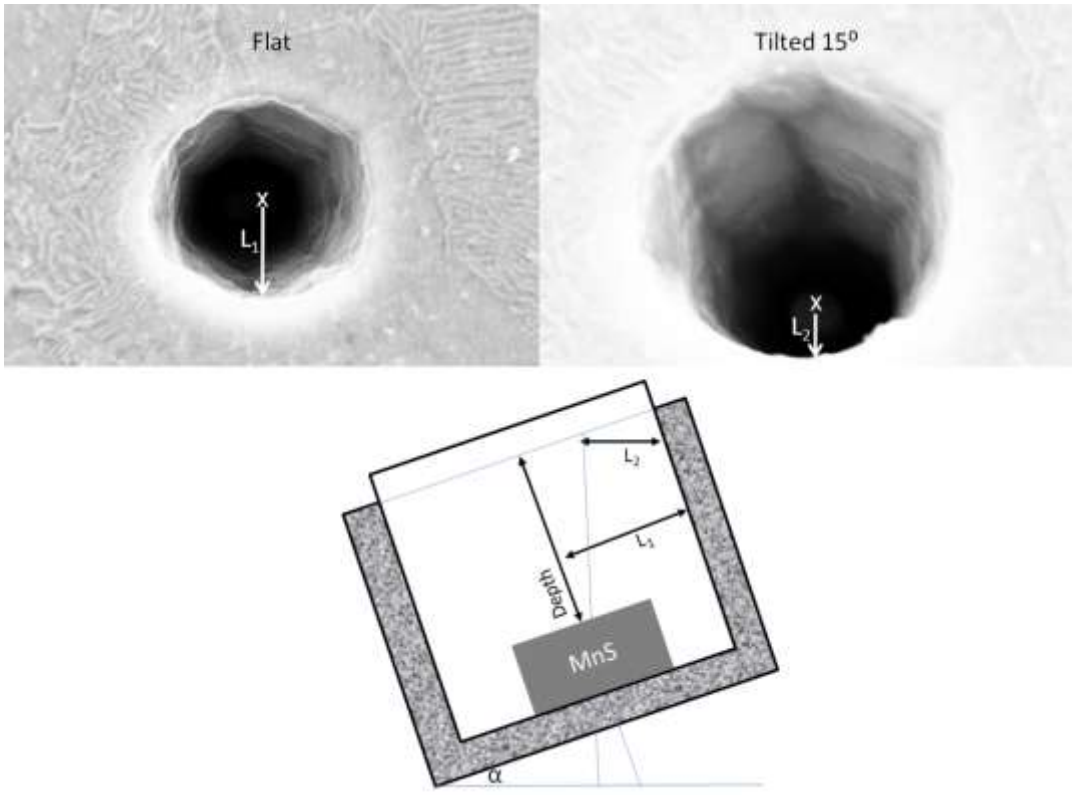

Figure 85: Diagram (bottom) with accompanying FEM images (top) of pit that has been tilted in order to calculate the depth of the inclusion within. L_1 is the distance from the inclusion to the pit edge before it is tilted a specified amount, and L_2 is the distance afterwards.

The results from the two methods were calculated for three corrosion pits (labeled pits #1–3) found on a sample exposed to sterile ALDC medium with [Na_2S] = 0.05 mM for two weeks. The FEM images and corresponding EDX spectra of points on the inclusion and next to the pit are given in Figs 86–88. Refer to the figure caption for measurement details.

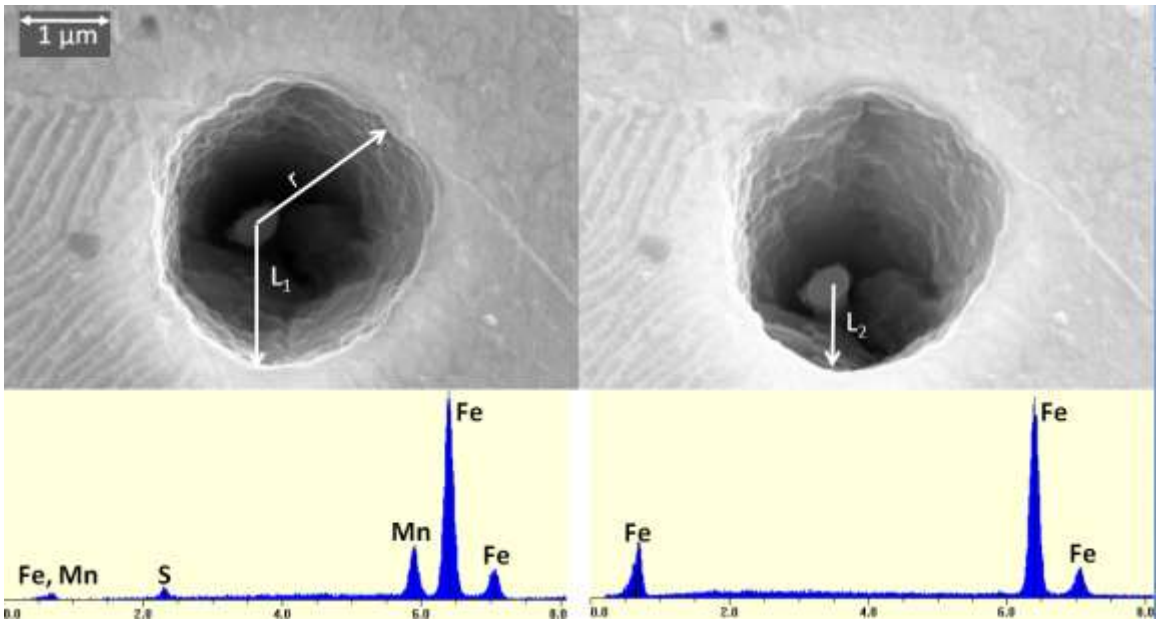

Figure 86: Pit #1. Geometric method: L_1 = 1.58 µm, L_2 = 970 nm, α = 15°, *r* = 2.04 µm, *D* = 2.5 µm. X– ray method: *d* = 2.2 µm.

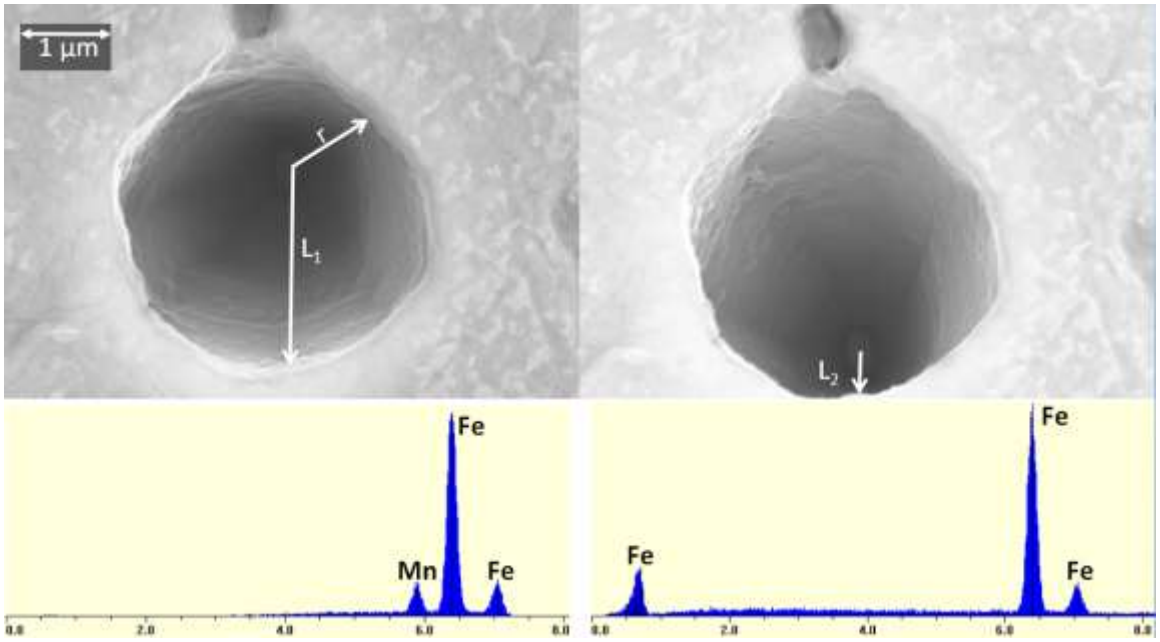

Figure 87: Pit #2. Geometric method: L_1 = 2.31 µm, L_2 = 510 nm, α = 15°, *r* = 1.27 µm, *D* = 1.5 µm. X– ray method: *d* = 5.2 µm.

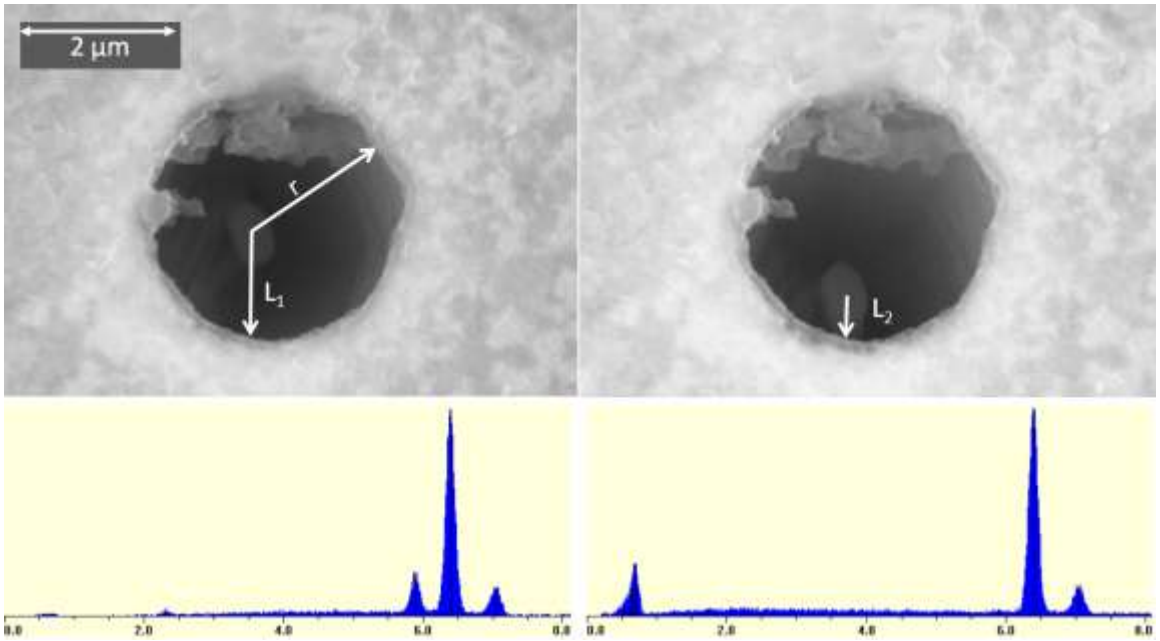

Figure 88: Pit #3. Geometric method: L_1 = 872 nm, L_2 = 427 nm, α = 10°, *r* = 1.18 µm, *D* = 1.4 µm. X– ray method: *d* = 2.3 µm.

Histograms of the path length through the steel, d, are given in Fig. 89 for the three pits, and the fitting parameters are given in Table 15. The EDX spectra taken from within the pit are also shown against the spectrum taken from the background for comparison.

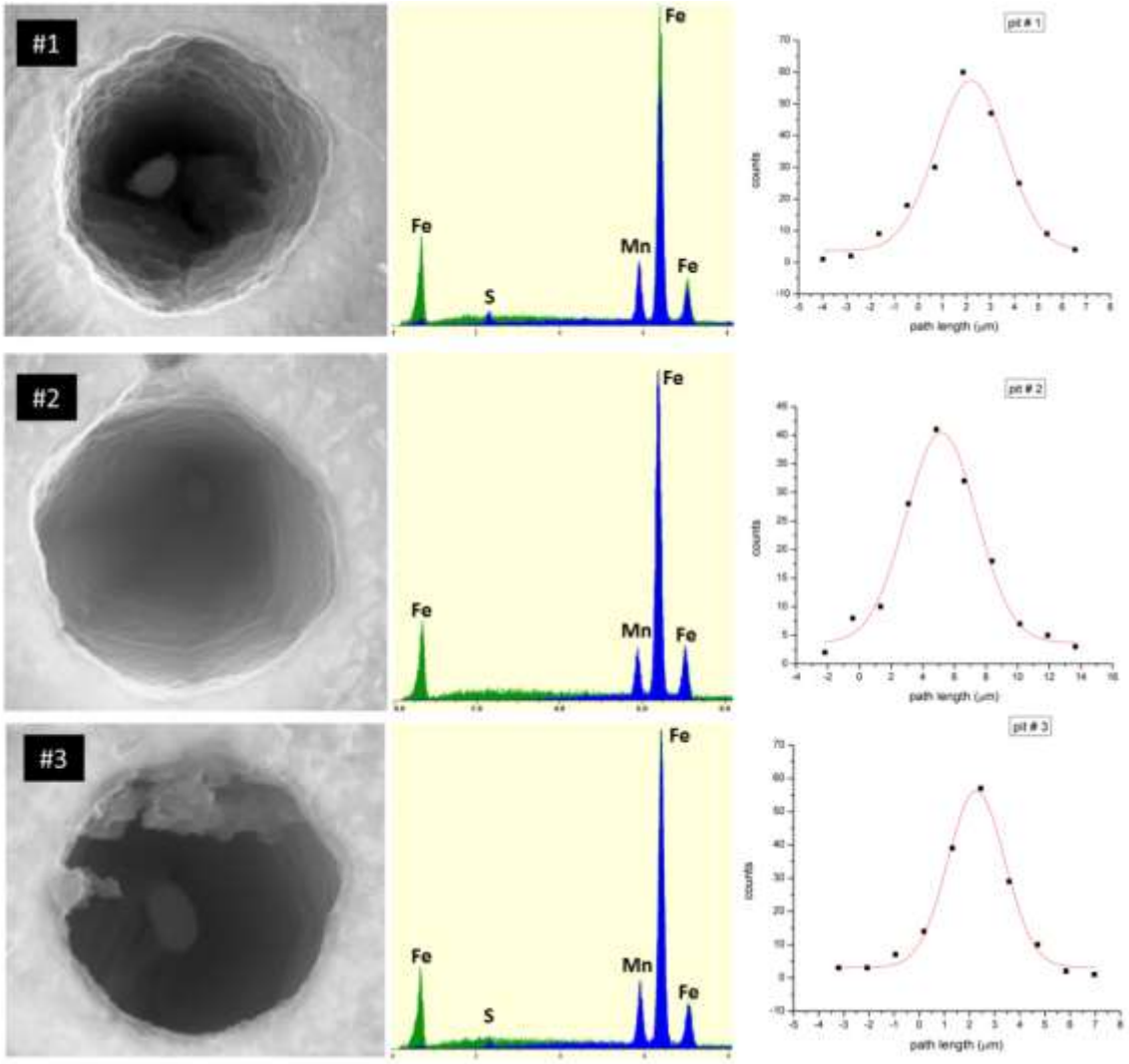

Figure 89: Summary of X- ray data taken from tilted pits containing inclusions: FEM images are given on the left, EDX spectra in the middle, and the distributions of calculated path length on the right.

Table 15: Curve fitting parameters of normal Gaussian fits of path length distributions for the three corrosion pits on coupon surface corroded by sterile ALDC medium for two weeks. The unit is μm, except where the parameter is unitless (N_0 and Height).

		Pit # 1	Pit # 2	Pit # 3
N_o	value	3.69	3.73	3.15
	error	2.11	1.04	0.95
d_c	value	2.19	5.18	2.27
	error	0.10	0.11	0.05
W	value	2.92	4.46	2.27
	error	0.26	0.28	0.11
A	value	196.44	205.38	150.87
	error	20.05	15.04	7.81
Standard deviation	value	1.46	2.23	1.13
FWHM	value	3.44	5.25	2.67
Height	value	53.66	36.75	53.11

The depths calculated using the geometric and X– ray methods are given in Table 16.

Table 16: Summary of pit depths as calculated using the geometric and X– ray methods.

	Pit Depth (μm)	
	Geometric method	**X – ray method**
Pit 1	2.2	2.7
Pit 2	6.7	3.8
Pit 3	2.49	2.1

These methods are not fully developed yet. Both the geometric and the X-ray method have uncertainties that need to be ironed out. The results are not too far from each other, and the trend is in the right direction. The methods are highly practical for getting a rough idea about pit depth where no other method would work. An AFM tip would not fit into a narrow pit well to measure depth. The optical methods do not have the spatial resolution. The measurements can be improved by calibration using standard wells prepared commercially on samples of interest. Such calibrations can be used to determine the unknown depths of the pits. This approach would be applicable in the

initial pitting processes; once the pits get very large, then other well-established techniques, such as optical or AFM-based techniques, can be used.

Impact of Electron Beam Irradiation of Surface on Corrosion

To corner the sites of pitting initiation, a scheme was devised to track inclusions throughout the corrosion process. Mineral inclusions of various compositions (mostly MnS and feldspar) were found using FEM, and their locations on the coupon surface were identified and recorded, as described in Methods. After the coupons were corroded and the specific mineral inclusions were found again, we were met with surprising results. The inclusions had been irradiated with the high-energy, 20-keV primary electron beam prior to corrosion to confirm their elemental content. These irradiated areas showed distinct morphological dissimilarities from the general corroded surface and other corroded inclusions in the near vicinity that had not been irradiated. Obviously, these data are not applicable to corrosion in Naval fuel tank systems, but their implications for physics and engineering, especially on the microscale, are of current interest.

When a high-energy electron beam impinges on a surface, many interactions occur that eject numerous forms of radiation and hence change the surface chemistry on the scale of the excitation volume. These processes were described in detail in Materials and Methods. Also, volatile hydrocarbon contaminants in the FEM sample chamber will adsorb on the surface and react to form less volatile carbon polymers. This builds as irradiation continues into a deposition layer on the surface that appears as a black square

in the shape of the analysis area. The effect is well known to SEM users and occurs on a wide range of samples.

An experiment was planned to measure the initiation of corrosion at sites of MnS inclusions immediately after immersion in the SRB cell culture. An "X" was scribed onto the coupon surface, and a group of MnS inclusions were found and imaged using FEM and analyzed using EDX. The group of inclusions before exposure to the corrosive medium is shown in the FEM images in Fig. 90, and their accompanying EDX spectra are given.

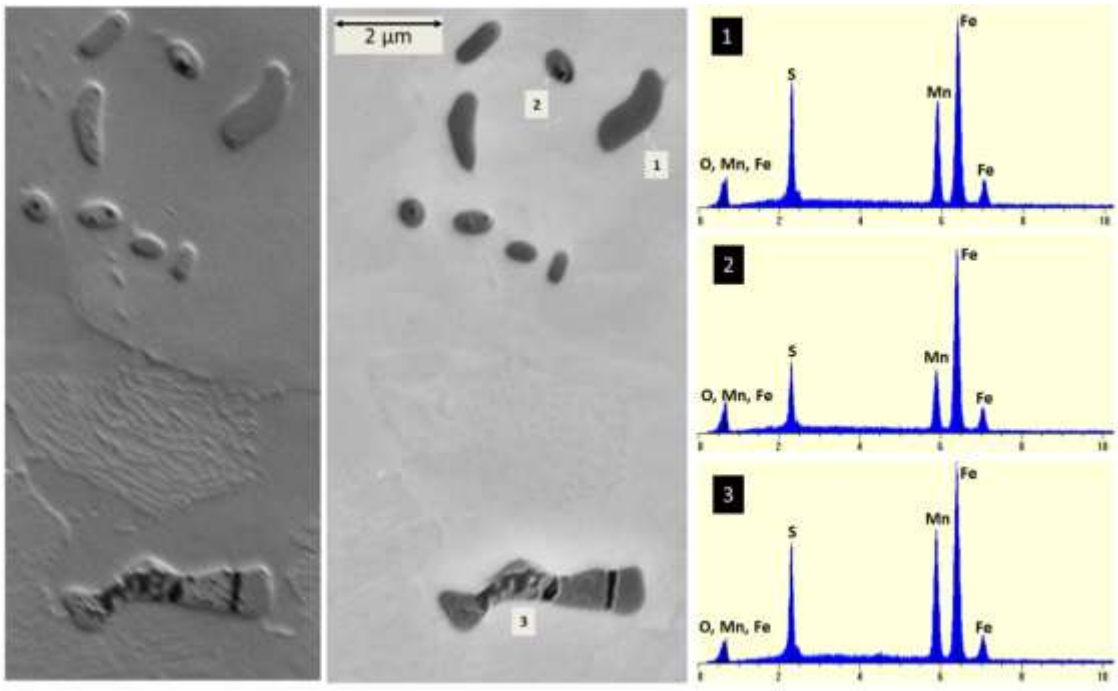

Figure 90: Group of MnS inclusions on coupon surface before corrosion: FEM images are given at 1 keV (left) and 20 keV (middle), as well as the corresponding EDX spectra (right).

The coupon was taken immediately from the FEM to the anaerobic chamber and immersed in the ALDC cell culture. Instantly, a brown spot about a millimeter in

diameter and centered on the scribed “X” appeared to the naked eye, whereas the rest of the surface remained shiny. Corroded samples will turn blackish/brown after prolonged exposure to SRB (> 1 day), but this clearly changed earlier than expected. We were prompted to remove the sample and investigate it again using FEM. The immersion time was <30 seconds. FEM images of a wide field of view of the analyzed region before and after exposure to the SRB are given in Fig. 91.

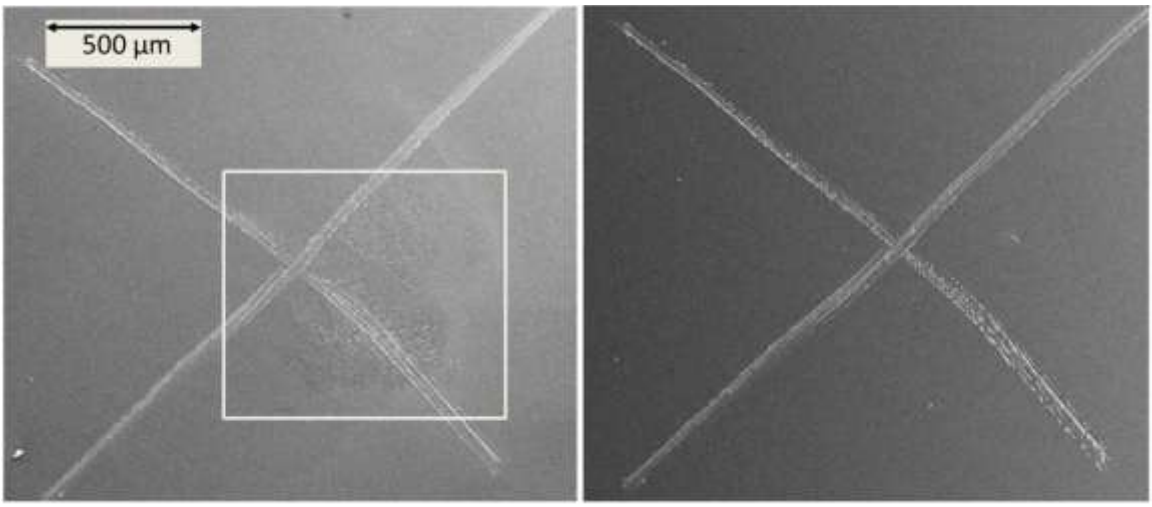

Figure 91: Corrosion deposits that formed immediately after exposure to the ALDC cell culture in the region previously irradiated by electron beam (left) are indicated by a white box. The same field of view before corrosion (right) is given for comparison.

Clearly, there is some kind of deposition in the region irradiated by the primary beam in the FEM. For a closer look at the inclusion group and deposition layer, the FEM images are shown in Fig. 92. The accompanying EDX are given in Fig. 93.

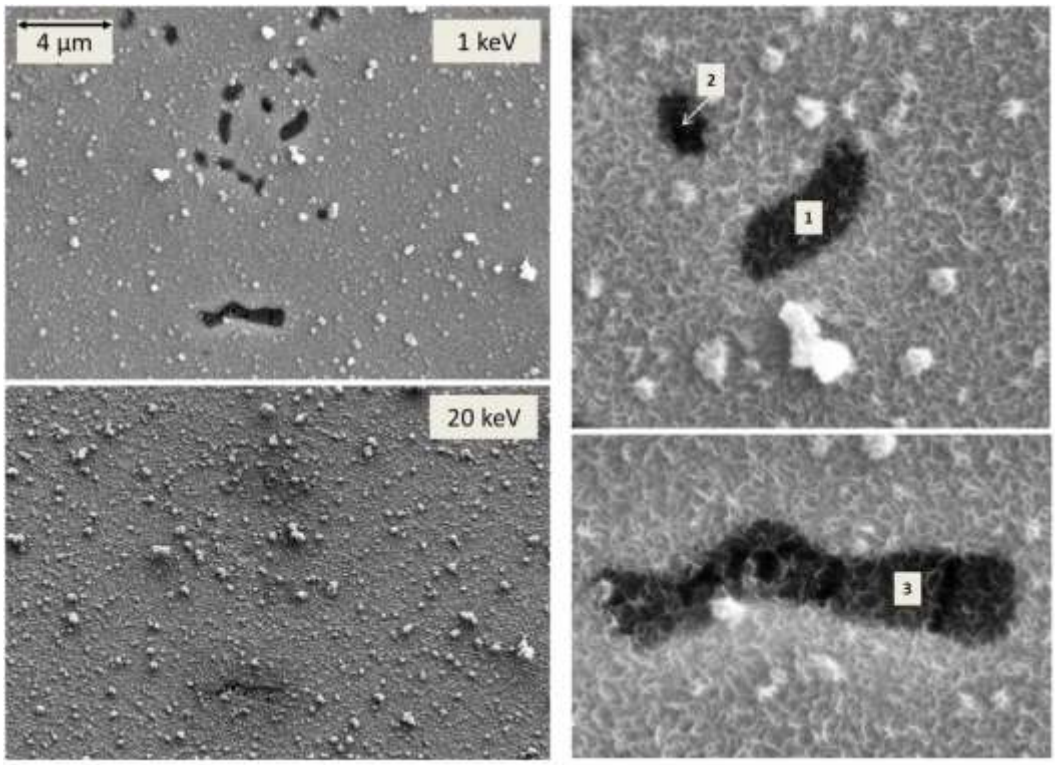

Figure 92: The same group of MnS inclusions after a brief exposure to the ALDC cell culture. Wide fields of view are given at the same magnification at (top) 1 and (bottom) 20 keV on the left, and a detailed view of the inclusions is given on the right.

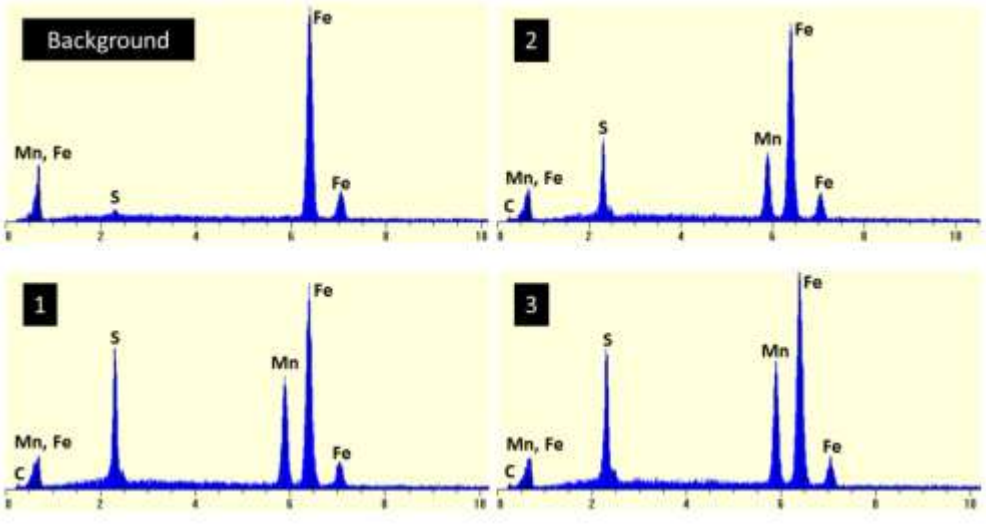

Figure 93: EDX spectra corresponding to the MnS inclusions and background shown in Fig. 92.

Note the appearance of carbon on the sample and sulfide corrosion. It appears that the microbes preferentially populated this part of the coupon surface, perhaps because of modification of this region resulting from irradiation by e beam. In their wake, they left a deposit of iron sulfide from the localized accelerated corrosion. Another suggestion is that the change in chemistry of the surface made it more susceptible to oxidation and subsequent corrosive attack.

An FEM image of an area infected with several MnS inclusions off the irradiated zone is shown in Fig. 94. Sulfide corrosion has been initiated, but there is no pitting yet around any of the MnS inclusions. The extent of general corrosion on this surface is miniscule compared to that in the irradiated zone. This proves that the electron beam itself acted as an accelerator of corrosion on a time scale of seconds.

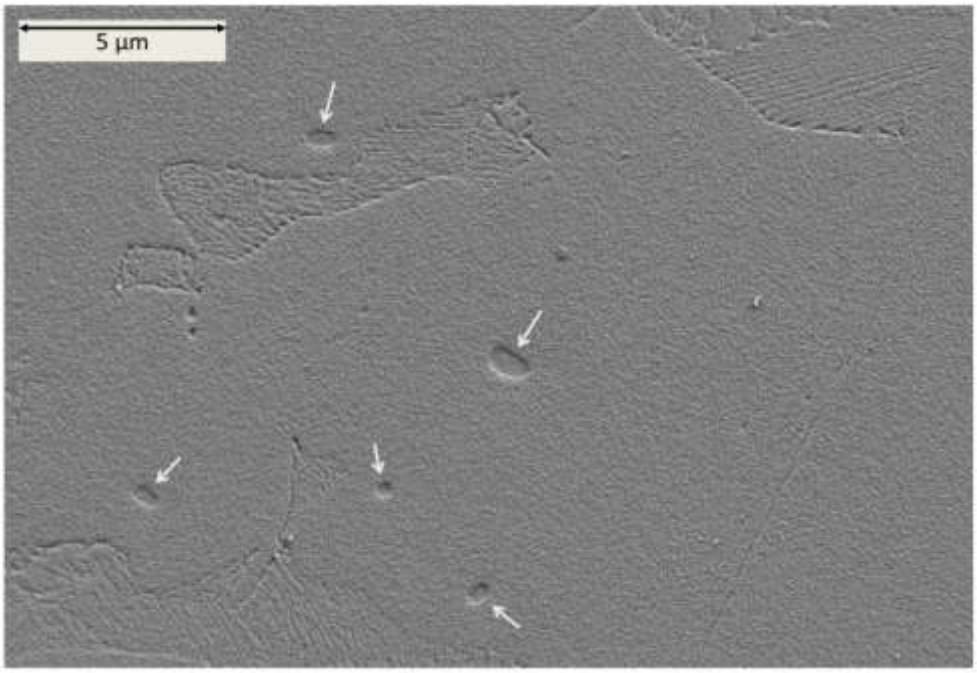

Figure 94: Area off irradiated zone after brief exposure to the ALDC cell culture. The surface roughness shows corrosion through the iron sulfide mechanism. White arrows point out MnS inclusions that were not severely corroded by the short immersion.

Steel coupons were exposed for 10 days to the abiotic sulfide control and the ALDC cell culture after having been irradiated with the 20-keV primary beam in the FEM for analysis. These results show the longer-term impact of the electron beam on the sample surface, which surprisingly was the opposite of acceleration: passivation. A group of inclusions from before and after corrosion in the abiotic sulfide solution are shown in Fig. 95.

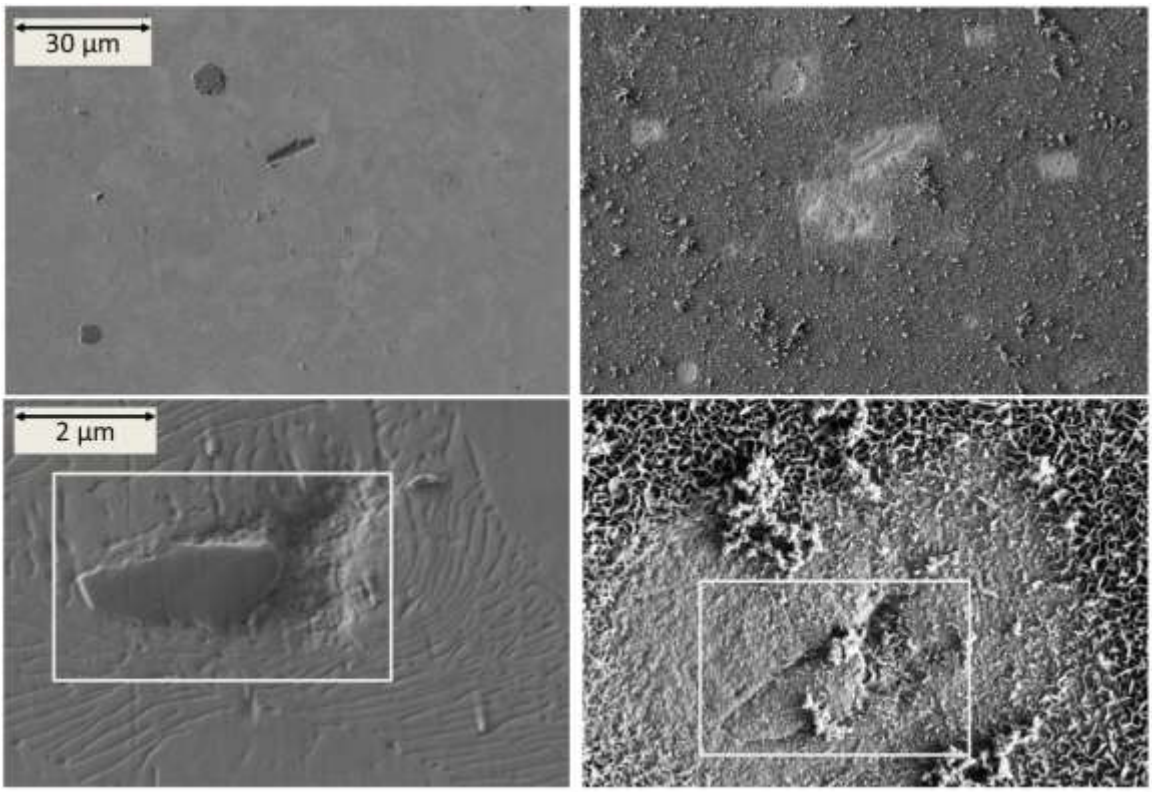

Figure 95: Group of various inclusions on coupon surface before (upper left) and after (upper right) corrosion by the abiotic sulfide solution with [Na_2S] = 25 mM for 11 days. A detail of a single inclusion from the field of view is shown before (left) and after (right) corrosion and is indicated by the white box.

A wide view is given to show that the effect occurred over a variety of elementally unique inclusions and on the surrounding iron matrix. An image at a higher

magnification shows that the surface truly is clean in these regions and that the region forms a well-defined square where the surface was analyzed and consequently irradiated by the primary beam.

FEM images of the biotically corroded sample taken before and after corrosion are given in Fig. 96.

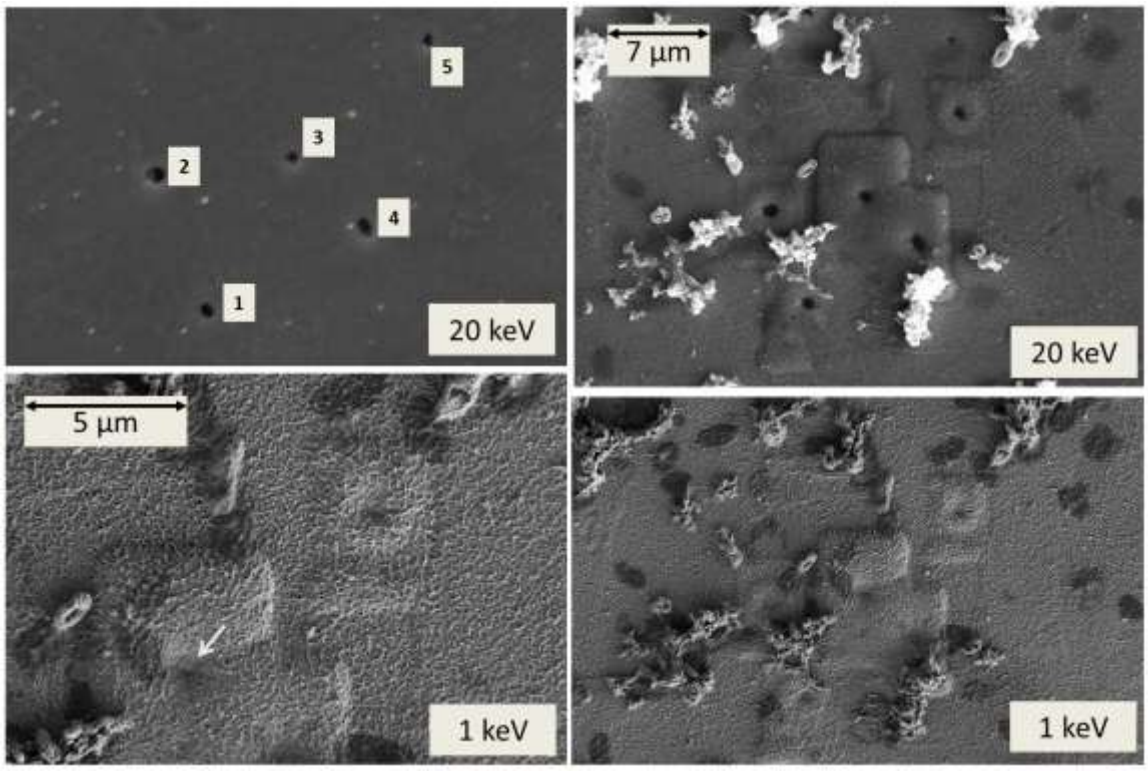

Figure 96: FEM images of a group of five MnS inclusions taken before (upper left) and after corrosion by the ALDC cell culture for 11 days. The right side of the figure is two FEM images of the same field of view, at (top) 20 and 1 keV. The bottom left FEM image is a detail of inclusions #3, 4, and 5. The white arrow points out where an inclusion is beneath a corrosion deposit as a divot.

The impact of the biotic solution is clearly different from that of the abiotic solution, despite both having sulfide as the dominant corroding mechanism. In this solution, the areas that had been investigated developed a swollen appearance. Whether

this is passivation or acceleration is questionable. The MnS inclusions are clearly divots, as indicated with the white arrow in the bottom left image.

The sample described in Fig. 10 in Materials and Methods was exposed for two weeks to the ALDC cell culture and stripped with Clark solution before being reinvestigated using AFM. Before corrosion, all inclusions in the FOV were confirmed to be MnS using EDX or Auger nanoprobe, as described in Methods. FEM images of the resultant sample surface are given in Fig. 97.

From the 1-keV images, it appears most of the inclusions did not dissolve, since they do not appear as dark holes. However, the EDX taken from two of the inclusions show that the low-energy X– rays are attenuated away, indicating pit depth, as shown in Fig. 98.

No MnS was detected from where the inclusion was, and chlorine was left behind from the action of the Clark solution. This suggests that the solid appearance of the pit is due to a cap that has formed on top, which the high-energy primary beam used for EDX penetrates.

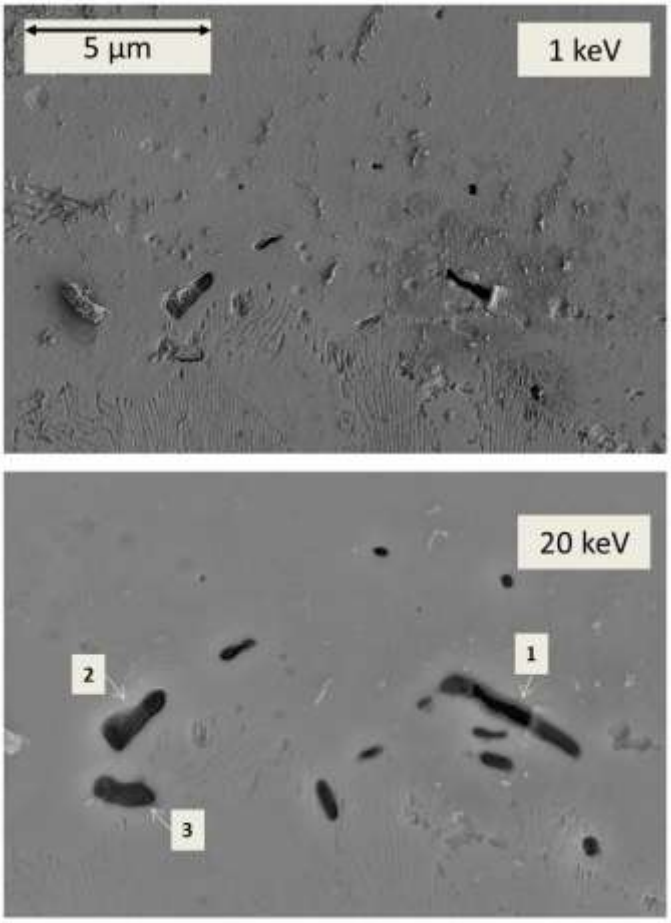

Figure 97: Group of MnS inclusions after irradiation with a 20-keV primary electron beam, corrosion by ALDC cell culture for two weeks and the removal of corrosion deposits by treatment with Clark solution. Note caps remaining over empty pits.

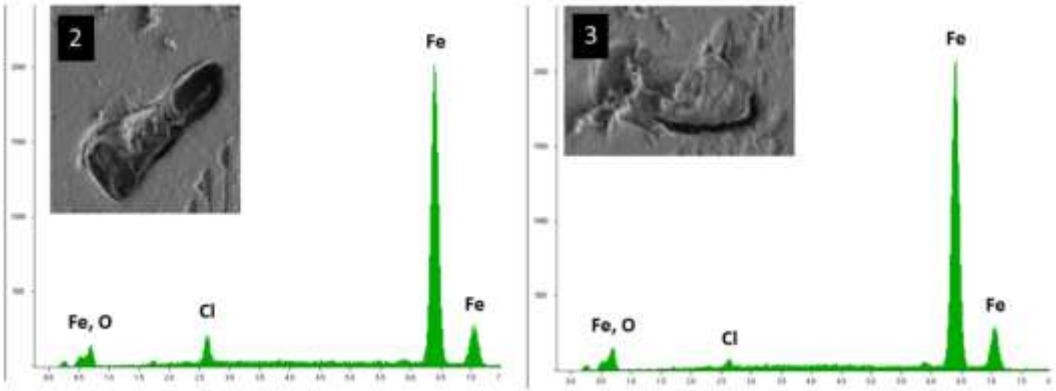

Figure 98: EDX spectra from inclusions (left) #2 and (right) #3 with corresponding FEM images. Note that low-energy X- ray intensity is attenuated and that the MnS characteristic X- rays are missing.

An FEM image from a hole left from a presumed MnS inclusion that was not irradiated by the electron beam before corrosion is given in Fig. 99 as a control against the impact of the primary beam.

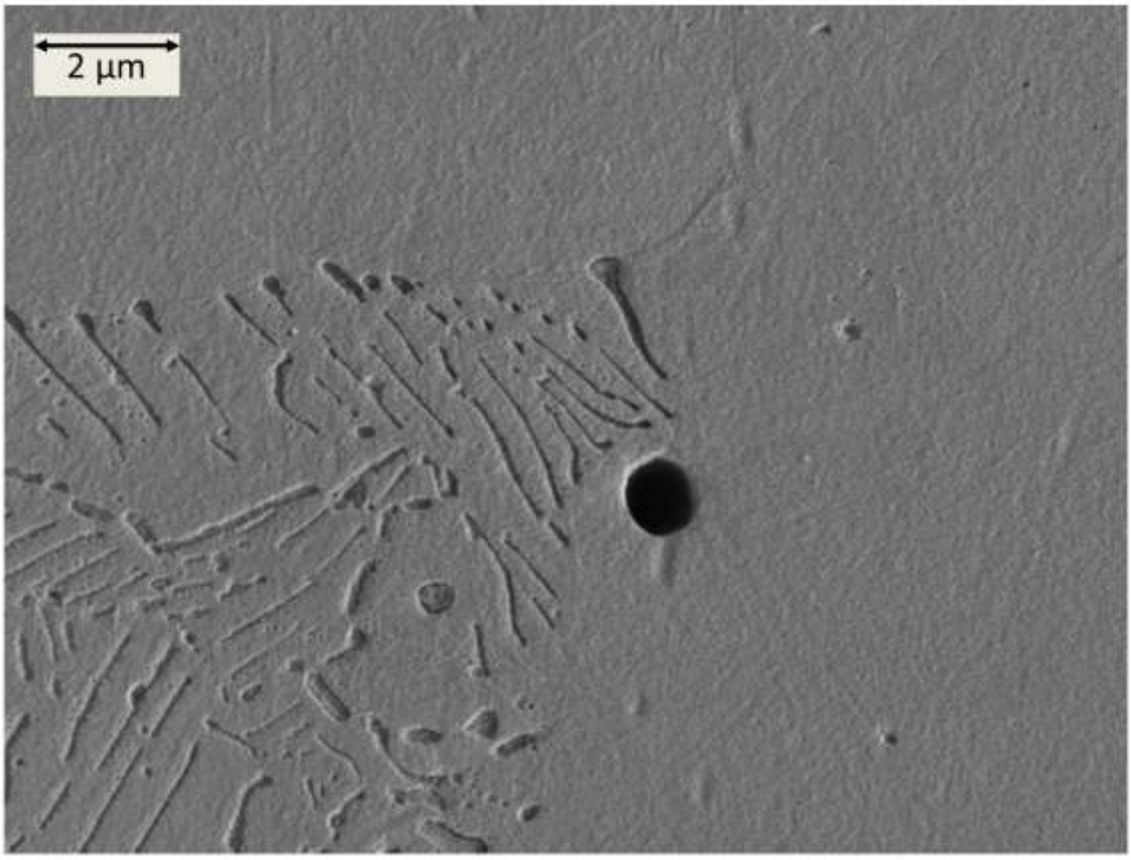

Figure 99: Empty hole observed off the irradiated region. It is assumed that there was an MnS inclusion here before treatment with Clark solution.

This pit is typical of pits left by MnS inclusions after treatment with Clark solution. For comparison with MnS inclusions on a clean steel surface dissolved by Clark solution, see Fig. 29 in Material and Methods.

To further investigate the morphology of these pits, they were imaged using AFM. These data and high-resolution FEM images show that there are indeed caps left

on the inclusions/pits after treatment with Clark solution. This suggests that the impact of the electron beam negated the effect of the Clark solution on the corrosion deposits that accumulated atop the irradiated surface. Not only does the electron beam influence the metal surface, but it also affects the corrosion products that are deposited upon it.

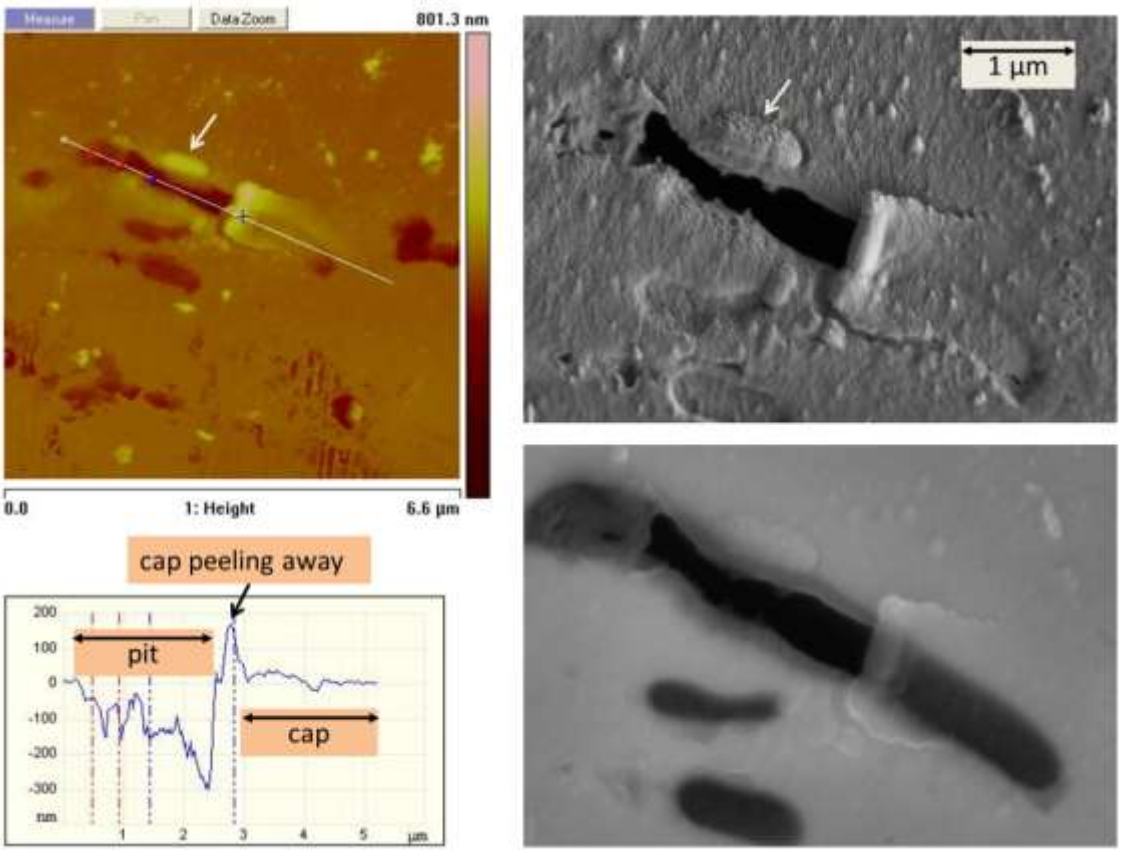

Figure 100: MnS inclusion labeled #1 after irradiation with the primary electron beam, corrosion by ALDC cell culture for two weeks, and the removal of corrosion deposits by treatment with Clark solution. FEM images taken at (top) 1 and (bottom) 20 keV are given on the right side of the figure. On the left side of the figure is (top) an AFM scan with (bottom) a line section of the featured MnS inclusion. Note the remains of a cap and cell pointed out in the upper right FEM image. The cell is comparable in size to one of these MnS inclusions.

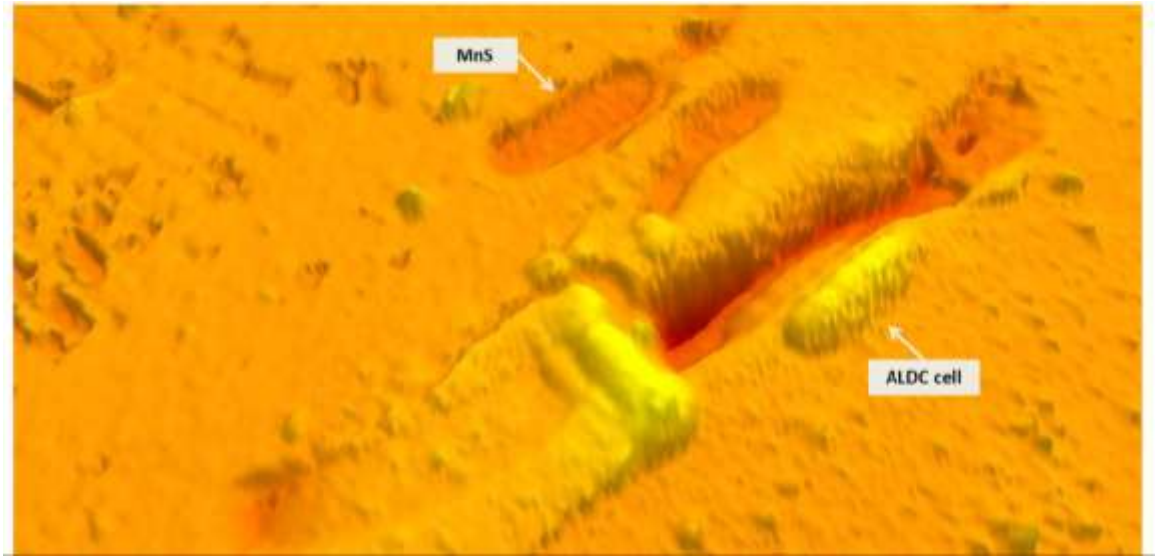

Figure 101: 3-D image of surface in the vicinity of inclusion #1. Another MnS inclusion and ALDC cell are pointed out for comparison. The cap can clearly be seen peeling away from the pit.

A final example is given in which an untouched MnS inclusion is irradiated using FEM after corrosion by ALDC cell culture for two weeks. The impact of the primary electron beam, this time on the corrosion deposits after stripping with Clark solution, is seen in Fig. 102.

The FEM images indicate that the inclusion and the corrosion deposit covering it were untouched. However, once again, EDX shows that the MnS was lost from the inclusion. The Si and small amount of Ca present in the inclusion, however, remained. The area that was scanned less per unit area by the rastered 1-keV primary beam at a lower magnification (to take the image in the upper right corner of Fig. 102) was passivated less than the areas where the 20-keV primary beam was used at high magnification to take EDX spectra. There are two scanned areas where high

magnification was used: one centered on the inclusion (to take the inset image in Fig. 102) and another directly next to it from focusing and adjusting the electron beam.

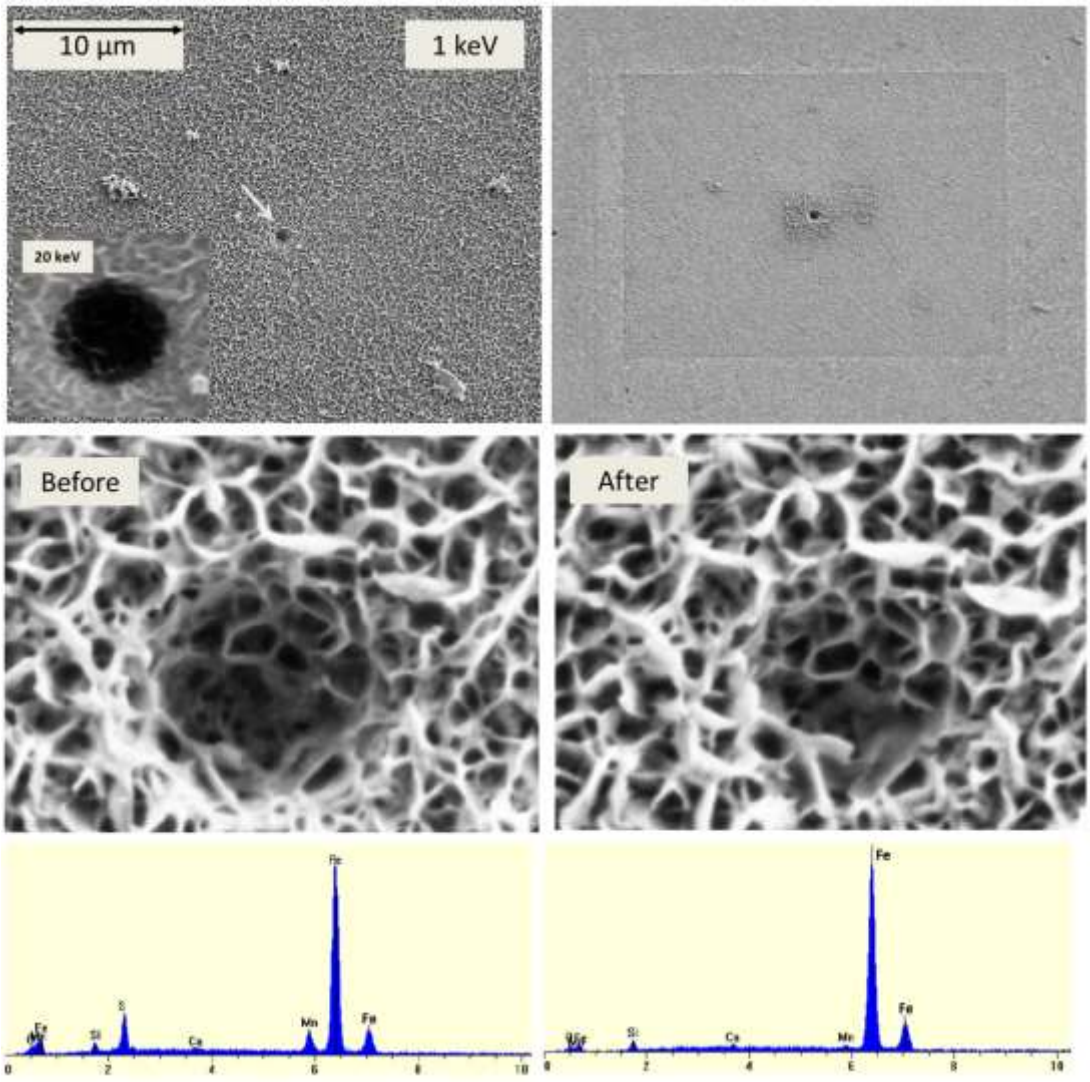

Figure 102: Images taken (left) before and (right) after treatment with Clark solution of a coupon surface that had been corroded by an ALDC cell culture for two weeks and then irradiated with the 20-keV primary electron beam. The scanning done at 1 keV to produce the image at the upper left is what induced the largest passivated region on the image shown at the upper right. A 20-keV FEM image is inset in the upper left image to illustrate how the primary beam image appears underneath the corrosion deposit. Note that the region irradiated the strongest by the primary beam appears the least affected by the Clark solution in the FEM images but that the EDX shows that the inclusion dissolved.

In conclusion, a metal surface irradiated with the high-energy (20-keV) primary electron beam in FEM is exceptionally prone to corrosive attack at the beginning of exposure to these anaerobic sulfidogenic environments but becomes passivated after a couple weeks' time. The effect of irradiating a corroded surface is passivation under exposure to the low-pH Clark solution. A corrosion deposit that has developed on an irradiated area is harder to remove by treatment with Clark solution and leaves behind caps covering empty pits that once held inclusions.

The answer to what causes the passivation lies in the surface phenomena that arise from interactions between the 20-keV primary electron beam and the specimen. In order to elucidate these, surface-sensitive techniques need to be applied. This is the direction of future work.

REFERENCES CITED

ASTM Standard A29/A29M – 12, 1957 (2012), "Standard Specification for Steel Bars, Carbon and Alloy, Hot-Wrought, General Requirements for," ASTM International, West Conshohocken, PA, 2012, DOI: 10.1520/A0029_A0029M-12, www.astm.org.

Beech, I. B. and J. Sunner (2004). "Biocorrosion: towards understanding interactions between biofilms and metals." *Current Opinion in Biotechnology* **15**: 181-186.

Brown, B. F., Fujii, C. T., and E. P. Dahlberg (1969). "Methods for studying the solution chemistry within stress corrosion cracks." *Journal of the Electrochemical Society* **116**: 218-219.

Davidova, I. A., Duncan, K. E., Choi, O. K., and J. M. Suflita (2006). "*Desulfoglaeba alkanexedens* gen. nov., sp. nov., an n-alkane-degrading, sulfate-reducing bacterium." *International Journal of Systematic and Evolutionary Microbiology* **56**: 2737-2742.

Feio, Maria, J., Beech, Iwona, B., Carepo, M., Lopes, J. M., Cheung, C. W. S., Franco, R., Guezennec, J., Smith, J. R., Mitchell, J. I., Moura, J. J. G., and A. R. Lino (1998). "Isolation and Characterisation of a Novel Sulphate-reducing Bacterium of the *Desulfovibrio* Genus." *Anaerobe* **4:** 117-130.

Goldstein, J. I., Newbury, D. E., Echlin, P., Joy, D. C., Romig, A. D., Jr., Lyman, C. E., Fiori, C., and E. Lifshin (1992). Scanning Electron Microscopy and X-Ray Microanalysis. New York, N.Y., Plenum Press.

Kreft, S., and M. Kreft (2009). "Quantification of dichromatism: a characteristic of color in transparent materials." *Journal of the Optical Society of America A* **26:** 1576-1581.

Lewandowski, Z., Dickinson, W., and W. Lee (1997). "Electrochemical interactions of biofilms with metal surfaces." *Water Science and Technology* **36**: 295-302.

Venzlaff, H., Enning, D., Srinivasan, J., Mayrhofer, K. J. J., Hassel, A. W., Widdel, F., and M. Stratmann (2012). "Accelerated cathodic reaction in microbial corrosion of iron due to direct electron uptake by sulfate-reducing bacteria." *Corrosion Science* **xx**: xxx-xxx.

Videla, H. A., and L. K. Herrera (2009). "Understanding microbial inhibition of corrosion. A comprehensive overview." *International Biodeterioration and Biodegradation* **63**: 896-900.

Widdel and Bak (1992). The Prokaryotes: A handbook on the biology of bacteria: Ecophysiology, isolation, identification, applications, 2nd edition. New York, N.Y., Springer-Verlag.

Willey, J. M., Sherwood, L. M. and C. J. Woolverton (2011). Prescott's Microbiology. New York, N.Y., McGraw Hill.

Wranglèn, G. (1974). "Pitting and sulphide inclusions in steel." *Corrosion Science* **14**: 331-349.

APPENDICES

APPENDIX A

BRACKISH WATER MINERAL MEDIUM

I.D	gm/L	Notes
NaCl	20.0	
$MgCl_2$ x $6H_2O$	3.0	
$CaCl_2$ x_2 H_2O	0.15	
NH_4Cl	0.25	
KH_2PO_4	0.2	
KCl	0.5	
RST trace elements	10 mL	X 100 stock solution
Resazurin	1.0 mL	0.1 % stock solution
Na_2SO_4	4.0	

APPENDIX B

RST TRACE ELEMENTS

I.D	g/L
Nitroloacetic Acid	2.0
$MnSO_4 – H_2O$	1.0
$Fe (NH_4)_2 (SO_4)_2$	0.8
$CoCl_2 – 6H_2O$	0.2
$ZnSO_4 – 7 H_2O$	0.2
$CuCl_2 – 2H_2O$	0.02
$NiCl_2 – 6H_2O$	0.02
$Na_2MoO_4 – 2H_2O$	0.02
Na_2SeO_4	0.02
$NaWO_4$	0.02

APPENDIX C

VITAMINS FOR CELL GROWTH

I.D.	mg/L
Biotin	2.0
Folic Acid	2.0
Pyridoxine – HCl	10.0
Thiamine – HCl	5.0
Riboflavin	5.0
Nicotinic Acid	5.0
Calcium Pantothenate	5.0
Cyanocobalamin	5.0
p-Amonobenozic Acid	5.0
Lipoic Acid	5.0

APPENDIX D

MATLAB PROGRAM CALCULATING MnS INCLUSION DISTRIBUTION

```
close all
clear
clc

level = 150; % threshold for finding minima
conn = 8; % connectivity 4 for sides, 8 for corners

count = zeros(512*12,1); % initialize array to track counts in each FOV
k = 0;

FOV_prefix = 'data\r1c1_r';
s = 1024/75; % pixel width per micron
vsp = s*1.75; % vertical spacing between subimages in pixels
hsp = s*3; % horizontal spacing
sq = s*15; % square dimension of subimage
SUM = zeros(1,4);
t=0;

for i = 1:16
   row = num2str(i);

      for j = 1:32
         col = num2str(j);
         FOV = strcat(FOV_prefix,row,'c',col,'.tif');
         X = imread(FOV);
         image = X(1:706,:);
         for l = 1:4
            for m = 1:3
               % row and column for cropping
               T = round(vsp*m+sq*(m-1)); % top
               B = round(m*(vsp+sq)); % bottom
               L = round(hsp*l+sq*(l-1));  % left
               R = round(l*(hsp+sq));% right
               subimage = image(T:B,L:R);

               B = logical(imextendedmin(subimage,level));
               [labeled,numObjects] = bwlabel(B,conn);

               k = k+1;
               % Do region props
               STATS = regionprops(labeled);
               for q = 1:numel(STATS)
                  a = STATS(q,1).Area ;
                  if a < 600
```

```
                t = t+1;
                count(k) = count(k) + 1;
                AREA(t) = a;
            end
        end

        % remove any spurrious 1 object images and reduce to 0
        if numObjects == 1
            SUM(1) = sum(sum(labeled(1:100,1:100)));
            SUM(2) = sum(sum(labeled(101:end,1:100)));
            SUM(3) = sum(sum(labeled(1:100,101:end)));
            SUM(4) = sum(sum(labeled(101:end,101:end)));

            if nnz(SUM) == 1
                count(k) = 1;
            else count(k) = 0;
            end

            if sum(sum(labeled)) == numel(labeled)
                count(k) = 0;
            end
        end


%%%%%%%%%%%%%%%%%%%%%%%%%%%%%%%%%%%%%%%%%%%%%%%%%%%%%%%%%%%%%%%%%%%%%%%
%%%%%%%%%%%%
            %  filename_sub = strcat('data150threshmax\',...
            %     num2str(k), strcat('r1c1_r',row,'c',col,...
            %     'sub.tif'));
            %  imwrite(subimage,filename_sub)
            %  filename_bin = strcat('data150threshmax\',num2str(k)...
            %     ,strcat('r1c1_r',row,'c',col,'bin.tif'));
            %  imwrite(B,filename_bin)
          end
       end
    end

end

hist(count,25)
```

APPENDIX E

MATLAB PROGRAM FOR CALCULATING PATH LENGTH OF X-RAYS

```
clear
close all
clc

% Here is a program to calcualate the attenuation of x-rays through the
% steel as they leave a MnS inclusion from deep within a pit.
% The x-ray pathlength is calcuated from tabulated values of the mass -
% attenuation coeffectient (mu - from NIST) and experimental values of
% x-ray intensity as a function of energy from the pit and background.

% define a range over which to average the pathlength
S = 2.9e3; % in eV
F = 4.5e3;

% number of bins to make the histogram with
bins = 10;

% First, spectra are taken at a range of 0 - 20 keV and given as 4096 data
% points.

eV = (1:4095)'.*(20000/4095);

% Now, load the background spectra from the text file
bground_filename = 's1_pit3_bg.txt';
fileID = fopen(strcat('spectra/',bground_filename));
A = textscan(fileID,'%f32','HeaderLines',120);
bckgrnd = A{1,1};
% Trim the background of zeroes
ind1 = find(bckgrnd);
% bckgrnd(bckgrnd==0) = [];

% Load the hole spectra from the text file
hole_filename = 's1_pit3_inc.txt';
fileID = fopen(strcat('spectra/',hole_filename));
A = textscan(fileID,'%f32','HeaderLines',120);
hole = A{1,1};
% Trim the hole of zeroes
ind2 = find(hole);
% hole(hole==0) = [];

% Make a vector of the indices of points where neither background nor hole
% signal is zero

k = 1;
```

```
for j = 1:numel(ind1)
   for i = 1:numel(ind2)
      if ind1(j) == ind2(i)
         ind(k) = ind1(j);
         k = k+1;
      end
   end
end
ind = ind';

hole = hole(ind);
bckgrnd = bckgrnd(ind);
eV = eV(ind);

% Reference June 29,2012 (pg 7 in third lab notebook)
% Now take the quotient of the background intensity and hole intensity

Q = bckgrnd./hole;

% Now, give the mass-attenuation coeffecient for Iron (numbers are
% extrapolated from data in the range of 1:20 keV)
% reference:
% http://physics.nist.gov/PhysRefData/XrayMassCoef/ElemTab/z26.html

rho = 7.8; % denisty of steel grams per centimeter cubed
range = find(eV>7000);
a = range(1);
b = numel(eV);

mu(1:a) = (rho*1.33e-4)*((1e-6)*eV(1:a)).^(-2.62);
mu(a+1:b) = (rho*7.31e-4)*((1e-6)*eV(a+1:b)).^(-2.68);
mu = mu';

% Calculate the X-ray pathlength in microns
PL = (log(Q)./mu)*1e4;

plot(eV,bckgrnd,'og')
hold on
plot(eV,hole,'or')
plot(eV,PL,'ob')
xlabel('eV');
ylabel('A.U. (spectra), microns (path length)');
legend('background','pit','path length');
title('raw data');
```

```
% lower limit:  where signal from hole becomes good
range = find(eV > S);
s = range(1);
% upper limit:  where lower limit of Mn signal begins
range = find(eV > F);
f = range(1);

figure
histfit(PL(s:f))
title('histogram of pathlength over averaged range')
xlabel('pathlength (microns)')
ylabel('counts')
```